



ÉCOLE POLYTECHNIQUE
FÉDÉRALE DE LAUSANNE

MASTER THESIS

FACULTY OF MECHANICAL ENGINEERING

Methodology Improvement for Performance Assessment of Pumping Kite Power Wing

Benoît PYTHON

supervised by

Dr. Mohamed FARHAT EPFL

Dr. Axelle VIRÉ TU Delft

PhD. Anna BLEY TU Delft

in collaboration with



March 17th, 2017

Acknowledgements

When I was a kid flying my toy kite in front of my home, I was far from realising the true potential of the wind energy. Of course, I flew my kite crosswind to experience the most power. Of course, I extended the original lines to reach higher altitudes. However, the physical concepts behind these aspects were for me completely mysterious. I was simply flying my toy kite. As a big kid, I am still astounded and amazed when I see the Kitepower wing gracefully flying through the sky. Nevertheless, I am now aware not only of the working principle of a kite, but also of the great energy potential available in the wind. The more I discover about it, the more I wonder why this source of energy has not been more explored yet. I am truly convinced that the future of harvesting wind energy, especially by means of Airborne Wind Energy systems, shines bright.

I would like to thank all the people who have made my M.Sc. Thesis in Delft possible, starting from Switzerland, with my EPFL supervisor Mohamed Farhat who encouraged me to seize the opportunity of going abroad for such a rich and valuable exchange. I am also thankful for his support and valuable advices.

My thanks go as well to my supervisor Axelle Viré and her colleague Roland Schmehl from TU Delft who welcomed me heartily within their research group and provided me with useful feedback. Still on the side of TU Delft, I want to particularly thank Anna Bley who acted as my second supervisor and was available any time for sharing my problems and having helpful and interesting discussions together. I am very grateful for the time she devoted to me not only in Delft but also during trips to Germany.

This M.Sc. Thesis would not have been possible without the close collaboration of Kitepower team. Thus, I would like to thank especially Johannes Peschel and Joep Breuer not only for their partnership but also for their constructive advices and technical guidance. Obviously, the Kitepower team, composed at that time by Antonello Cherubini, Balazs Szalai, Bert Buchholz, Bruno Fernandes, David van Rijn, Eduardo Terzidis, Roger Coenen, Roland Verheul and Pietro Faggiani, supported me in one way or another.

I am also grateful to Jan Hummel and Christoph Elfert from TU Berlin for performing test together thanks to their own test bench. They not only provided me with experimental data, but also helped me to understand their setup and its working principle.

Thanks also to Siegfried Vlaminck from Genetrix Kiteboarding for his clear and helpful explanations about kite design strategies.

This six-month period was a long journey which was fortunately supported by tens of people starting from the students of the Room 6.08, my dear Dutch and Swiss friends as well as my beloved family.

Delft, the 17th of March 2017

Benoît Python

"My interest is in the future because I am going to spend the rest of my life there"
Charles Kettering

Abstract

Pumping kite power systems are a promising way of harnessing clean energy from high-altitude winds. A large kite flies crosswind developing a strong pulling force through a tether which is connected at the ground to an electrical generator. The power output of such innovative systems is directly related to the wing aerodynamic properties which therefore play a key role. Moreover, the latter, often assumed with best guess, are also required for computational simulations at development stage.

In this context, the research group of TU Berlin recently designed a car towing test bench for evaluating flexible airfoil performances in an automated and repeatable manner. By towing the kite at a prescribed speed, relevant information, such as tether force and elevation angle, are extracted and can be converted into aerodynamic properties thanks to a suitable analytical model.

With the purpose of improving the assessment of aerodynamic properties and their exactitude, the present work takes advantage of the TU Berlin test bench by investigating the Kitepower wing. An alternative testing methodology is suggested and compared against the current procedure, indicating a dynamic behaviour of the kite. A 2D quasi-steady point mass model is implemented to compute the kite aerodynamic properties by taking both wing and tether mass as well as tether aerodynamic effects into consideration. Eventually, a detailed analytical model of the tether is developed to assess its sag and effects on the kite performance. Finally, an attempt to provide polar curves with respect to the angle of attack rather than the power ratio is experimentally carried out.

Keywords

Airborne Wind Energy, Pumping Kite Power System, Kite, Aerodynamic Properties, Lift-over-Drag Ratio, Tether Sag, Power Ratio

Contents

Acknowledgements	iii
Abstract	v
List of Figures	x
List of Tables	xiv
Nomenclature	xv
1 Introduction	19
2 Literature Study	23
2.1 Natural Wind	23
2.1.1 Low Altitude Wind	23
2.1.2 High Altitude Wind.....	24
2.2 Wind Turbine Energy.....	24
2.2.1 Wind Turbine Evolution	25
2.3 Airborne Wind Energy.....	26
2.3.1 Ground-Gen	27
2.3.2 Fly-Gen.....	28
2.3.3 Crosswind.....	29
2.3.4 Key Factors – Aerodynamic Coefficients.....	30
2.4 Experimental Research – State of the Art.....	31
2.4.1 Wind Tunnel Testing	31
2.4.2 Car Tow Testing.....	32
2.4.3 Circular Testing	35
2.4.4 Crosswind Testing	36
2.4.5 Aerodynamic Curves with respect to	38
2.4.5.1 Angle of Attack.....	38
2.4.5.2 Back Line Force Ratio	41
2.4.5.3 Brake Position	42
2.4.5.4 Power Ratio.....	43

2.5	Background Theory and Theoretical Models	44
2.5.1	Wind Models.....	44
2.5.2	Wing Aerodynamic.....	44
2.5.3	Kite Model.....	46
2.5.4	Tether Models.....	46
3	Thesis Goal and Approach	49
3.1	Objective	49
3.2	Approach.....	49
4	Experimental Setup and Methodology.....	51
4.1	Kites.....	51
4.2	Testing Conditions.....	52
4.3	Test Bench - TETA Setup.....	52
4.3.1	Accuracy of Measurement.....	53
4.4	Testing Procedure	54
4.4.1	Dynamic Maneuvers	54
4.4.2	Static Maneuvers	55
4.4.3	Summary.....	55
4.5	Power Ratio Angle.....	55
5	Theoretical Models	57
5.1	General Aspects	57
5.2	Two-Dimensional Point Model.....	57
5.3	Tether Mass Contribution	58
5.4	Tether Aerodynamics	60
5.5	Tether Sag Model	60
5.6	Angle of Attack Assessment	62
6	Results.....	63
6.1	Data Processing.....	63
6.1.1	Dynamic Maneuvers Processing	64
6.1.2	Static Maneuvers Processing	65
6.1.3	Summary.....	66
6.1.4	Uncertainty Propagation.....	67
6.2	Dynamic Maneuvers	68
6.3	Static Maneuvers.....	69
6.4	Dynamic vs Static Maneuvers	71
6.5	Mass and Tether Effects on Aerodynamic Performances	74

6.6	Tether Sag Effect	77
6.7	Angle of Attack - Power Ratio Relationship	80
7	Discussion and Recommendations.....	86
7.1	TETA Setup	86
7.1.1	Methodologies	86
7.1.2	Kite Comparison.....	87
7.2	Source of Error	89
7.2.1	Random Quantified Error.....	89
7.2.2	Random Unquantified Error.....	89
7.2.3	Systematic Unquantified Error.....	89
7.2.4	Summary.....	90
7.3	Parameter Sensibility	91
7.4	Main Recommendations	92
8	Conclusion	93
8.1	Achieved Results	93
8.2	Future Development	94
9	References.....	95
10	Annexes.....	99
10.1	Global Wind Potential	99
10.2	Advantage of Airborne Wind Energy Systems	100
10.3	Lumped Tether Mass Derivation.....	101
10.4	Sag Differential Equation Derivation.....	102
10.5	Error Propagation Derivation	103
10.6	Corrected Lift and Drag Coefficients	104
10.7	Kite and Tether Mass Effects.....	105
10.8	Tether Drag and Lift Effects.....	106
10.9	Hypothetical Pitch Angle – Power Ratio Relationship.....	107
10.10	Instantaneous Aerodynamic Properties vs Pitch Angle	108

List of Figures

Figure 2.1 Vertical profile of the wind speed (green), the air density (blue) and the wind power density (black) [15].	24
Figure 2.2 Wind power density that exceeded 5, 32, 50, 68 and 95% of the time between 1979-2006 with respect to the elevation [16].	24
Figure 2.3 Wind power global capacity and annual additions, 2005-2015, [7].	25
Figure 2.4 Growth in size of wind turbines since 1980 and prospects, [24].	25
Figure 2.5 83.5 m long blade for Samsung S7.0-171 wind turbine [27].	26
Figure 2.6 Tower diameter limited by bridge height (4.3 m) [28].	26
Figure 2.7 Evolution of institutions actively involved in AWE [31].	27
Figure 2.8 Working principle of the pumping kite power system. Top: generation phase. Bottom: retraction phase. Modified from [13].	28
Figure 2.9 Typical power production. Modified from [11].	28
Figure 2.10 Fly-Gen AWE system, modified from [8]. Left: AWE system flying crosswind, similar to Makani Power. Right: AWE system flying at natural wind, similar to Altaeros Energies.	29
Figure 2.11 Wind window represented with the zenith position and crosswind flight. Modified from [10].	29
Figure 2.12 Close look of the velocity triangle for crosswind flight. Modified from [13].	29
Figure 2.13 De Wachter analysing a 6 m ² ram-air kite in the 8 x 6 m wind tunnel test section [42].	32
Figure 2.14 Car test rig designed by Alexander and Stevenson [44].	34
Figure 2.15 Detailed view of the car test rig arrangement [44].	34
Figure 2.16 Towing test rig designed by Dadd [46].	34
Figure 2.17 Schematic view of the test rig designed by Costa [47].	34
Figure 2.18 Schematic design of the towing test bench (TETA) developed by Hummel [49].	34
Figure 2.19 10 m ² North Vegas kite towed by the TETA setup. Modified from [50].	34
Figure 2.20 Circular test rig designed by Alexander and Stevenson. Green dashed lines: the kite path. White dashed lines: kite lines projection. Red dashed lines: circular vehicle path. Modified from [44].	35
Figure 2.21 Schematic top view of the testing method employed by van der Vlugt [43].	37
Figure 2.22 TU Delft prototype used by Ruppert [54].	37
Figure 2.23 Test bench of Politecnico di Torino used by Fagiano. Modified from [53].	37
Figure 2.24 Angles representation as defined by Costa. Modified from [47].	39
Figure 2.25 Mounting of an IMU and its orientation with respect to the chord line. Modified from [11].	39
Figure 2.26 Aerodynamic coefficients achieved by Costa [47]. $\Delta\phi_c$ indicates the azimuth downwind deviation. Red: curve fitted for $V_a = 14$ m/s. Black: curve fitted for $V_a = 16$ m/s. Dashed: curve fitted on scattered data.	40
Figure 2.27 Glide ratio obtained by Ruppert [11] during generation (red), transition (blue) and retraction (green). Black: weighted linear least squares fitting curve.	40

Figure 2.28 L/D vs BL% for a 3.2 m ² kite for different testing days established by Stevenson. Modified from [44].	41
Figure 2.29 Two distinct α stemming from the same BL% [43].	42
Figure 2.30 L/D vs BL% for a 6 m ² kite investigated by van der Vlugt. Modified from [43].	42
Figure 2.31 Glide ratio for different wind speed expressed versus the brake position from de Wachter. Modified from [42].	42
Figure 2.32 Glide ratio for different kites assessed by Hummel. Modified from [48]. First column: abbreviation of the kite name. Second column: number of maneuvers performed.	43
Figure 2.33 Flat wing area. Modified from [57].	45
Figure 2.34 Projected wing area A_{proj} . Modified from [57].	45
Figure 2.35 Kite models with different levels of complexity. Modified from [48].	46
Figure 2.36 Tether sag [11].	47
Figure 2.37 Schematic representation of the distributed drag equivalent to drag lumped to the kite.	47
Figure 2.38 Free body diagram used by van der Vlugt to consider the tether weight [54].	48
Figure 4.1 Hydra V5. Modified from [64].	51
Figure 4.2 Vegas 2015. Modified from [65].	51
Figure 4.3 Pütznitz airfield, 1.5 km long track. Modified from [50].	52
Figure 4.4 TETA towing test bench. Modified from [50].	53
Figure 4.5 Close view of the angular sensors. Modified from [50].	53
Figure 4.6 Wind window with constant glide ratio (red plane) [50].	53
Figure 4.7 Dynamic maneuvers, 0 - 100% power within 4 seconds, for the Hydra V5 at 22 kt.	54
Figure 4.8 Static maneuvers with constant power setting, for the Hydra V5 at 22 kt.	55
Figure 4.9 Schematic setup to assess the power ratio angle ε .	56
Figure 4.10 Angular sensor mounted on carbon rod.	56
Figure 5.1 Point model without mass (left) and with mass (right).	58
Figure 5.2 Components of the apparent tether weight F_{gt} for a magnitude of 10 [N].	59
Figure 5.3 Force acting on an elemental length of a kite tether.	61
Figure 5.4 Pitch angle variation with respect to the power ratio.	62
Figure 5.5 Close view of the full power situation. Blue: unknown angles. Yellow: measured angles. Red: geometry angle.	62
Figure 6.1 Raw and filtered data of the elevation angle Θ_w for one dynamic maneuver.	64
Figure 6.2 Apparent elevation angle ϑ_w .	65
Figure 6.3 Tether force F_t .	65
Figure 6.4 Raw and filtered data of the elevation angle Θ_w for short sequence of static maneuver.	65

Figure 6.5 Apparent elevation angle ϑ_w of individual samples (grey) and their corresponding median (red) for each power ratio step. The number above the grey scale indicates the number of samples observed.....	66
Figure 6.6 Tether force F_t of individual samples (grey) and their corresponding median (red) for each power ratio step. The number above the grey scale indicates the number of samples observed.....	66
Figure 6.7 Process flow	66
Figure 6.8 Median +/- MAD of the aerodynamic properties computed from dynamic maneuvers for the Hydra V5 flying at 22 kt.	68
Figure 6.9 Relative error $MAD/median*100$	69
Figure 6.10 Median and MAD of the aerodynamic properties computed from static maneuvers for the Vegas 2015 at 22 kt (blue), for the Mixt at 22 kt (green), for the Hydra V5 at 22 kt (orange) and at 29 kt (yellow).....	70
Figure 6.11 Sawtooth profile of the force in the power line.	71
Figure 6.12 ϑ_w and G for the Hydra V5 at 22 kt. Green: median +/- MAD of dynamic maneuvers. Purple: result of dynamic maneuvers obtained by Hummel [48]. Orange: median +/- MAD of static maneuvers.	71
Figure 6.13 Median and MAD of the aerodynamic properties computed for the Hydra V5 at 22 kt. Green: dynamic maneuvers. Orange: static maneuvers.	72
Figure 6.14 Power ratio and apparent elevation angle. Yellow shading: dynamic powering maneuver.	73
Figure 6.15 Structure and interpretation of Figure 6.16.	74
Figure 6.16 Kite and tether weight, drag and lift tether effects on aerodynamic performances for the Hydra V5 at 22 kt. Left axis: effective value. Solid orange: no correction. Solid blue: mass incl.. Solid yellow: tether aerodynamic incl.. Solid green: global correction. Right axis: contribution of kite mass (dashed blue), tether mass (dash-dotted blue), tether drag (dashed yellow), tether lift (dash-dotted yellow).	75
Figure 6.17 Sensitivity analysis of the tether diameter d_t on the glide ratio variation ΔG due to tether drag effect ΔD_t	76
Figure 6.18 Tether sag for power ratio of 10% (blue) and 90% (orange), in comparison to straight tether (dashed black).....	78
Figure 6.19 Aerodynamic performances for the Hydra V5 at 22 kt obtained from different refinement models. Solid orange: no correction, median +/- MAD, $V_w = 0$ m/s. Solid green: global correction from lumped forces (Chap 6.5), $V_w = 0$ m/s. Dashed green: correction from sag model, $V_w = 0$ m/s. Solid blue: correction from sag model, $V_w = 2$ m/s.....	79
Figure 6.20 Tangent relationship between elevation angle β and glide ratio G . Dashed lines shows the difference in G for $\beta = 82.66^\circ$ and $\beta = 86.06^\circ$ which correspond to the angles for 50% power ratio (Table 6.2).	80
Figure 6.21 Power ratio angle ε with respect to the power position (alternatively power ratio). Blue: measurement with 36 cm power range lines. Orange: extrapolation for 50 cm power range lines.	81
Figure 6.22 Pitch angle ψ versus the power ratio, evaluated with β_g (dashed line) and β_k (solid line).	81

Figure 6.23 Aerodynamic properties for the Hydra V5 at 22 kt obtained from the tether sag model (Chapter 6.6) and expressed with respect to the different pitch angle derivations. Dashed lines considered the elevation angle at the ground β_g whereas solid lines the elevation angle at the kite β_k	82
Figure 6.24 Aerodynamic properties assumed by Fechner [72] and adopted for the reverse calculation process.....	83
Figure 6.25 Theoretical (blue) and experimental (green) pitch angle with respect to power ratio.	83
Figure 6.26 Instantaneous pitch angle ψ versus the elevation angle β_k for each power ratio. Black dots: median.....	84
Figure 6.27 Instantaneous lift coefficient versus the pitch angle for 10% of power ratio with median +/- MAD (red).	84
Figure 7.1 Typical lift polar curve. Modified from [73].	87
Figure 7.2 Example of the power range of the line system (blue) and the power range of two distinct kites, namely Kite A of 400 mm (orange) and Kite B of 300 mm (green) power range.	88
Figure 7.3 Glide ratio, lift coefficient (solid line) and drag coefficient (dashed line) for an increase in V_a of +25% (orange), of +50% (yellow), for a d_t of 1 mm (purple), of 2 mm (green) and for default value (dark blue).	91
Figure 10.1 Wind power density for 80 m and 500 m, that was exceeded 50, 68, 95% of the time between 1979-2006 [75].	99
Figure 10.2 Kitepower system fitted into a freight container. Modified from author's picture.	101
Figure 10.3 Simens SWT-6.0-154, 120 m hub height, 75 m long blade, from [78].	101
Figure 10.4 Mass effect on aerodynamic performances for the Hydra V5 at 22 kt. Orange: massless case with median +/- MAD and polyfit. Blue: kite mass included. Yellow: tether mass included. Green: both kite and tether mass included.	105
Figure 10.5 Drag and lift effect of the tether on aerodynamic performances for the Hydra V5 at 22 kt. Orange: tether neglected, median +/- MAD and polyfit. Blue: tether drag included. Yellow: tether lift included. Green: both drag and lift included.	106
Figure 10.6 Aerodynamic properties expressed with respect to the hypothetical pitch angle obtained by doubling the value of the power ratio angle. Dashed lines considered the elevation angle at the ground whereas solid lines the elevation angle at the kite.....	107
Figure 10.7 Instantaneous aerodynamic properties for the Hydra V5 at 22 kt obtained from the tether sag model (Chapter 6.6) and expressed with respect to the pitch angle.	108

List of Tables

Table 2.1 Roughness length for Log Law [15]	44
Table 2.2 Power Law exponent [15]	44
Table 4.1 Kite characteristics	51
Table 4.2 Sensor accuracy	54
Table 4.3 Accuracy of computed values	54
Table 4.4 Experiment summary	55
Table 6.1 Channel outputs.....	63
Table 6.2 Tether sag effect	77
Table 7.1 Accuracy of computed values	89
Table 7.2 Source of error	90

Nomenclature

Latin Symbols

A_{proj}	Wing projected area	m^2
A_{ref}	Reference area	m^2
A	Axial force	N
$BL\%$	Back line force ratio	[-]
C_A	Axial force coefficient	[-]
C_D	Drag coefficient	[-]
$C_{D,t}$	Tether drag coefficient	[-]
C_N	Normal force coefficient	[-]
C_L	Lift coefficient	[-]
C_p	Wind turbine power coefficient	[-]
C_R	Resultant aerodynamic coefficient	[-]
c_t	Tether loading constant	[-]
D	Drag force	N
D_k	Kite drag force	N
d_t	Tether diameter	m
D_t	Tether drag force	N
$D_{t,e}$	Equivalent tether drag force	N
D_p	Drag force experienced by on-board turbines due to their operation	N
F_a	Resultant aerodynamic force	N
$F_{g,t}$	Lumped tether gravity force	N
F_{LS}	Left steering line force	N
F_P	Power line force	N
F_{RS}	Right steering line force	N
F_S	Total steering line force	N
F_t	Tether force	N
G	Glide ratio, lift-over-drag ratio	[-]
G_e	Effective glide ratio	[-]
L	Lift force	N
$L_{t,e}$	Equivalent tether lift force	N
l_t	Tether length	m
m_k	Kite mass	kg
m_t	Tether mass	kg
Ma	Mach number	[-]
$M_{D,t}$	Momentum generated by the tether drag force around the ground station	Nm
N	Normal force	N
P_m	Mechanical power output	W
$PR\%$	Power ratio	[-]
q_∞	Dynamic pressure	$kg/m/s^2$
Re	Reynolds number	[-]
S	Swept area	m^2
V_a	Apparent wind velocity	m/s
V_{car}	Car velocity	m/s
V_k	Kite velocity	m/s
V_t	Tether reel-out velocity	m/s
V_w	Free stream velocity, natural wind speed	m/s

WPD	Wind Power Density	W/m^2
z	Elevation from ground level	m
z_0	Surface roughness length	m
z_{ref}	Reference height	m

Note:

Symbols listed above refer to their magnitude. When their vectors are considered, the above symbols are modified in bold. For instance, L refers to the lift magnitude whereas \mathbf{L} corresponds to the lift vector.

Greek Symbols

α	Angle of attack	degree
α	Power Law exponent	[-]
β	Tether elevation angle	degree
γ	Wind direction angle	degree
δ	Intrinsic chord angle	degree
Δ	Absolute error	cf. unit
ε	Power ratio angle	degree
ζ	Angle at the handle bar junction	degree
η	Offset angle	degree
θ	Polar angle of spherical coordinates	degree
θ_0	Elevation angle from angular sensor	rad
θ_w	Computed elevation angle from angular relationship	rad
ϑ_w	Apparent elevation angle	degree
ρ_{air}	Air density	kg/m^3
ρ_t	Tether density	kg/m^3
ρ'_t	Linear tether density	kg/m
φ	Azimuthal angle of spherical coordinates	degree
Φ_{01}	Azimuthal angle from angular sensor	rad
Φ_{02}	Pivot angle from angular sensor	rad
Φ_g	Computed azimuthal angle from angular relationship	rad
Φ_w	Computed azimuthal angle from angular relationship, wind included	rad
χ	Wind direction angle	rad
ψ	Pitch angle	degree

Subscript

e	Equivalent
g	At ground level
k	At kite location
t	Tether

Abbreviation

AoA	Angle of attack
AWE	Airborne Wind Energy
AWEC	Airborne Wind Energy Conference
CFD	Computational Fluid Dynamic
CH	Switzerland
COP21	21 st Conference Of the Parties
cst	Constant

DE	Germany
DK	Denmark
EWEA	European Wind Energy Association
FSI	Fluid-Structure Interaction
GB	Great Britain
IEA	International Energy Agency
IMU	Inertia Measurement Unit
IT	Italy
LCOE	Levelized Cost Of Energy
MAD	Median Absolute Deviation of the Median
NL	Netherlands
NZ	New Zealand
PV	Photovoltaic
REN21	Renewable Energy Policy Network for the 21 st Century
SLE	Supported Leading Edge
STD	Standard Deviation
TETA	Test and Evaluation of Tethered Airfoils
TPES	Total Primary Energy Supply
TU	University of Technology
UN	United Nations
WPD	Wind Power Density

1 Introduction

Nowadays, the world is facing an energy transition challenge. The constant growth of world population together with welfare development of societies lead to a continuous increase of energy demand. According to the International Energy Agency ([IEA](#)), the Total Primary Energy Supply (TPES) was increased by a factor of 2.5 between 1971 and 2014 [1], while for the same period the United Nations ([UN](#)) have recorded that the world population was almost doubled [2]. In order to supply this tremendous amount of energy, the power production mainly relies on fossil fuels (81.2% in 2014 [1]).

Despite the high energy density of these combustibles, fossil fuels have however negative environmental side effects. Indeed, they account for a large part for production of carbon dioxide (CO₂), which acts as a greenhouse gas and strongly contributes to global warming. From 1750 to 2000, the atmospheric CO₂ concentration has risen by 31% and the current level of CO₂ has never been experienced during the last 420'000 years [3]. Not only scientific experts but also politicians are aware of the risk of temperature rise. In December 2015, 195 countries have concluded the first international climate agreement during the Paris Conference ([COP21](#)). Together, they agreed on limiting the temperature rise to below 2°C with respect to pre-industrial level [4].

In addition to fossil fuels, nuclear energy also plays a role in the global power production. Although its proportion is relatively small compared to fossil fuels (4.7% of the world power production in 2014 [1]), nuclear energy has always been a delicate subject. The main discussion lies in the safety aspect of the power plants. Chernobyl (1986) and Fukushima (2011) nuclear disasters are only two examples which present the sensibility and complexity of this technology. Furthermore, the radioactive waste management is a topical issue. For instance, Switzerland is currently investigating 6 potential sites for deep geological repository, which is thought by the experts community to be the only long term safe solution [5].

These first statements illustrate that the current power production is not sustainable in the long term. In order to succeed in the energy transition, renewable energies have to be further developed to compete with fossil energies. In the last decade, wind energy has become one major actor in the field of clean energies. The global cumulative installed wind capacity raised from 59 GW in 2005 up to 433 GW in 2015 (+633%) [6], which represents about 23.5% of the world renewable power, just behind hydro power (57.5%). However, the hydro power capacity has increased only by 2.7% (+28 GW) in 2015 whereas the wind energy has grown by 17% with a record addition of 63 GW [7]. This shows the fast development of wind energy as a renewable energy.

However, in order to reach higher power outputs, wind turbines tend to become huge, consisting of heavy structures. At a certain point, increasing the size of a wind turbine is not financially beneficial anymore [8]. Besides this structural limitation, the wind condition at low altitudes is not always constant and relatively difficult to forecast for long term. Therefore, the power output delivered by conventional wind turbines strongly varies in time and solutions to stabilize the power grid have to be considered. As a consequence, new concepts of wind energy harvesters are developed targeting high altitude winds. This technology is referred to as Airborne Wind Energy (AWE) technology [9] and takes advantage of more powerful and more constant winds available at high altitudes.

Pumping cycle kite power system is one of the concepts which belongs to AWE technology. It consists of a lightweight kite connected by a tether to a ground based drum coupled to a generator. As its name suggests, the process is com-

posed by a two-phase cycle, namely the traction phase and the retraction phase. During the traction phase, energy is extracted from the wind. The kite flies crosswind and develops a strong pulling force. Thus, the tether is reeled out from the drum and drives the electrical generator. When the tether has reached its maximal length, the retraction phase starts. The aerodynamic characteristic of the kite is adjusted in such a way that the traction force is significantly reduced. Therefore, only a fraction of the previously extracted energy is required to pull the kite back to its initial position. This results in a net amount of energy generated per cycle and the process can start again. Several companies are involved in the race of developing a first commercial AWE system. Just to name a few, [Kitepower](#) (NL), [Kite Power Solutions](#) (GB) and [KiteGen](#) (IT) operate thanks to a flexible kite while [EnerKite](#) (DE), [TwingTec](#) (CH) and [Ampyx Power](#) (NL) use a rigid wing. Both systems have their own advantages and disadvantages.

So far, pumping kite power systems mainly operate with soft wings derived from the kitesurf industry. Surf-kites are designed by adopting a trial-and-error method using several prototypes and their performances are iteratively assessed in qualitative manner by kite surfers until the final design is reached [10]. On the side of kite power systems however, evaluation of the wing performance requires more quantitative considerations since the power output of the system strongly depends on it. The main aerodynamic requirement for a kite with the purpose of power generation is a high lift-to-drag ratio which leads to a strong pulling force during traction phase [11]. In addition to that, the depower ratio, namely the ratio between the force during reel-in and reel-out phases, is required to be significant to limit the amount of energy lost during retraction phase [12].

In order to evaluate and optimize the entire power system, most research groups are implementing computer models varying in complexity. Numerical simulations give a great help in designing such complex systems. However aerodynamic performances coefficients of the wing, which are required for dynamic flight model, are in the case of soft wings not always well known. For instance, lift-to-drag ratio is commonly set with best guessed values, for example, from rigid airfoil theory and might not faithfully correspond to the actual soft wing. As a consequence, a small discrepancy in the input of the model might lead to a significant error in the simulated output. A precise characterization of the aerodynamic performance of the kite would not only improve the prediction of power output but could also provide more insight on how the kite design should be adjusted to reach better performances.

Several possibilities in assessing the wing performance are available. Among them, numerical modelling has gained in popularity with the increase of computer performances. From the simple 2D computational fluid dynamic (CFD) to the more complex 3D fluid-structure interaction [13], numerical modelling offers the possibility to test variable parameters without the need of manufacturing a real prototype. However, complex simulations might require significant computer resources and could potentially lead to extensive simulation time (up to weeks or even more). Moreover, although numerical models aim at studying the behaviour of the wing and establishing its performances, validation of the model is still required to ensure it accurately represents the real situation [14]. This validation is made by comparing results obtained from both numerical and experimental methods.

Unfortunately, the number of quantitative kite experiments is relatively limited due to the difficulties in obtaining the kite performance characteristics during flight. An alternative in measuring the kite state is to perform wind tunnel test. This allows to control environmental parameters, such as flow velocity, pressure or temperature, which at the end facilitate the repeatability of the test. One main downside of the wind tunnel testing, besides expensive costs, is the scalability aspect [12]. Indeed, due to the large size of the kite, not all wind tunnels can offer the possibility of testing such structure. Therefore, the kite has to be scaled down while respecting similarity parameters. The dynamic similarity, given by the Reynolds number (Re) together with the geometrical similarity could lead to a non-feasible geometry because of material limitation. Moreover, the aero-elasticity behaviour of the down-sized kite model is not guaranteed to be similar to the real kite. In other words, the acquisition of experimental data for the purpose of numerical model validation is still a challenging question for flexible kite wings.

Recently, a car towing test bench, *Test and Evaluation of Tethered Airfoils* ([TETA](#)), has been developed at TU Berlin (DE) to evaluate the in-flight state of flexible kites in an automated and repeatable manner. As a first step, a simple analytical model is used to compute the aerodynamic properties obtained from dynamic maneuvers. In this context,

the present thesis takes advantage of this new test bench to provide validation data for ongoing numerical simulation research by experimentally assessing the Kitepower wing. As a first research question, two distinct testing methodologies for acquiring kite state are applied and compared. Measurement from dynamic maneuvers of the kite are confronted with data achieved from static maneuvers. A point mass model is implemented to compute the aerodynamic efficiency of the wing from the measured forces and angles obtained by the two distinct methodologies. As a second point, additional influences such as tether drag and weight, so far neglected, are considered to improve the point mass model. Their influences on the final results are analysed. The sag of the tether and its direct effects on the kite aerodynamic properties are investigated as a third research question. Eventually, it is intended along the fourth research question to assess the kite angle of attack by relating the bridle configuration to the kite geometry. In this way, the aerodynamic properties of the kite can be expressed with respect to the angle of attack, which makes it more appropriate not only for numerical simulation but also for kites comparison.

Following this Introduction, the literature study first exposes some features of the natural wind for different altitudes and depicts how conventional and new types of wind energy harvesters are being developed accordingly to achieve greater power output. Then, a description of the current state of the art regarding kite experiments details distinct testing methods for assessing the aerodynamic properties. Eventually, the background theory and the theoretical models regarding kite and tether are exposed. Thesis goal and approaches are deepened before detailing the experimental setup and methodologies used for this work. Next, the distinct theoretical models adopted are explained before presenting the results for each research question. Finally, recommendations are suggested, before giving a conclusion for the overall work.

2 Literature Study

This chapter provides the relevant background information. First, the natural wind is presented in Chapter 2.1 for different altitudes and illustrates the great potential of the energy contained within the winds. Then, in Chapter 2.2 the evolution of wind energy market around the world is exposed. The progress in wind turbine technology is also described and discloses reasons for the growing interest in Airborne Wind Energy systems. Eventually, a focus on Airborne Wind Energy, its different systems and its advantages are presented along Chapter 2.3. The state of the art regarding experimental research is presented in Chapter 2.4. Distinct innovative methods to assess the kite performances are listed and described in detail. In addition, origins and reasons for choosing one or another variable for expressing the aerodynamic curves are also given. Eventually, background theory regarding wind and kite aerodynamic as well as theoretical models are exposed and detailed in Chapter 2.5.

2.1 Natural Wind

Physically speaking, wind is a mass of air in movement. This movement is induced by a complex interaction of five factors occurring at different scales [15]. First, the differential earth heating leads to pressure gradients around the globe, which drives air from high to low pressure regions. Second, the earth rotation engenders the Coriolis force and affects the air movement by changing its apparent acceleration. Third, gravity also enters into the equation of motion. Fourth, wind shear and buoyancy create rotating air motions called eddies which convert into turbulences. Eventually at small scale, air viscosity is also taken into account since it slows down the movement of air. The last two terms, namely the wind shear and the viscosity, tend to be more significant as the distance to the ground level reduces. In contrast, both frictional and turbulent terms can be neglected above a certain altitude. Characteristics for low and high altitude winds are described in the following chapter. The global wind potential is detailed in Annexe 10.1 for more information.

2.1.1 Low Altitude Wind

A vertical wind speed gradient arises from both frictional and turbulent factors which play an important role within the boundary layer [15]. As a consequence, the wind speed generally increases with altitude. However, it is important to mention that the air density reduces with height [11]. Both features have a direct effect on the available power, namely the wind power density (WPD), which is given by Equation (2.1). The WPD grows linearly with air density ρ_{air} while it increases with the cube of the wind speed V_w . Thus, if the wind velocity is doubled, the available wind power increases by a factor of eight. This situation is illustrated in Figure 2.1, on which two different wind laws, namely the Power Law (green solid line) and the Log Law (green dashed line), are exposed for a reference wind speed of 3 m/s over crop fields. Both laws, explained in more detail in Chapter 2.5.1, include terrain characteristics such as roughness and are valid up to 500 m [15]. The wind power density shows a rapid increase the first hundreds of meters. For instance, the WPD is 50 W/m² at 80 m (conventional wind turbines height) whereas at 400 m (typical AWE system height), its value almost doubles. From this, the interest in harvesting wind energy at higher altitudes is no more questionable.

$$WPD = \frac{1}{2} \rho_{air} V_w^3 \quad (2.1)$$

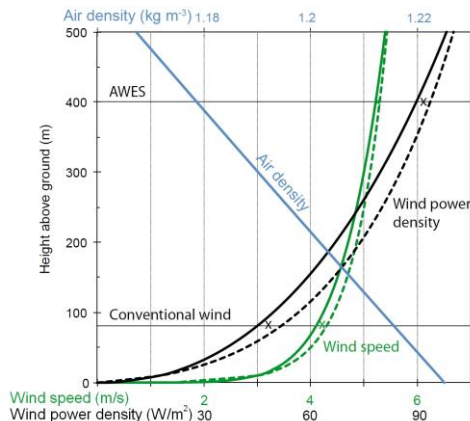


Figure 2.1 Vertical profile of the wind speed (green), the air density (blue) and the wind power density (black) [15].

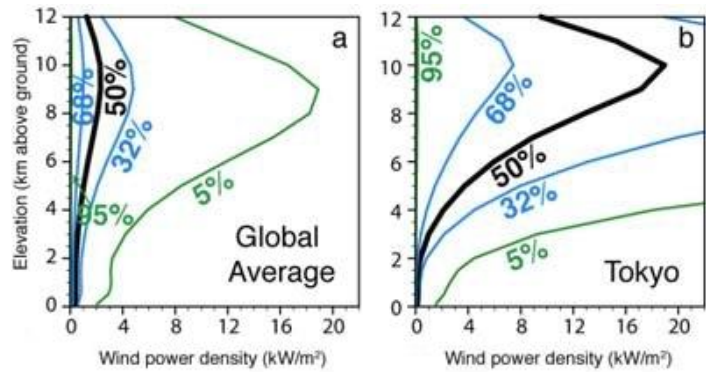


Figure 2.2 Wind power density that exceeded 5, 32, 50, 68 and 95% of the time between 1979-2006 with respect to the elevation [16].

2.1.2 High Altitude Wind

Above 500 m, both frictional and turbulent effects are usually negligible whereas the Coriolis and pressure gradient forces are mainly dominant [15]. Such implications, which hold well within the atmospheric upper levels, lead to the so-called geostrophic flow. In this case, the wind speed generally intensifies with elevation while the air density declines nearly exponentially above the boundary layer [16]. This results in a different distribution of available wind power compared to low altitude one. Figure 2.2 presents the situation of the WPD for the global average and the city of Tokyo. The different percentage lines indicate the proportion of time between 1979 and 2006 during which the corresponding wind power density was exceeded. When comparing the global average against Tokyo, it can be deduced that the available wind power is not distributed evenly around the globe. Furthermore, focusing on the global average, it is worth mentioning that between 500 and 2000 m, the WPD does not significantly vary whereas above 2000 m, the available wind power constantly increases with height [15]. As a consequence, this suggests that wind energy harvester would not achieve more gain in going above 500 m, unless it extracts wind energy above 2000 m.

2.2 Wind Turbine Energy

According to the Renewable Energy Policy Network for the 21st Century ([REN21](#)) [7], [17], renewable energy share has grown during the last decade from 880 GW in 2005 up to 1849 GW in 2015 (+110%), which currently represents 19.2% of the global final energy consumption. Among all clean energies, wind energy has strongly expanded over the same period. In 2005, the world wind power capacity accounted for 6.7% of the total renewable energy whereas in 2015, it represented 23.5%. In comparison, hydro energy, the top first clean energy, provided 88.7% of the total renewable energy in 2005 and dropped down to 57.5% in 2015.

As it is presented in Figure 2.3, the global wind power capacity has raised by +633% from 59 GW to 433 GW within the last 10 years. For the same period, the hydro power sector grew from 781 to 1064 GW (+36%). In other words, although the hydro power capacity is still greater than the wind power capacity, the wind energy sector evolved significantly faster compared to the hydro technology. This fast-growing wind power evolution is not expected to stabilise straightaway. Indeed, more than half of the worldwide wind power capacity has been installed over the last 5 years. Furthermore, 2015 was an exceptional year with a record addition of 63 GW of wind power to the grid.

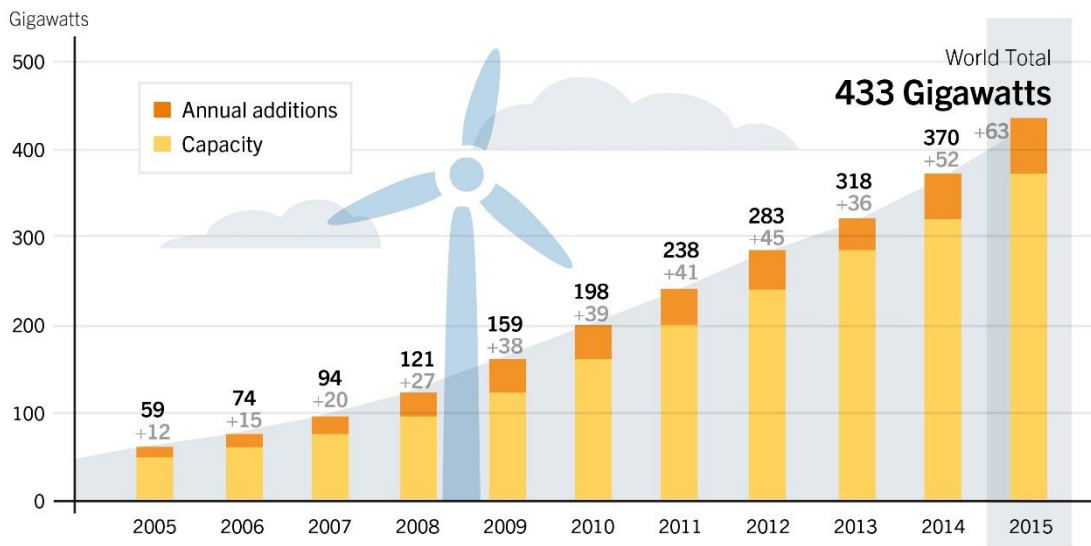


Figure 2.3 Wind power global capacity and annual additions, 2005-2015, [7].

2.2.1 Wind Turbine Evolution

The wind energy market development has been driven notably by the evolution of the wind turbine technology. In 1991, Enercon Company (DE) manufactured the world’s first direct drive train wind turbine [18]. According to the European Wind Energy Association (EWEA) [19], this innovation was particularly noteworthy. Since then, new technological developments have followed: variable speed electronical and pitch control systems, power electronics and blade material improvement are only a short list of them. However, the most outstanding progression in recent years has been the evolution in larger and more imposing wind turbines [19]. Figure 2.4 illustrates this striking trend since 1980. At the time of drafting this report, the world’s biggest wind turbine currently installed is reported by several specialized magazines ([20], [21]) and DONG energy (DK) [22] to be the offshore Vestas V164-8.0 MW at Burbo Bank Extension (GB). The 220 m high staggering structure is composed by three 80 m long blades, weighing 33 tons apiece. The total swept area (21124 m²) is equivalent to three soccer fields [23].

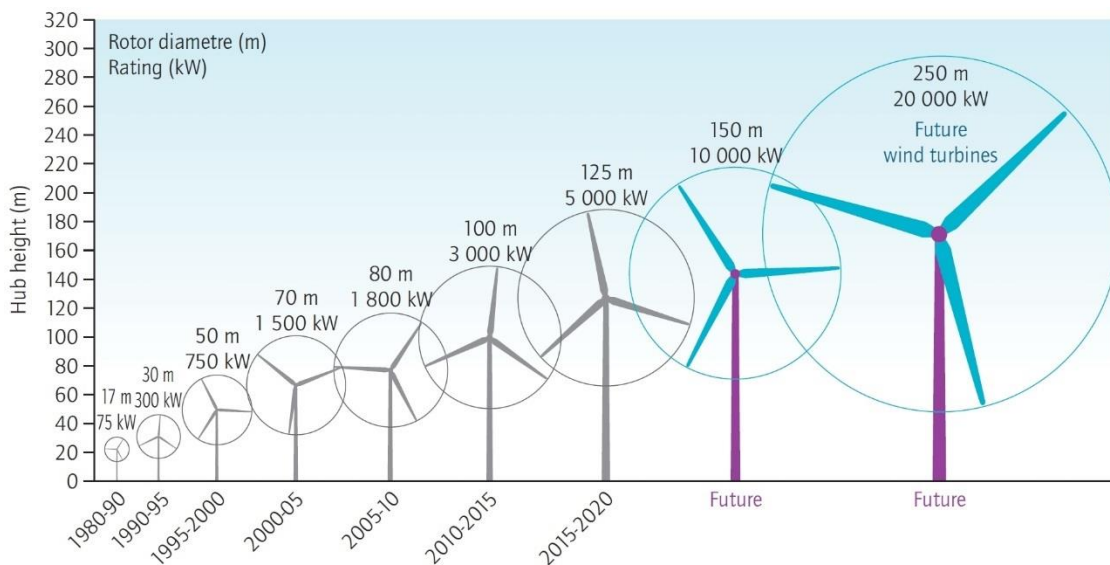


Figure 2.4 Growth in size of wind turbines since 1980 and prospects, [24].

The trend of increasing the rotor diameter has been driven by the fact that wind turbine mechanical power output is directly related to the blade swept area S by Equation (2.2). Thus, doubling the blade length will quadruple the mechanical power output.

$$P_m = C_p S WPD = C_p S \frac{1}{2} \rho_{air} V_w^3 \quad (2.2)$$

Wind turbines convert the kinetic wind power into mechanical power, thus the wind power density comes into account. The power coefficient C_p specifies the amount of power that is actually converted from the wind into mechanical power. The theoretical maximum power coefficient has been established by German physician Betz back in 1919 [25]. He showed that no conventional horizontal axis wind turbine can extract more than 59.3% of the wind kinetic energy. From Equation (2.2) and as already mentioned in Chapter 2.1.1, doubling the incoming wind speed will increase the power output by eight-fold. Therefore, another reason for placing the rotor in higher altitudes is to take advantage of more energetic winds [26] as introduced along Chapter 2.1.

These technical improvements have led to a general increase in capacity factor and to a reduction in levelized cost of energy (LCOE) especially in low-wind-speed locations [24]. However, wind turbines are not expected to develop in size as fast in the future as they have previously. Blades longer than 100 m would be technically possible for land-based wind turbine but other potential barriers such as transportation and installation of the huge components would have to be overcome, as suggested in the following Figure 2.5 and Figure 2.6



Figure 2.5 83.5 m long blade for Samsung S7.0-171 wind turbine [27].

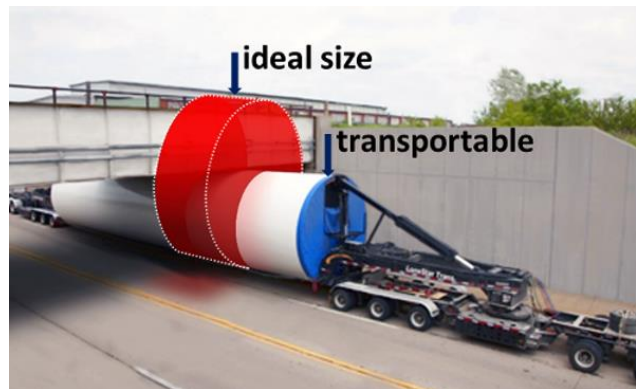


Figure 2.6 Tower diameter limited by bridge height (4.3 m) [28].

But on top of that, the main reason for a size limit for wind turbines arises from the “square-cube law” [26]. This law states that “as a wind turbine rotor increases in size, its energy output increases as the rotor-swept area (the diameter squared), while the volume of material, and therefore its mass and cost, increases as the cube of the diameter.” This means that, at a certain point, an increase in wind turbine size will not result in an economical benefit anymore. In other words, the cost for a larger turbine will surpass the energy output earnings. Nevertheless, the high wind energy potential above 200 m is gaining more and more interest. In this context, a new generation of renewable energy systems has emerged out of the scientific community: the Airborne Wind Energy systems.

2.3 Airborne Wind Energy

In 1980, the American engineer Loyd published his article “Crosswind Kite Power” [29] in which he provides the underlying theory for Airborne Wind Energy system and assesses the energy that could theoretically be harvested by such concepts. Since then and for the rest of the 20th century, the AWE sector rather stayed constant because of the significant development in wind turbine technology and market. However, in early 2000s, the progress in tether and control technologies together with the limitation of wind turbine size increase led to a renewed impetus to AWE concepts [30]. Indeed, since 2000, multiple worldwide academic research groups and commercial companies have joined the Airborne Wind Energy sector every year, as illustrated in Figure 2.7. In 2010, the first Airborne Wind Energy Conference (AWEC) was organised in Stanford with the ambition of gathering institutions active in the AWE sector from all around the world. Since then, one yearly international conference is held alternatively in Europe and in the US.

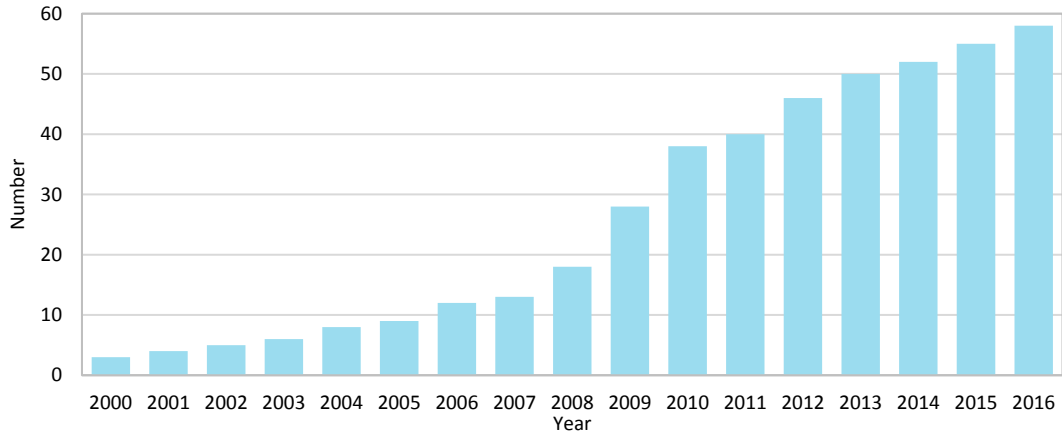


Figure 2.7 Evolution of institutions actively involved in AWE [31].

Airborne Wind Energy technology refers to an electro-mechanical machine that converts the wind kinetic energy into electrical energy [8]. Unlike conventional wind turbines, AWE systems are able to harvest wind energy from medium to high altitudes with a low material investment [32]. In general, such systems consist of two main components namely a stationary or moving ground station and an airborne device. The latter could be a lightweight aircraft, a rigid wing, a flexible kite or an aerostat. In addition, the flying device is connected to the ground thanks to at least one tether. Cherubini provides in his paper [8] a wide and exhaustive overview of the current existing technologies and companies involved in Airborne Wind Energy.

Within the AWE system designs, one common classification is based on the location of the electrical energy transformation. A clear distinction can be drawn between concepts with a ground-based generator (ground-gen, Chapter 2.3.1) and those operating with on-board generator (fly-gen, Chapter 2.3.2). Although this thesis aims at investigating exclusively ground-based AWE systems, a description of both systems is presented in the following sections. Later on, the concept of crosswind flight introduced by Loyd is presented along Chapter 2.3.3. In order to illustrate the wide strength of Airborne Wind Energy systems in general, their main advantages are exposed in Annexe 10.2 through examples by comparing innovative AWE concepts against conventional power generation systems.

2.3.1 Ground-Gen

As briefly introduced, ground-gen stands for ground-based generator, which means that the electrical power transformation takes place on the ground [8]. In this case, the generator is driven by a strong pulling force which is transmitted from the airborne device to the ground station by means of one or more cables, usually called tethers. Loyd [29] refers this principle to *lift mode* since the aerodynamic lift of the aircraft is mainly responsible for the tether force. Various other terms refereeing to *lift mode* exist in the literature: *pumping kite*, *traction kite* or *yo-yo* [11], [32], [33]. Such designations are derived by the periodical working principle of ground-gen AWE system (Figure 2.8), which can be decomposed into two distinctive phases, namely the generation and the retraction phases.

During the generation phase, the lightweight wing experiences high apparent wind velocity by flying crosswind, which in turn leads to a considerable lift force and therefore to a strong traction of the tether. Hence, the latter is simultaneously reeled out of the drum with the appropriate speed and induces the rotation of the electrical generator [32]. The mechanical power at the drum, given by Equation (2.3), is composed by the product of the tether pulling force F_t and the tether reel-out velocity V_t . As a first approximation, the tether force corresponds to the wing lift force L if the lift coefficient is significantly larger than the drag coefficient [33]. During this reel-out phase, the wind kinetic energy is thus converted into electrical energy. Eventually, due to its finite length, the tether must be wound back into the drum at the end of the generation phase. This brings the process to the beginning of the retraction phase.

$$P_m = F_t V_t \approx L V_t \quad (2.3)$$

As the reel-in phase occurs, the generator changes mode and acts as a motor which then drives the drum. This results in a rewind of the tether around the winch. In order not to consume all the energy produced during the generation phase, not only the crosswind flight is stopped but also the aerodynamic characteristics of the wing are adjusted in such a way that the tether pulling force is significantly reduced [32], [34]. The kite de-power capacity is responsible for this force reduction. Therefore, the energy required to bring the wing back to its initial position during the recovery phase is significantly lower than the energy extracted from the wind during the generation phase. Eventually, this results in a positive net energy generated per cycle and the process can start again. This feature is presented on Figure 2.9 where the yellow and the red colours indicate the energy generated during reel-out phase and the energy spent during reel-in phase respectively.

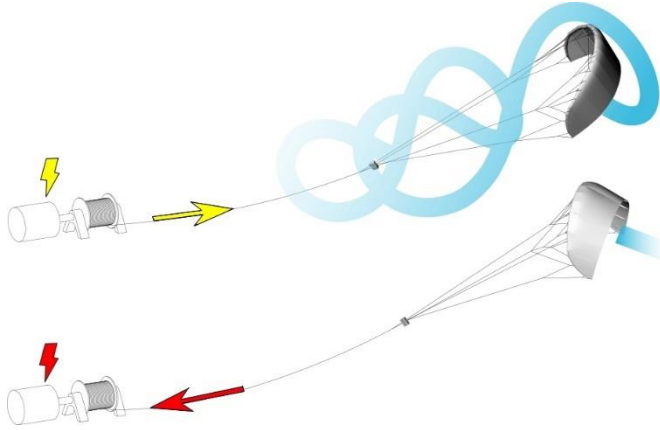


Figure 2.8 Working principle of the pumping kite power system. Top: generation phase. Bottom: retraction phase. Modified from [13].

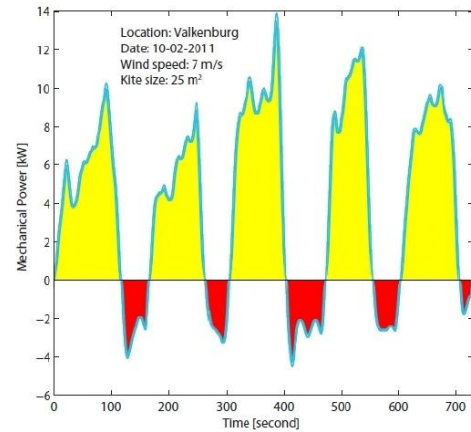


Figure 2.9 Typical power production. Modified from [11].

2.3.2 Fly-Gen

The second way of harvesting wind energy for AWE systems is to convert power directly on-board of the aircraft and then to transmit it to the ground through a special conductive cable of constant length [8]. The airborne device can either take advantage of crosswind flight as presented on the left-hand side of Figure 2.10 or simply experience natural wind as illustrated on the right-hand side of Figure 2.10. Loyd [29] calls this principle as *drag mode* since the on-board wind turbines generate extra drag on the wing.

In case of crosswind flight, the wing experiences high apparent wind speed which induces the on-board wind turbines to spin at high rotation speeds. Hence, the electrical generators do not require a gearbox, which saves weight [32]. The mechanical power delivered by the on-board wind turbines, given by Equation (2.4), is the product of the drag force experienced by the turbines due to their operation D_p and the apparent wind speed V_a [33]. Moreover, unlike the pumping kite power system, the fly-gen system does not operate with a retraction phase and can therefore generate power continuously. However, the on-board wind turbines and generators together with a thicker and heavier cable lead to an increase in weight of the system compared to pumping kite power system, which reduces its performances [11]. Nevertheless, the on-board wind turbines can act as propellers for vertical take-off and landing, by operating generators in motor mode. This is one of the major advantages of fly-gen systems in comparison to ground-gen systems [33].

$$P_m = D_p V_a \quad (2.4)$$

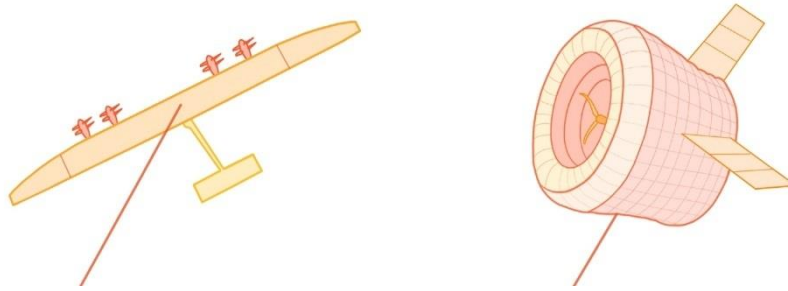


Figure 2.10 Fly-Gen AWE system, modified from [8]. Left: AWE system flying crosswind, similar to [Makani Power](#). Right: AWE system flying at natural wind, similar to [Altaeros Energies](#).

2.3.3 Crosswind

When a kite is flying statically at the zenith position, namely high and straight downwind (Figure 2.11), it only experiences the incoming wind velocity V_w and the tension within the lines is relatively low. In this situation, the kite is not moving with respect to the earth [10]. Hence, the apparent wind speed V_a , namely the air speed that the kite perceives, is equal to the incoming wind speed ($V_a = V_w$). However, as soon as the kite leaves the zenith position and starts to fly within the wind window as illustrated in Figure 2.11, the pulling force in the tether significantly increases [32]. This is due to the fact that the apparent wind speed V_a becomes greater than the natural wind speed V_w when flying crosswind ($V_a > V_w$), as presented on Figure 2.12. Typically, the apparent wind velocity V_a , whose vector is given by Equation (2.5), can be 5 to 10 times greater than the incoming wind velocity V_w [33]. In the case of ground-gen, the increase in apparent wind speed leads to stronger pulling force since the aerodynamic lift force L evolves with the square of the latter as shown in Equation (2.6).

$$\mathbf{V}_a = \mathbf{V}_w - \mathbf{V}_k \quad (2.5)$$

$$L = \frac{1}{2} \rho_{air} A_{ref} C_L V_a^2 \quad (2.6)$$

Lloyd's idea was to take advantage of crosswind flight to achieve great power generation by means of tethered airfoils. Indeed, if the apparent wind speed increases by a factor 10 due to crosswind maneuvers, the tension of the tether intensifies by a factor 100 in comparison to a kite that is flying statically at the zenith position. This leads to an increase of the power output by almost the same ratio (Equation (2.3)) in comparison to static flight.

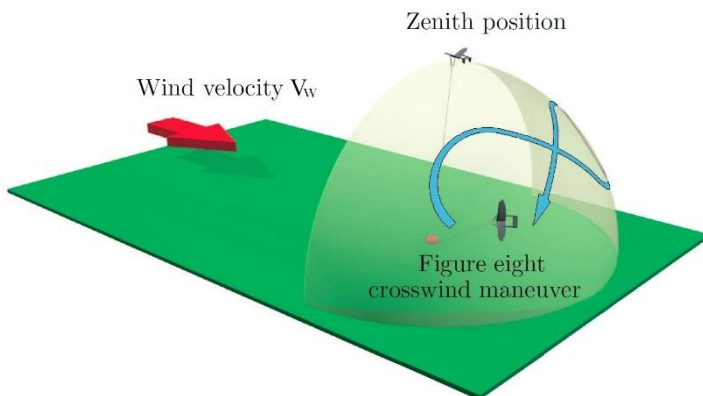


Figure 2.11 Wind window represented with the zenith position and crosswind flight. Modified from [10].

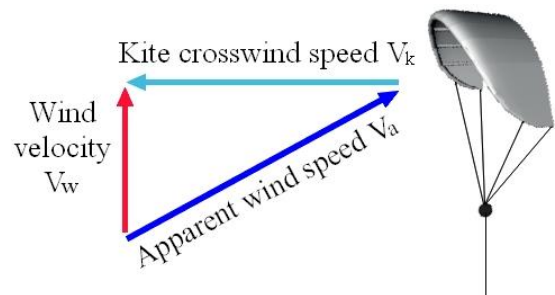


Figure 2.12 Close look of the velocity triangle for crosswind flight. Modified from [13].

Lloyd estimated that both lift and drag principles flying crosswind generate the same amount of power. Under idealised assumptions, the mechanical power output of a tethered airborne apparatus is given by Equation (2.7) [32]. One major aspect is the fact that the wing lift-over-drag ratio C_L/C_D appears quadratically into the formula which makes it an important parameter for AWE system. Therefore, it is of high interest to accurately establish its value in order to

correctly estimate the power output. This ratio is also known in the aircraft industry as the glide ratio G which can be seen as the efficiency of the airfoil. Hence, the term C_L^3/C_D^2 has to be maximized in order to harvest the most wind energy [10].

$$P_m = \frac{2}{27} \rho_{air} A_{proj} V_w^3 C_L \left(\frac{C_L}{C_D} \right)^2 \quad (2.7)$$

2.3.4 Key Factors – Aerodynamic Coefficients

As it has been previously introduced in the Introduction and in Chapter 2.3, the wing efficiency plays an important role in Airborne Wind Energy systems. In order to numerically represent a pumping kite power system, research groups have developed complex computational models which allow various types of simulations. Such models could provide relevant information on the system in general or on specific aspects without the need of manufacturing and testing a real kite prototype. Kite design improvement [10], economic potential analysis [34], mechanical power output estimation [35] and optimal flying trajectories [36] are a short list of simulation prospects.

However, such models commonly require aerodynamic coefficients C_L , C_D and/or L/D as input. Thus, a small inaccuracy in these coefficients directly leads to miscalculation of the model output. As an illustration, it is established in Annex 10.2, that an AWE system with C_L and C_D of 1 and 0.07 respectively, facing a wind speed V_w of 13 m/s could potentially generate 40 kW/m². If the drag coefficient C_D is actually 10% larger, namely 0.077, while other parameters are kept constant, the power density drops to 33.6 kW/m² (Equation (2.7)), which corresponds to a decrease of 16%. This short calculation shows the high relevance of precise coefficients for numerical simulation purposes.

The aerodynamic coefficients are intrinsic properties of a given airfoil. Combining both lift and drag coefficients leads to the L/D ratio, which is usually seen as the aerodynamic efficiency [8], [29]. Generally speaking, a higher L/D leads to better flight performance [37]. The lift-over-drag ratio, also called glide ratio G , can be interpreted for an unpowered wing as the ratio of the horizontal travelled distance over the vertical lost elevation. It plays an important role in pumping kite power system since the mechanical power output of the system is approximately proportional to the square of the kite's lift-over-drag ratio (Equation (2.7)) [38]. Hence, this ratio has to be optimised. A high lift is required to transmit a strong pulling force to the drum during reel-out phase whereas a low drag force aims at reducing the losses [11]. The accurate determination of these coefficients is far from easy though. Although several methods exist in assessing the wing performances, they differ in complexity and accuracy.

For instance, computational fluid dynamic models have recently earned active interest with the growing improvement in computer performance. Indeed, numerical modelling offers the possibility to design, modify and efficiently investigate various aspects of the kites without actually manufacturing them. This greatly simplifies the design loop. Moreover, aerodynamic coefficients can be easily established. To illustrate the popularity growth in numerical modelling, Leloup [39], who has estimated L/D ratio with the lifting line method, enumerates several papers which investigate aerodynamic coefficients by means of 2D simulations, 3D simulations [40], [41], Navier-Stokes simulations [42] and other computational methods. Leloup also claims that the most advanced method of his time was implemented by Breukels [10]. His model, which takes into account the kite deformation, relies on a fluid structure interaction which couples Reynolds-Averaged Navier-Stokes equations for the air with a multibody dynamic simulation for the kite. However, such model requires heavy computer resources and extensive computational time. Furthermore, the numerical approach has to be validated in order to make sure that the model correctly represents the reality [14]. This is usually done by comparing computed results against experimental ones. Unfortunately, such experimental results are not always available.

Other alternatives in defining the aerodynamic coefficients exist on the side of the experimentation. Van der Vlugt [43] suggested several kite testing methods including wind tunnel testing, tow testing, dynamic and static testings. Such methods are presented with more details in the following Chapter 2.4.

2.4 Experimental Research – State of the Art

As stated earlier, the number of quantitative kite experiments is rather limited due to the difficulties in assessing the kite state in real operating conditions. Accurate position and direction of the kite [11] as well as apparent wind speed measurement are such elements relatively difficult to gauge since they depend on external influences. Indeed, weather conditions and environmental solicitation play an important role and have to be taken into account [12]. Furthermore, due to its flexibility, the kite will deform under loading, which consequently changes its behaviour. Nevertheless, some experiments have been conducted by means of different methods. The following Chapters 2.4.1 to 2.4.4 present some of the relevant testing methods that have been performed so far. Chapter 2.4.5 enumerates and describes the parameters with respect to which the aerodynamic curves have been expressed heretofore.

As it might be confusing, the following definitions are clarified. Front lines, which go to the leading edge of the kite, are also referred as power lines. In contrast, the lines which are connected to the tip/trailing edge of the kite are commonly identified as back, steering, control or brake lines since their purposes are to achieve such actions.

2.4.1 Wind Tunnel Testing

Wind tunnel testing is a reliable way to assess the aerodynamic properties of an airfoil [11]. Thanks to the precise control of the flow conditions (speed, pressure, temperature) together with the repeatability of the test, this method allows to provide rigorous and reproducible experimental results. Although wind tunnel testing gives accurate data, several downsides have to be mentioned. Indeed, a wind tunnel is a complex facility composed by several elements which aim at providing constant and steady flow with the least of turbulences. Therefore, the larger the wind tunnel, the more expensive it is to operate it [43]. Consequently, it restrains the size of a kite that can be tested.

A common way to circumvent this is to scale down the investigated object. Doing so will not only reduce the cost of the wind tunnel test campaign but will also limit the amount of energy supplied to the wind tunnel [42]. However, scaling down an aerodynamic body is not an easy task and criteria have to be respected to ensure similar flow between the free flight and the wind tunnel. In order to guarantee the dynamic similitude, similarity parameters, such as Reynolds and Mach numbers, are the key points [37]. They have to be the same for the wind tunnel flow and for the free flight flow. Although it is technically difficult for kites to maintain both numbers simultaneously the same, the effect of Mach number can be neglected for incompressible flow ($Ma < 0.3$) and thus only Re has to be respected [42]. Nevertheless, the geometry scaling raises other challenges. Indeed, it is relatively complex to scale down the light kite structure together with its thin material and to ensure at the same time that the scaled kite reacts and deforms similarly to the real one [43]. At some point, the material, such as wrinkles, fabric and stitches, suffers from technical limitation. Hence, the only way to guarantee similar aerodynamic characteristics along with comparable deformation during wind tunnel test is to investigate full-size kites [10].

De Wachter [42] investigated a 6 m² ram-air inflated kite in the Large Low-speed Facility (LLE) owned by the German-Dutch Wind Tunnels institute in Marknesse (NL). The full-size kite was set upside down in the 8 x 6 m test section as presented in Figure 2.13. Load cells, laser scanning and photogrammetry were used to record the aerodynamic lines loading and the kite shape for different oncoming wind speeds and power setting configurations. The 14 camera photogrammetry setup allowed to reconstruct the shape of the kite and performed CFD simulation whereas the force measurements provided data to establish the aerodynamic curves.

Breukels [10] analysed the canopy deformation of a full-scale inflatable leading edge kite for the purpose of 3D computational model validation. The test took place in the 6.3 m diameter section of the Boëwindkanal at the University of Stuttgart (DE). Same as de Wachter, photogrammetry was also used to determine the shape of the canopy. In addition, the kite was hung upside down with the help of load cells attached on the ceiling of the wind tunnel. Several angles of attack and flow velocities were investigated. Once the computational model was validated, the aerodynamic coefficients along the span were extracted from both 2D and 3D numerical simulations for different angles of attack.



Figure 2.13 De Wachter analysing a 6 m² ram-air kite in the 8 x 6 m wind tunnel test section [42].

2.4.2 Car Tow Testing

An alternative way of testing kites is to use a towing vehicle behind which a full-size kite is attached together with multiple sensors. When performed in light or no wind condition, this solution offers the possibility to control the incoming airflow velocity that the kite experiences by simply adjusting the vehicle driving speed [43]. However, this towing method not only requires a rather long test field in order to have sufficient space to complete the measurements, but a smooth and flat terrain should also be preferred to avoid measurement disturbances due to road bumps. Commonly, the kite is mounted on the test rig thanks to short lines (< 30 m) which ease kite launching and improve flight stability [44]. In addition, an anemometer is set on the moving vehicle to provide wind data. Although this testing method is cheaper than wind tunnel testing, one can already identify some drawbacks of this setup. Indeed, experiments can only be conducted in low wind condition which restricts the number of testing days. Moreover, even if tests are performed in supposedly no wind condition, local winds like gusts always occur and affect the measurements. Furthermore, one important aspect to take care of is the accurate measurement of the tether elevation angle. Indeed, the lift-over-drag ratio is directly estimated from this angle with the help of a tangent relationship. Since the tangent function becomes asymptotic close to 90° and due to the fact that traction kites operate between 75-85°, any small deviation in the elevation angle leads to significant variation in L/D [44]. This issue is even more pronounced with advanced kites which exhibit better performances and therefore greater glide ratio and higher elevation angle. As a result, both wind and angle inaccuracies prove to be the main limitation of this method.

In collaboration with [Peter Lynn Kites](#) developer, Alexander and Stevenson from the University of Canterbury (NZ) designed a car test rig meant for evaluating the performance of both two-line and four-line kites [44], [45]. The main reason for adopting a towing car system was the controllability of the wind speed perceived by the kite. After several designs, they adopted a four light arms test ring bolted directly to the roof of car as illustrated in Figure 2.14. Equipped with potentiometers and load cells (Figure 2.15), the test rig was able to provide both angles and tension measurements of the two or four lines. Moreover, the rig was designed in such a way that the kite could still be steered and controlled from inside the car. To ensure consistency of the rig, tests were only performed with a natural wind speed lower than 15 km/h and a standard kite was tested at the start of every test session. Eventually, six kites from different shapes were investigated on 10 m long lines. The car test rig was performed on a 20 km long sand beach while two parameters were simultaneously varied, namely the wind speed and the back line load. From this, the aerodynamic curves were established. A detailed error analysis of the setup is also provided. Eventually, Alexander and Stevenson acknowledged that the main concern of their car test rig was the accuracy and the repeatability of the results. Indeed, their setup encountered some inherent problems emanating from the tangent relationship which especially leads to high sensibility of the lift-over-drag ratio. Moreover, the weather condition significantly limited the test days and consequently prolonged the time required to acquire a representative set of results.

Dadd [40], [46] from the University of Southampton (GB) compared two analytical kite models against experimental results obtained by towing a 3 m² kite with four 24 m long lines. Static and dynamic flights were performed. The test rig was driven to maintain an apparent wind speed of 15 knots (27.8 km/h) while both line angles and tension were recorded (Figure 2.16). In addition, the wind speed was also logged during measurement. Control of the kite was realized by manually applying equal and opposite forces on the steering lines. From the static measurements, the aerodynamic lift and drag forces were estimated and converted into lift and drag coefficients, which then gave L/D ratio. These performance characteristic values were then used as input for mathematical kite models. Eventually, line tension and 3D trajectories of dynamic figures of eight from the models were compared against experimental results. Dadd also showed that a higher lift-over-drag ratio would lead to a stronger onset speed, which would on the one hand increase the line tension, but on the other hand diminish the stability of the flying kite.

A suitable test setup for the purpose of kite testing has been designed from scratch by Costa from the Swiss Federal Institute of Technology Zurich (CH) [47]. A towing car equipped with an integrated sensor configuration (Figure 2.17) was first used to evaluate the kite aerodynamic properties together with its structural deformation and secondly to record the dynamic flight maneuvers. Indeed, load cells, inclination sensors and wind speed measurement device allowed to assess the aerodynamic coefficients with help of a 2D dynamic point mass model whereas a photogrammetry and image correlation systems computed the kite deformation under loading. In addition, for some tests, an inertial measurement unit (IMU) was fixed on the centre of the kite to provide its orientation. Tests were conducted on the military airfield of Dübendorf (CH) by towing a 15.3 m² inflatable leading edge kite with 12 m long lines. Tests typically lasted about 100 seconds during which launching, measurement and landing occurred. Once the kite had reached its stable position, the power setting was kept constant. During flight, the operator only tried to keep the kite at the zenith position and had to compensate light crosswind by manual steering input. The mathematical kite model was validated by comparing the tether tension against experimental results. Costa found out that the tether drag had a significant influence on the glide ratio. He also tried to relate the deformed kite shape to the tether force. However, performing optical measurement in an outdoor environment led to certain inaccuracies. Moreover, it was not possible to capture the entire kite with two cameras since its curvature was too important.

Hummel from the University of Technology of Berlin (DE) has developed a test bench aiming to accurately test and evaluate tethered wings from the kitesurf industry [48]. The car-trailer setup can either be operated at rest to perform static tests with natural wind or can be driven in no or low wind conditions at a certain speed to simulate a desired wind speed. Depending on the time scale of wind gusts, the whole test bench can potentially reduce their influence by adapting the car speed accordingly. The investigated kite is attached by means of 24 m long four- or five-lines to a trailer mounted with angular and force sensors as illustrated on Figure 2.18. The TETA setup ([Test and Evaluation of Tethered Airfoils](#)) is habitually driven on the former airfield of Pütnitz (DE) which offers 1.5 km of flat concrete road (Figure 2.19). So far, Hummel has tested numerous different kites. Wings up to 21 m² could potentially be investigated whereas the test bench could theoretically withstand a maximum load of 6400 N. When driving the towing test rig at 22 knots (40.7 km/h), assessment of the kite performance is achieved by modifying the kite's power setting from zero power to full power within a short duration, of typically a couple of seconds. Such maneuvers are performed multiple times in order to provide enclosed results. Indeed, the more maneuvers that are recorded, the less important the measurement deviation is. Ideally, up to hundreds of maneuvers are achieved during one single test session leading to angular deviation of 1°. Moreover, the fact of driving back and forth along the airfield allows to limit the effect of possible natural winds. Indeed, assuming a natural wind coming from one side of the airfield, the back and forth runs lessen its effects since the kite experiences a stronger wind speed during one way and a weaker one on the return. Improvements of the test bench are currently in progress to provide relevant information regarding the flying position and deformation of the kite.



Figure 2.14 Car test rig designed by Alexander and Stevenson [44].

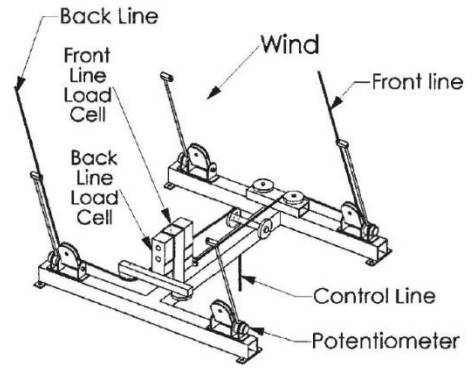


Figure 2.15 Detailed view of the car test rig arrangement [44].



Figure 2.16 Towing test rig designed by Dadd [46].

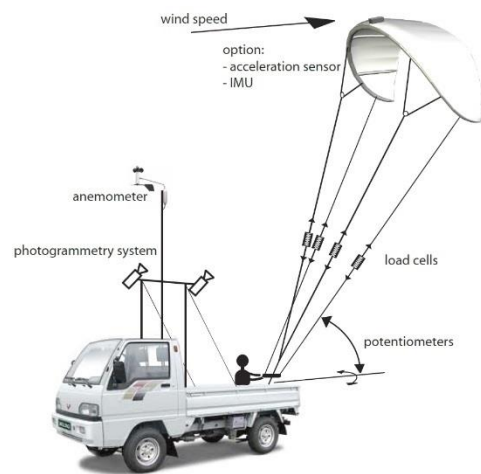


Figure 2.17 Schematic view of the test rig designed by Costa [47].



Figure 2.18 Schematic design of the towing test bench (TETA) developed by Hummel [49].



Figure 2.19 10 m² North Vegas kite towed by the TETA setup. Modified from [50].

2.4.3 Circular Testing

After Alexander and Stevenson from the University of Canterbury (NZ) realised that their previous car-based test rig (Figure 2.14) suffered some intrinsic problems, especially inaccuracies due to the tangent relationship and the low wind requirement, they investigated a faster and more reliable method [44], [51]. A circular test bench was developed which allowed kites to be flown horizontally and to be investigated in a more accurate and repeatable way than with the car-based method. A light motor vehicle was placed in the centre of the test ground and follows a circular path of a determined radius while the kite was pulled by the latter rotating apparatus as illustrated in Figure 2.20. One pilot, sitting backwards, was required to control and stabilize the kite. By knowing three parameters, namely the length of the lines (white dashed line of Figure 2.20), the radius of the circular buggy path (red dashed line of Figure 2.20) and the angle between the two, the lift-over-drag ratio could accurately be determined. Indeed, by adjusting the radius of the vehicle path in such a way that the angle between the lines and the radius approached 90° , the glide ratio became less sensitive to the accuracy of this angle. Moreover, the whole experiment took place indoors in a huge aircraft hangar and therefore, no external contribution of the wind existed, which was one major drawback of the car tow testing method. This significantly improved the repeatability of the experiment. However, since the kite was flying horizontally, the weight did not act in the same plane as the aerodynamic forces anymore. Moreover, due to circular motion, inertia could not be neglected even though its effect might have been small. Although the L/D ratio obtained from this setup differed by definition from the one established by the car towing test, a relationship was established to allow comparison of both test rigs [52]. In addition, it was shown that this method provided significant improvement in accuracy. Indeed, to achieve an accuracy of ± 0.1 for L/D , the precision of the elevation angle measured by the previous car towing test would have to drop below $\pm 0.3^\circ$. On the contrary, the angle measurement with the circular testing method could be less precise ($\pm 5^\circ$) and still led to the same certainty of ± 0.1 for L/D . Furthermore, a wide variety of kites could be investigated in a relatively short term via this test bench since the testing rig could easily be adjusted up to a certain point. However, one limiting aspect was the size of indoor facility. At this time, 15 m long lines could be used to perform experiment in the 40 m wide hangar, but the height of the hangar also limited the size of the kite that had to be investigated.

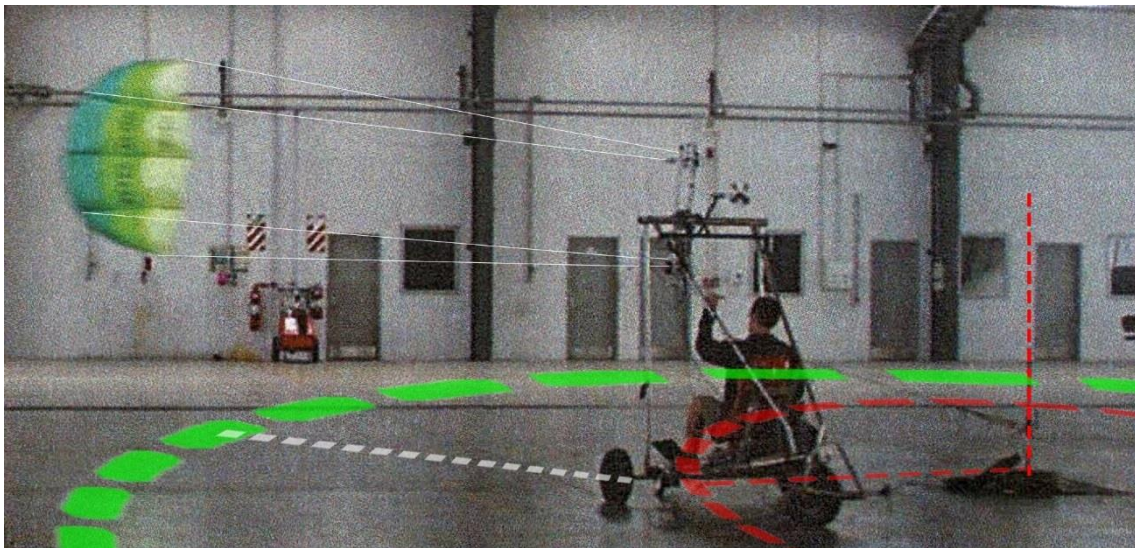


Figure 2.20 Circular test rig designed by Alexander and Stevenson. Green dashed lines: the kite path. White dashed lines: kite lines projection. Red dashed lines: circular vehicle path. Modified from [44].

2.4.4 Crosswind Testing

The aerodynamic properties of a kite can also be determined in normal operating flight conditions of AWE systems, namely crosswind flight. Indeed, by flying so, the kite experiences different wind speeds and develops variable tether forces along the flying path. By accurately recording these two parameters together with the kite position and environmental conditions, relevant information regarding the kite performance can be extracted. Eventually, the actual flying path can be compared to an optimal path obtained numerically. This testing method allows to investigate very large kites which could not be evaluated with other test benches. Kites of 500 m² are evoked [43]. Moreover, no extra energy is required to operate the test bench besides the natural wind energy and the steering input. Even in light winds, the kite is able to reach high velocities by flying crosswind. Consequently, this extends the number of testing days available. However, one limitation of this setup is a strong windy day during which the kite could potentially be damaged by experiencing overloading. A second drawback is the difficulty in obtaining accurate wind speed measurement at the kite, which is then used to establish the aerodynamic kite properties. Inaccuracies of the global system can be limited by averaging multiple figures of height over an extended period of time. Nevertheless, since this testing method depends on the environmental conditions, a steady and constant wind should be preferred to obtain reliable results.

In his work of analysing the contribution of each element constituting a speed kiteboarder, van der Vlugt, from University of Technology of Delft (NL), especially focused on establishing the aerodynamic properties of a 6 m² kite [43]. He restricted the crosswind flight motion into a horizontal plane by flying the kite from one side of the wind window to another as illustrated in Figure 2.21. While performing such horizontal flights, the velocity of the kite, the tension within the lines and the wind velocity were simultaneously recorded by means of appropriate sensors. Indeed, GPS, load cells and anemometer have been selected accordingly. Tests were performed on Scheveningen Beach (NL) which offers large open area together with undisturbed wind. Since crosswind flight leads to large forces, especially when the kite flies through the power zone of the wind window, a solid anchor was required to dissipate this energy and to handle the system. Heavy sand bags were used for this purpose. In addition, lines of 50 m were selected in order to allow the kite to accelerate to its top speed and to still be easily controlled. Eventually, roughly 80 sweeps were performed from which the glide ratio was extracted. By knowing the line tension, both lift and drag coefficients could be established. Important is to note that L/D ratio, and therefore C_L and C_D , were determined by only using peak velocity and peak load of each sweep. Consequently, a lot of data remained unused. Attempts in establishing the glide ratio along the entire path have been done. However, the accuracy of the apparent wind speed was not sufficient to provide relevant data. Van der Vlugt recommended to install an anemometer directly on the kite in order to obtain accurate apparent wind measurement.

Fagiano from Politecnico di Torino (IT) aimed to demonstrate the strong potential of innovative AWE technology in the revolution of wind energy. His work significantly contributed to push the AWE technology one step further. Indeed, he dedicated his PhD thesis [53] on the development and the automatic control of AWE systems. A small-scale pumping system, commonly referred as HE-yoyo and presented in Figure 2.23, were designed in order to validate the concept of high altitude wind energy system. The prototype was able to operate with airfoils ranging from 8 to 18 m² of projected area and was connected with 1 km long cables made of composite fibres. These 4 mm diameter tethers could withstand 1.3 ton of loading each. Two independent drums, around which the two tethers were wound, could operate separately as a motor or generator to achieve necessary steering. On-board sensors allowed to track the motion of the kite in the sky. At ground level, measurement devices provided data regarding tether force, speed, power output, magnitude and direction of wind speed. Although he did not extract the aerodynamic curves from data, he used the measurement to compare the generated power, the line length and the line speed from the experiment against the simulated one in order to estimate the degree of confidence of the model. Eventually, he found good correspondence between simulation and experimental results, which indicated confidence in developing medium-to-large scale generators.

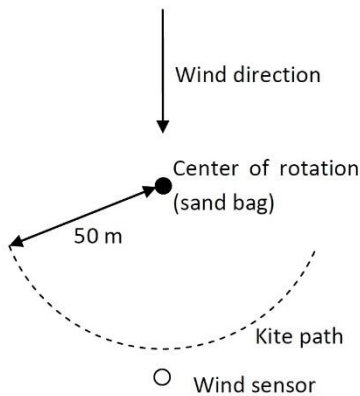


Figure 2.21 Schematic top view of the testing method employed by van der Vlugt [43].

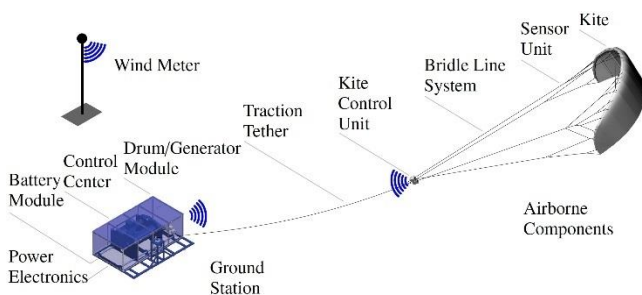


Figure 2.22 TU Delft prototype used by Ruppert [54].



Figure 2.23 Test bench of Politecnico di Torino used by Fagiano. Modified from [53].

Recently, Ruppert from University of Technology of Delft (NL) developed a real time pumping kite power model and validated it with experiment [11]. Since his numerical model required the aerodynamic coefficients as input, these had firstly to be established by means of experimental measurement. For this, Ruppert analysed the data obtained by flying figures of eight with a 25m^2 kite connected to the 20 kW ground station designed by TU Delft (NL) and schematized in Figure 2.22. Besides usual sensors composed of GPS, force sensors and ground-based anemometer, Ruppert developed an apparent wind measurement system relying on a Pitot tube which pointed towards the flow thanks to a shuttlecock. The airborne anemometer was mounted in between the kite bridles. Nevertheless, this device was not available for many flight tests. In addition, an IMU was attached directly on the kite and provided the orientation of the kite along the flying path. By knowing this information, Ruppert attempted to express the aerodynamic curves with respect to the angle of attack. Since the angle delivered by the IMU depends on the IMU mounting, the angle of attack was not refereeing to the kite geometry but rather to the IMU placement. Although an offset existed between the measured angle of attack and the real one, the general trend could be extracted and used to express the aerodynamic curves in function of it. Eventually, Ruppert declared that a wind speed measurement device at the kite is essential in obtaining accurate kite characteristics. Moreover, he showed that the quality of the results depends on the accuracy of the GPS and IMU.

2.4.5 Aerodynamic Curves with respect to ...

As found in the literature, the aerodynamic curves can be expressed with respect to different parameters. This chapter aims at listing these diverse parameters and at describing their origin as well as their advantage/disadvantage. Important is that the following list might not be exhaustive since other parameters could have been adopted in other studies.

2.4.5.1 Angle of Attack

From an aerodynamic point of view, pressure and shear stress distributions are the only two sources which lead to a resultant aerodynamic force \mathbf{F}_a experienced by a given airfoil moving throughout a fluid [37]. The resultant aerodynamic force can then be decomposed into two forces, namely the axial force \mathbf{A} formed by the component of \mathbf{F}_a parallel to the chord and the normal force \mathbf{N} which is the component of \mathbf{F}_a normal to the chord. Alternatively, the resultant aerodynamic force can also be decomposed with respect to the apparent velocity vector \mathbf{V}_a which leads to a lift force \mathbf{L} perpendicular to \mathbf{V}_a , and to a drag force \mathbf{D} , parallel to \mathbf{V}_a . Consequently, these two decompositions are directly related by the following Equation (2.8) and Equation (2.9).

$$L = N \cos \alpha - A \sin \alpha \quad (2.8)$$

$$D = N \sin \alpha + A \cos \alpha \quad (2.9)$$

where α is the angle between the chord and the apparent wind speed defined as the angle of attack (AoA). Dividing these forces by the dynamic pressure and a reference area, the corresponding non-dimensional coefficients are obtained: axial force coefficient C_A and normal force coefficient C_N alternatively lift coefficient C_L and drag coefficient C_D . Such coefficients are widely used to characterize the aerodynamic properties of a given body. Given Equation (2.8) and Equation (2.9), one can already notice the dependence of these aerodynamic coefficients on the angle of attack. J. Anderson [37] generalises the definition of these aerodynamic coefficients by including Re and Ma numbers. Thus, both lift and drag coefficients are function of Reynolds number, Mach number and the angle of attack as expressed by Equation (2.10) and Equation (2.11).

$$C_L = f_{C_L}(Re, Ma, \alpha) \quad (2.10)$$

$$C_D = f_{C_D}(Re, Ma, \alpha) \quad (2.11)$$

Although both Re and Ma numbers might significantly vary for the case of aircraft, the aerodynamic curves are usually expressed versus the angle of attack. In the case of pumping kite power system however, both Reynolds and Mach numbers can be considered as constant since the apparent velocity, namely the only variable parameter, does not change its order of magnitude. Therefore, both lift and drag coefficients only depend on the AoA. Consequently, one might want to relate the aerodynamic coefficients to the corresponding angle of attack when characterising the aerodynamic properties of a kite.

By towing the kite with his vehicle, Costa [47] was able to express the aerodynamic coefficients with respect to the angle of attack of the kite. Indeed, thanks to his setup, he established two different methods to obtain the AoA. One approach was to directly measure the orientation of the kite by means of an IMU placed on the kite. Thus, the acceleration sensor provided the angle between the kite chord and the horizontal plane, namely the pitch angle ψ . By determining the wind direction angle γ , the angle of attack, as illustrated on Figure 2.24, could be derived from Equation (2.12).

$$\alpha = \psi + \gamma \quad (2.12)$$

The second approach stemmed from the assumption that the kite lines are ideally fixed as soon as the kite has reached its equilibrium position. Thus, an angle relationship could be established to obtain the pitch angle ψ . By looking at Figure 2.24, the following Equation (2.13) could be considered. It relates the pitch angle to the tether elevation angle θ_c and to an offset angle η which acts as a fitting parameter. Indeed, η represents the deviation angle from which the kite lines and the chord deviate from right angle. For his case, Costa [47] established that the offset angle η varies between -5° and -10° depending on the position of the power line with respect to the steering lines. In other words, a fully powered kite will have shorter steering lines which then diminish the offset angle η which consequently leads to a greater angle of attack.

$$\psi = \left(\frac{\pi}{2} - \theta_c\right) - \eta \quad (2.13)$$

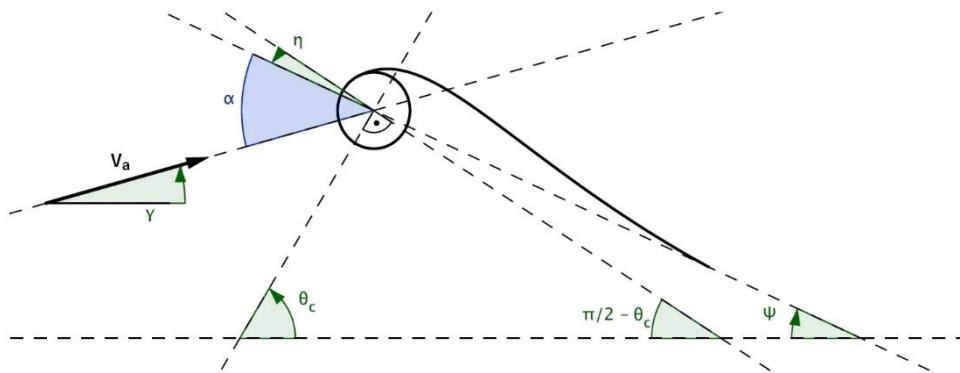


Figure 2.24 Angles representation as defined by Costa. Modified from [47].

Initially, Costa plotted the lift coefficient versus the tether elevation angle θ_c . This led to a rather dispersed data plot. However, by expressing the aerodynamic coefficient with respect to the angle of attack, it reasonably gathered the different measurements of C_L and a general trend could be identified as presented in Figure 2.26. Nevertheless, before fitting polynomial curves to the scattered data, a filter was applied to only consider data for which the kite was flying downwind with a range of $\Delta\phi_c = \pm 15^\circ$. This value was chosen to gauge the deviation from the 2D model assumed. From then, a linear curve was fitted for the lift coefficient whereas a second order curve was assumed for the drag coefficient. Although this should not be the case, Costa showed that the aerodynamic curves were affected by the change in wind speed. He suggested that at faster wind speeds, the kite experienced higher loads which in turn led to greater deformations and consequently modified the aerodynamic performance. Moreover, Costa advised to add supplementary sensors in order to obtain a better accuracy of both AoA and apparent wind speed. Indeed, these two parameters had a strong influence on the final results. Eventually, a 3D mathematical model would be required to improve the data evaluation. Nevertheless, the highest glide ratio obtained for low angles of attack varied between 4.5 and 5.5.

A general remark on the angle of attack concerns the placement of the IMU sensor. Indeed, care should be taken when mounting the device on the kite. Depending on the location of the sensor, an offset angle might appear with respect to the true pitch angle. For instance, the IMU can easily be attached to a strut tube which is not necessary aligned to the chord as illustrated in Figure 2.25. This is not a problem as long as this offset angle is known. The angle provided by the IMU can then be corrected accordingly.

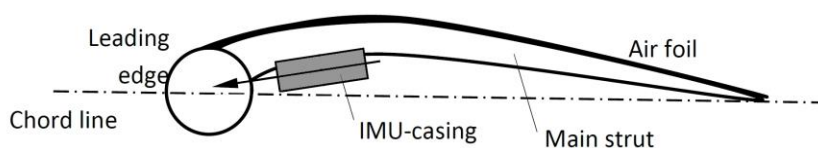


Figure 2.25 Mounting of an IMU and its orientation with respect to the chord line. Modified from [11].

Ruppert also estimated the angle of attack of the wing by means of an IMU attached directly on the kite [11]. The acceleration sensor provided the orientation of the kite, namely the pitch angle ψ . However, unlike Costa, whom apparent wind velocity could be considered as stable once the kite had reached its equilibrium position, Ruppert investigated the aerodynamic performance by flying the kite in a crosswind manner. Hence, the wind speed perceived by the kite was constantly changing along the flying path. Thus, Equation (2.12) became more delicate to apply since the measurement of the apparent wind direction was one of the most complex variables to assess. Nevertheless, he used Equation (2.5) to evaluate the apparent wind speed which was then compared to the speed measured by the Pitot tube. The apparent wind direction V_a is composed by the natural wind velocity vector V_w which was assumed to be parallel to the ground and by the kite velocity V_k which was derived from GPS position. The magnitude of the natural wind speed was extrapolated from a wind shear model which took into account the surface roughness of the testing area. At this point, two sources of error were identifiable, namely the accuracy of the wind shear model and the precision of the GPS tracking. His results are therefore more an approximation than the exact value. Secondly, the GPS sensor did not provide reliable data. The accuracy of the GPS significantly dropped when the kite was performing highly dynamic maneuvers. The signal was even lost when accelerations exceeded 4G. Nevertheless, Ruppert attempted to relate the aerodynamic properties with respect to the estimated angle of attack. Figure 2.27 illustrates the glide ratio for the 25 m² kite flying figures of eight. Although the measurement points are rather spread out, a weighted linear least squares method is used to smooth the data and to extract the general trend. Ruppert mentioned that the weight and inertia effect of the pod together with the tether sag might not only have significant effect on the aerodynamic values but might also influence the measurement of the angle of attack. In addition, the inaccuracy of the wind shear model and the GPS data could also explain this scattered point cloud. Eventually, Ruppert acknowledged that the wind speed (both magnitude and direction) at the kite was one of the most critical parameters to measure. A more advanced on-board anemometer might improve the measurement.

Relating the aerodynamic curves to the angle of attack allows the comparison of different wings, not only within the aircraft industry but also from the traction kite point of view. The angle of attack is one simple generic parameter which does not depend on the size nor on the weight of the wing. However, defining an angle of attack for a kite is not an easy task since the wing is not rigid and might deform during flight. One can define the angle of attack with respect to the mid-span chord line [43]. Nevertheless, steering input may also have an influence on this angle of attack, even in downwind position.

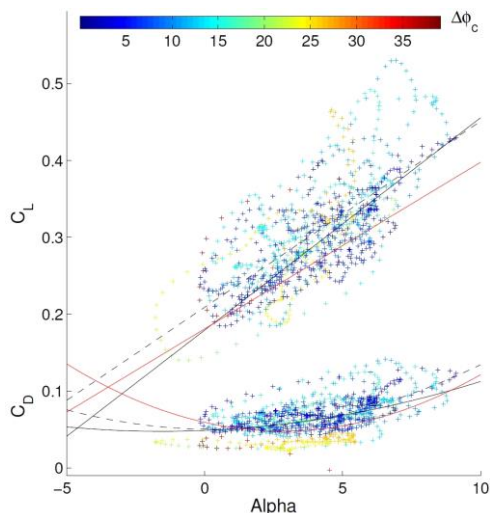


Figure 2.26 Aerodynamic coefficients achieved by Costa [47]. $\Delta\phi_c$ indicates the azimuth downwind deviation. Red: curve fitted for $V_a = 14$ m/s. Black: curve fitted for $V_a = 16$ m/s. Dashed: curve fitted on scattered data.

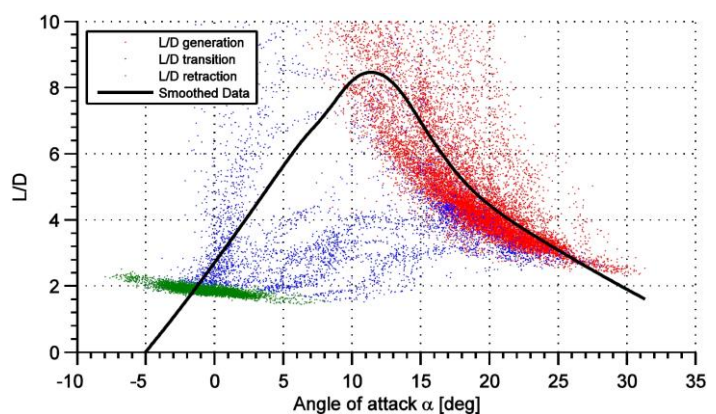


Figure 2.27 Glide ratio obtained by Ruppert [11] during generation (red), transition (blue) and retraction (green). Black: weighted linear least squares fitting curve.

2.4.5.2 Back Line Force Ratio

An alternative way of representing the aerodynamic curves is to refer them to the back line force ratio ($BL\%$), as mentioned for the first time by Stevenson [44]. This ratio, given by Equation (2.14), relates the back line load to the total tether force. Although Stevenson declared that the $BL\%$ had the greatest influence on the kite performance, he pointed out the fact that modifying the back line length would in turn alter the angle of attack of the wing. Nevertheless, he claimed that the change in back line load was the only way for a flyer to adjust these aerodynamic performances. Hence, Stevenson considered the back line ratio as a major and useful parameter to represent the kite aerodynamic properties. Figure 2.28 shows the lift-over-drag ratio of a 3.2 m^2 kite with respect to the back line force ratio for six different days. It can be observed that glide ratio values lay between 4 and 5 for the given kite. Stevenson noted one main issue of the method when the tension of the back lines was very low. The tension would not be sufficient enough to straighten the line and therefore a significant curvature would appear leading to inaccuracies.

$$BL\% = \frac{T_{back}}{T_{total}} \quad (2.14)$$

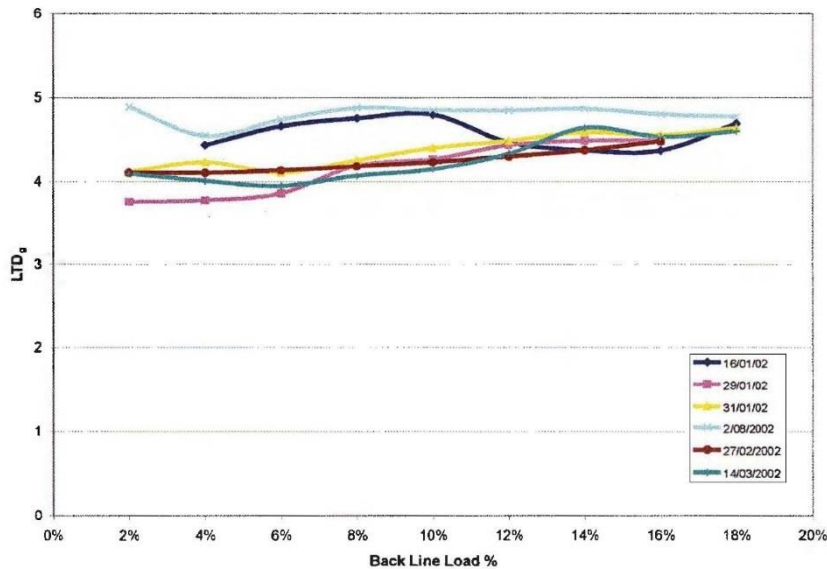


Figure 2.28 L/D vs $BL\%$ for a 3.2 m^2 kite for different testing days established by Stevenson. Modified from [44].

Although van der Vlugt supported Stevenson's idea, he pointed out that the $BL\%$ parameter should be cautiously handled [43]. Within his thesis, he showed that the angle of attack might not necessarily be coupled to the back line ratio. Indeed, a same $BL\%$ could be obtained by two distinct angles of attack if the two different lift and drag force repartitions have collinear resultant forces. This particular situation is illustrated in Figure 2.29. Nevertheless, in general the angle of attack evolves as the back line ratio increases. Therefore, this $BL\%$ ratio is expected to have significant control over the kite performances. Results obtained by van der Vlugt for the glide ratio are presented with respect to the back line ratio in Figure 2.30.

As a general comment, one can expect that the weight of both wing and lines would have an influence on the load cell reading located at the bottom of the line. Indeed, the measured force in the back line is basically composed by the aerodynamic lift and drag forces but also by the weight and inertia of the material involved, namely the kite and lines. Although this contribution might be relatively small compared to the resultant aerodynamic force, this could lead to some miscalculations and should be kept in mind.

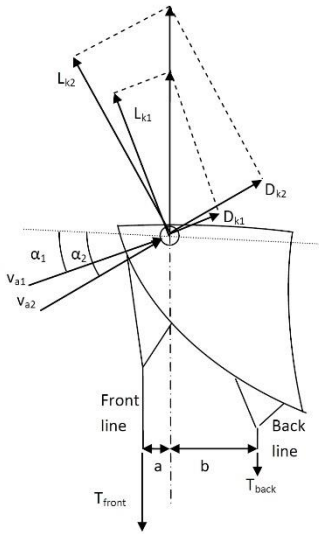


Figure 2.29 Two distinct α stemming from the same $BL\%$ [43].

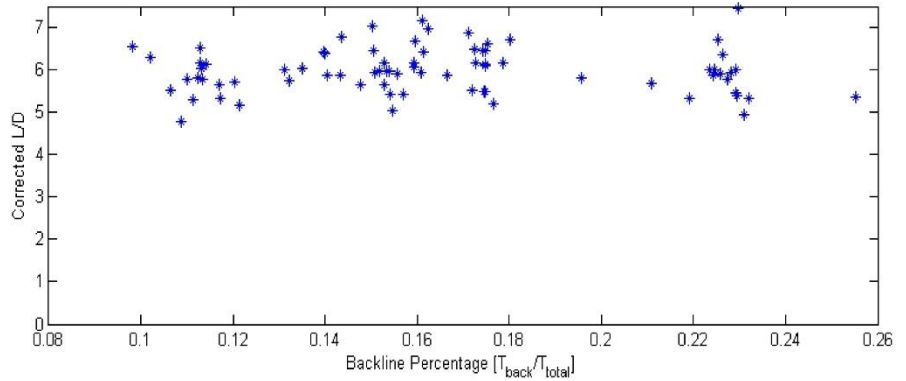


Figure 2.30 L/D vs $BL\%$ for a 6 m^2 kite investigated by van der Vlugt. Modified from [43].

2.4.5.3 Brake Position

De Wachter mentioned that unlike aircrafts, kites do not have a single well defined angle of attack. Therefore, an alternative parameter should be considered. In his work on ram-air kites [42], he explains that the behaviour of the kite results from its L/D ratio which itself is a distribution of the airfoil loading. This force distribution derives from both dynamic pressure and brake setting. As the back lines are varied, the pitch angle of the kite and consequently the AoA are modified which in turn alters both lift and drag forces and therefore the glide ratio as well. Hence, de Wachter considered the brake line position as the major characteristic parameter to relate the aerodynamic properties of the kite. A pull on the brake lines, considered as positive, increased the angle of attack and consequently the lift force whereas the opposite occurred when a release of the back lines was applied. Figure 2.31 presents the glide ratio obtained thanks to the wind tunnel measurement performed by de Wachter.

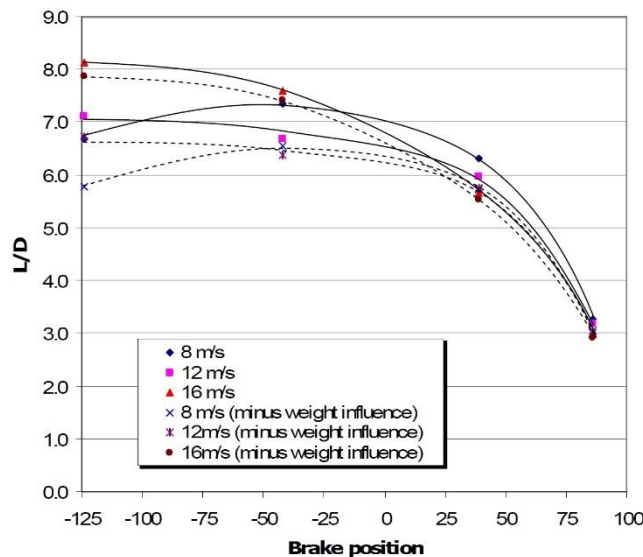


Figure 2.31 Glide ratio for different wind speed expressed versus the brake position from de Wachter. Modified from [42].

However, one comment on this method should be mentioned. Unlike other characteristic parameters, the brake line position is not a non-dimensional parameter and depends moreover on the kind of lines employed for testing. If different lines were selected, the general behaviour might have been slightly modified compared to the previous one. A more universal characteristic parameter should be preferred for comparing kite performances.

2.4.5.4 Power Ratio

In line with the reasoning of de Wachter, Hummel suggested to relate the aerodynamic efficiency curves to the power ratio [48] for the purpose of comparing wings from sports kites. Since a non-dimensional ratio is considered, this method is suitable for comparing different wing concepts. The power ratio $PR\%$, as defined in Equation (2.15), relates the variation in length between the front and the back lines. Precisely, it compares the current position of the handle bar with respect to its position corresponding to a fully powered kite. Therefore, a value of 100% means that the kite is fully powered (i.e. handle bar close to the pilot), whereas a value of 0% corresponds to a completely depowered kite (i.e. handle bar away from the pilot). The distance encompassed between 0 and 100% is defined as the so-called power range. It is important to note that in the case of full power, the length of both front and back lines are equal.

$$PR\% = \frac{\text{power position}}{\text{total power range}} \quad (2.15)$$

Since Hummel always used the same line system and consequently the same power range, he was able to compare multiple kites of different shapes against each other. On the test bench, the power ratio was controlled automatically which allowed reproducible dynamic maneuvers. Figure 2.32 shows the lift-over-drag ratio versus the power ratio for several sports kites evaluated during different test sessions. As a general trend, it can be seen that, as the kite is powered, it gains altitude which translates into an increase of the tether elevation angle, eventually leading to a higher glide ratio.

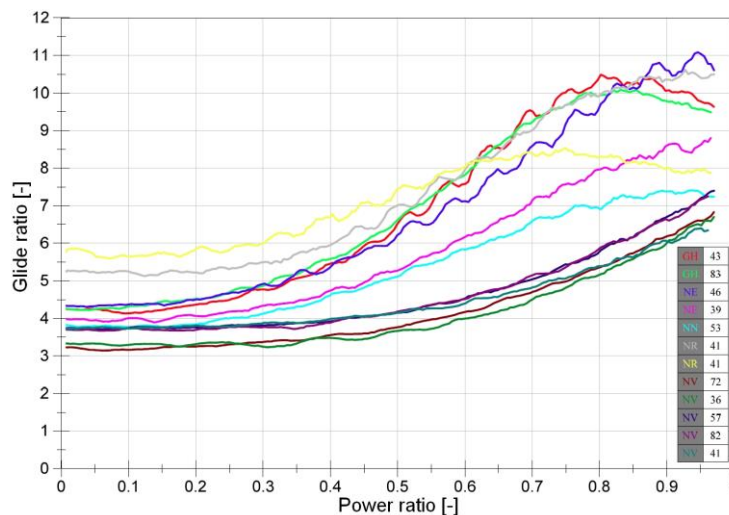


Figure 2.32 Glide ratio for different kites assessed by Hummel. Modified from [48].
First column: abbreviation of the kite name. Second column: number of maneuvers performed.

During several months of investigation, different kites were flown with the same line system. In every test, a large power range of 500 mm was used to adjust the power setting of a given kite. It is important to note that in the kitesurf industry, the kite including bridles and lines together with the bar are usually considered as two separate objects. Bars and lines can be exchanged from one kite to another. Furthermore, a kite wing has its own intrinsic power range which does not necessarily correspond to the same range covered when using a given bar-line system. As a consequence for the TETA test bench, kites with a larger power range than the one provided by the line system could not be fully investigated. Only a fraction of their power range could be covered. Nevertheless, this situation hardly occurred since the 500 mm power range employed by the TETA test rig was wider than most common power ranges. If this range was still not sufficient enough, the line system could easily be extended to include the kite power range. Conversely, kites with shorter power range than the line system could easily be fitted and be tested throughout their full power range.

2.5 Background Theory and Theoretical Models

2.5.1 Wind Models

Analogously to fluid mechanics where a flow is slowed down as it approaches a wall, natural wind within the earth boundary layer generally decelerates as it comes closer to the ground level. Although the magnitude of the wind speed varies in time and space, its average value generally increases with elevation above ground. This phenomenon is known as wind shear [55]. As previously mentioned in Chapter 2.1.1, two wind profile models are commonly adopted to consider wind speed near the earth's surface, namely the Log Law and Power Law. These wind models are given in Equation (2.16) and Equation (2.17) respectively. It should be kept in mind that both relationships may not be used above 500 m [15]. In addition to that, the variation in wind direction can usually be considered as negligible in the first 100 m [56].

$$\text{Log Law} \quad V_w(z) = V_w(z_{ref}) \frac{\log\left(\frac{z}{z_0}\right)}{\log\left(\frac{z_{ref}}{z_0}\right)} \quad (2.16)$$

$$\text{Power Law} \quad V_w(z) = V_w(z_{ref}) \left(\frac{z}{z_{ref}}\right)^\alpha \quad (2.17)$$

The Log Law is based on both theoretical and experimental research regarding boundary layer flow at atmospheric level. The natural wind speed V_w at a given height z is extrapolated from the wind speed measured at a reference height z_{ref} by taking into account the surface roughness length z_0 of the location. The latter is the main parameter and depends on the terrain characteristic as presented in Table 2.1. The Power Law is a simple model to estimate the vertical wind profile. It also considers the quality of the terrain through a parameter, namely the Power Law exponent α . Typical values for α are illustrated in Table 2.2. The Power Law generally approximates wind profiles well empirically [15]. It should be mentioned that the zero value, namely $V_w = 0$ m/s, is defined for the Log Law at z_0 , whereas for the Power Law, the wind profile is zero at the surface of the ground.

Table 2.1 Roughness length for Log Law [15]

Terrain characteristics	Roughness length z_0 (m)
Water surface	0.0002
Open areas with a few windbreaks	0.03
Farm land with some windbreaks more than 1 km apart	0.1
Urban districts and farm land with many windbreaks	0.4
Dense urban or forest	1.6

Table 2.2 Power Law exponent [15]

Terrain characteristics	Exponent α [-]
Smooth hard ground, calm water	0.10
Tall grass on level ground	0.15
High crops, hedges and shrubs	0.20
Wooded countryside, many trees	0.25
Small town with trees and shrubs	0.30

2.5.2 Wing Aerodynamic

As air passes over an airfoil, it generates a resultant aerodynamic force F_a which can be decomposed into both lift L and drag D forces as presented in Equation (2.18). Its magnitude is given in Equation (2.19). The lift force L is defined normal to the apparent wind speed V_a whereas the drag force D is parallel to it. The magnitude of these vectors is given in Equation (2.20) and Equation (2.21) respectively. Both aerodynamic forces depend on the square of the ap-

parent wind speed V_a , which is by definition the relative velocity of the wing. The vector of the apparent wind speed V_a , previously mentioned in Chapter 2.3.3, is presented again for convenience in Equation (2.22). It combines both natural wind speed V_w and kite velocity V_k .

$$\mathbf{F}_a = \mathbf{L} + \mathbf{D} \quad (2.18)$$

$$F_a = \frac{1}{2} \rho_{air} A_{ref} C_R V_a^2 \quad (2.19)$$

$$L = \frac{1}{2} \rho_{air} A_{ref} C_L V_a^2 \quad (2.20)$$

$$D = \frac{1}{2} \rho_{air} A_{ref} C_D V_a^2 \quad (2.21)$$

$$\mathbf{V}_a = \mathbf{V}_w - \mathbf{V}_k \quad (2.22)$$

The aerodynamic coefficients C_R , C_L and C_D are obtained by dividing Equation (2.19), Equation (2.20) and Equation (2.21) respectively by the dynamic pressure q_∞ given in Equation (2.23) [37]. Thus, Equation (2.24), Equation (2.25) and Equation (2.26) respectively are derived. In addition, the three aerodynamic coefficients are related, similarly as Equation (2.18), through Equation (2.27).

$$q_\infty = \frac{1}{2} \rho_{air} V_a^2 \quad (2.23)$$

$$C_R = \frac{F_a}{q_\infty A_{ref}} \quad (2.24)$$

$$C_L = \frac{L}{q_\infty A_{ref}} \quad (2.25)$$

$$C_D = \frac{D}{q_\infty A_{ref}} \quad (2.26)$$

$$C_R = \sqrt{C_L^2 + C_D^2} \quad (2.27)$$

It is important to note that the above equations consider a reference area A_{ref} . This reference area has to be related to the geometrical body shape. For an aircraft wing, the planform area is usually taken as reference. However, for a kite wing, which by nature is flexible, no general rules have been established yet. One can decide to consider either the flat wing area (Figure 2.33) or alternatively the projected wing area A_{proj} (Figure 2.34). For instance, New Zealand based kitesurf company, [SwitchKite](#), indicates both areas in their kite specification [57]. Other definition could be imagined, such as the projected wing area in the direction of the lift vector [58]. Nonetheless, the choice of the reference area is not a critical factor as long as it is known which reference area the measurements are based on [37].



Figure 2.33 Flat wing area.
Modified from [57].

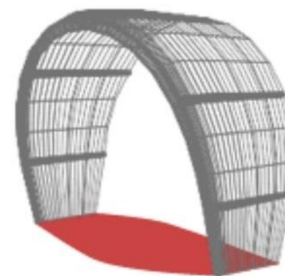


Figure 2.34 Projected wing area A_{proj} .
Modified from [57].

Eventually, the kite glide ratio G is defined by Equation (2.28). As it is presented in Chapter 2.5.4, other glide ratios can be defined including for instance the tether which leads to extra drag. This is then considered as the effective glide ratio of the whole airborne system combining wing and tether [35].

$$G = \frac{L}{D_k} = \frac{C_L}{C_D} \quad (2.28)$$

2.5.3 Kite Model

In the last years, several models of different levels of complexity have been developed to analyse the kite and its behaviour. Figure 2.35 shows some of these models. They differ not only in degrees of freedom but also in level of assumptions. Moreover, the consideration of deformations also evolves with the complexity of the model. For instance, it is obvious that a point mass model does not take the deformation of the wing into account whereas a complex finite element model captures such changes in shape. An exhaustive list of kite models implemented in the past is available in the work of Ruppert [11]. He also explained that many kite models originate from the simple point mass model developed by Diehl [59]. Although the purpose of these models is to achieve a computational simulation of the kite, the point mass model can be used for an analytical investigation of the kite properties. Indeed, Costa [47] implemented a 2D dynamic point mass model to evaluate his measurement data. Dadd [40] also used the point mass model to investigate the effect of mass by comparing it to a zero mass model.

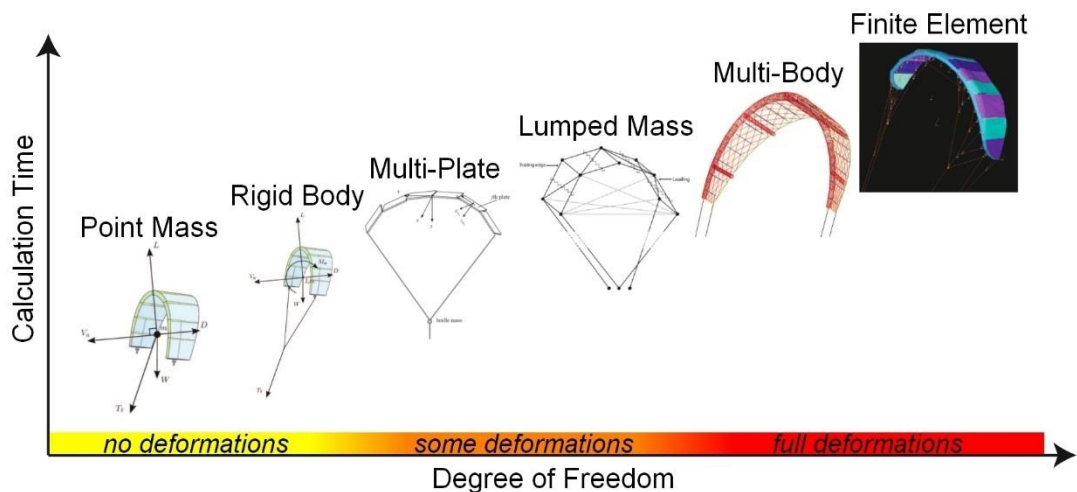


Figure 2.35 Kite models with different levels of complexity. Modified from [48].

2.5.4 Tether Models

In order to simulate the entire kite power system, the tether has to be considered as well. Indeed, there is no doubt that the cables have an influence on the kite behaviour. Depending on the length of the tether, its weight plays a more or less important role in the dynamic of the kite. Moreover, when flying the kite crosswind, the tether also experiences a fast apparent wind speed which results in a drag force distributed along itself. Consequently, both weight and drag forces have an effect on the tether shape. In addition, the tether might sag depending on the magnitude of the forces involved in the lines (Figure 2.36). Eventually, due to its material properties, the cables might elongate under the experienced tension. Several models have been developed accordingly. Ruppert [11] provides a quick overview of the existing models. Most common analytical considerations are presented in the following section.

The simplest model considers the tether to be straight without mass nor drag. Therefore, the tether has no effect on the kite. It simply links the kite to the ground by a given length. To improve this model, Houska [38], [60], Argatov [35], [61] and Fagiano [53] modelled the tether drag in their calculation. By assuming the apparent wind experienced by the tether to increase linearly along it, the angular momentum generated by the distributed drag force along the cable is integrated. Knowing this momentum allows to determine an equivalent tether drag force acting on the kite. The situa-

tion is illustrated in Figure 2.37. In such a way, a point mass model for the kite can still be employed. The equivalent aerodynamic drag of the tether is given in Equation (2.29). However, it should be mentioned that the calculation assumes crosswind flight. This means that a faster velocity is experienced by the tether close to the kite than near the ground. This might not necessarily be the case if the kite stays at zenith. By lumping the tether drag to the kite, the effective glide ratio of the kite and the tether together can be established via Equation (2.30).



Figure 2.36 Tether sag [11].

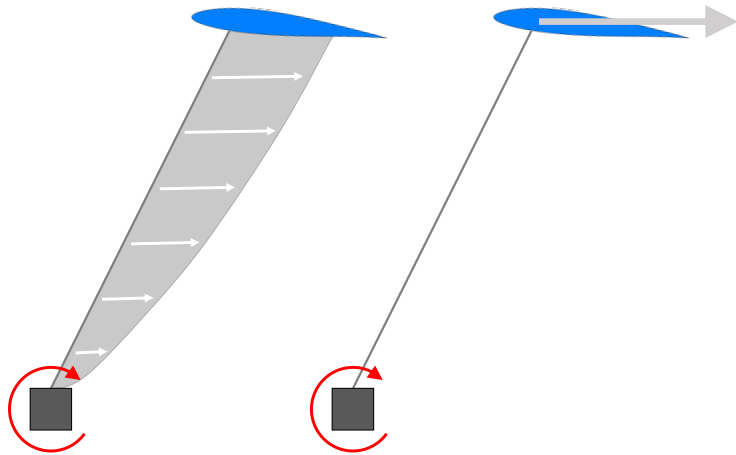


Figure 2.37 Schematic representation of the distributed drag equivalent to drag lumped to the kite.

$$D_t = \frac{1}{8} C_{D,t} \rho_{air} d_t l_t V_a^2 \quad (2.29)$$

$$G_e = \frac{C_L}{C_D + C_{D,t} \frac{d_t l_t}{4 A_{ref}}} \quad (2.30)$$

It is worth mentioning that some considerations differ from one author to another. Fagiano [53], for instance, considered the line surface perpendicular to the apparent wind speed rather than the total front line area as expressed in Equation (2.29). Argatov [35], [61], on the other hand, took into account not only the normal tether drag coefficient but also the frictional one. Although the second term is generally negligible compared to the normal tether drag coefficient, Argatov calculated that omitting it would lead to an error of 2%.

Since the weight of the tether might represent a large part of the total weight of the AWE system, it has to be included in the models. Fagiano [53], Argatov [61] and Rautakorpi [62] considered that half of the weight of the tether acts on the kite and half of it is supported by the ground station, independent from the elevation angle. On the other hand, van der Vlugt [54] and Noom [58] lumped the tether weight to kite in a similar way as it has previously been done with the tether drag. Figure 2.38 illustrates their reasoning. They decomposed the tether weight into two parts, namely one aligned with the tether and one transverse to it. Considering that the tether can only support tension forces, the component along the tether is only supported by the kite. In addition, transverse force component has to be equally distributed at each ends of the tether. Therefore, the equivalent tether gravity force $\mathbf{F}_{g,t}$ acting on the kite is depicted in spherical coordinates (r, θ, φ) in Equation (2.31).

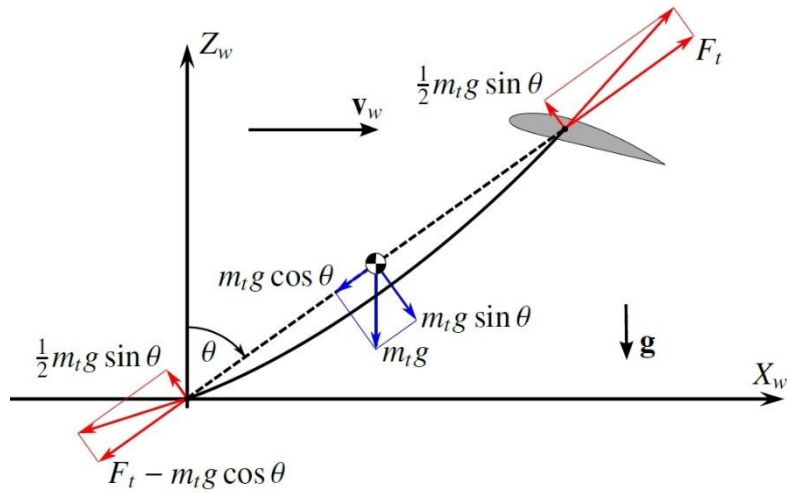


Figure 2.38 Free body diagram used by van der Vlugt to consider the tether weight [54].

$$\mathbf{F}_{g,t} = \frac{1}{4} \rho_t \pi d_t^2 l_t g \begin{pmatrix} -\cos \theta \\ \frac{1}{2} \sin \theta \\ 0 \end{pmatrix} \quad (2.31)$$

Eventually, the sag of the tether induced by its weight, drag and lift has to be considered. Noom [58] showed that when a single uniform distributed load is applied, an analytical solution can be found by using the catenary equation developed in 1691 by Huygens, Leibniz and Bernoulli. He formulated the catenary equation, as shown in Equation (2.32), by considering the distributed gravitational force along the tether. The tether loading constant c_t is defined in Equation (2.33). The two constant C_1 and C_2 are defined from the boundary conditions $z(0) = 0$ and $z(x_k) = z_k$ respectively, where x_k and z_k are the kite position in (x, y, z) reference.

$$z = \frac{l_t}{c_t} \cosh\left(\frac{c_t}{l_t} x + C_1\right) + C_2 \quad (2.32)$$

$$c_t = \frac{\frac{1}{4} \rho_t \pi d_t^2 l_t g}{F_{t,x}} \quad (2.33)$$

Varma [63] argued that the catenary equation taking into account only the weight cannot faithfully represent the shape of the tether. Therefore, he included not only weight but also drag and lift of the tether in his calculation. It is worth mentioning that Varma neglected the variation in wind speed with altitude. Argatov [35], [61] also considered these forces acting on the tether and established equations for a gently sloping static line profile.

3 Thesis Goal and Approach

3.1 Objective

The main objective of this present M.Sc. Thesis is:

**“to improve the assessment methodology and exactitude of
the aerodynamic properties of the Kitepower wing
for the purpose of computational model validation”**

As stated in Chapter 2.4, only a few numerical models have been validated experimentally. However, in order to estimate their accuracy, computational models have to be validated against measurement data. The lack of experimental data regarding kites is often an issue at the current state of research. In addition, the aerodynamic properties are typically used as a basis to compare kites against each other. Therefore, experimental data are of great interest not only for the purpose of numerical model validation but also for kite comparison. This main objective is divided into four research questions, namely:

- **Which car tow testing procedure is the most appropriate for evaluating the kite aerodynamic performances ?**
- **Do kite mass, tether mass, drag and lift have significant effects on the kite glide ratio or can they be neglected ?**
- **Is the straight tether assumption valid or should the sag of the tether be considered for such testing conditions ?**
- **Is it possible to express the aerodynamic curves with respect to the angle of attack in a reliable manner ?**

3.2 Approach

With the aim of extracting the aerodynamic performance parameters of the kite from measurement, an analytical point model of the kite with different levels of refinement is implemented in this work. In addition, a quasi-steady flight condition is assumed to represent the instantaneous flight state of the kite. This means that the system is constantly at its equilibrium position and forces are always balanced.

First, a simple two-dimensional theoretical model involving only the aerodynamic forces and the tether tension is considered. This massless model is adopted to investigate two distinct testing strategies. Although both methods take advantage of the TU Berlin test bench operating at same steady wind conditions, they involve different flying maneuvers. Indeed, the usual dynamic maneuvers established by Hummel [48] are confronted against a new method of static maneuvers. This methodology comparison shall cover the first research question.

For the second research question, the aerodynamic properties previously derived from the massless model are amended by independently including:

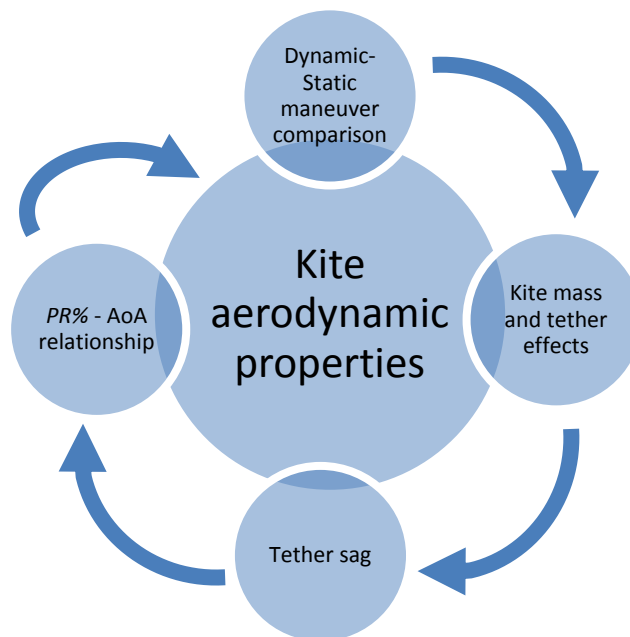
- the weight of the kite
- the weight of the tether lumped to the kite
- the aerodynamic forces of the tether lumped to the kite
- the combination of all these forces together

This allows to estimate their effects on the aerodynamic properties of the kite compared to the massless case. Depending on their influence, some aspects can be neglected without compromising much the accuracy of the results.

So far, the different theoretical models assume the tether between the test bench and the kite to be straight. In order to judge whether this assumption is valid or not, a more detailed analytical model of the tether is introduced by taking into account the distributed load of the weight, drag and lift. Eventually, the sag of the tether can lead to appreciable changes in the computed aerodynamic properties of the kite. Thus, the third research question is assessed.

At this point, it is worth mentioning that the major parameter considered so far for expressing the kite aerodynamic properties is the power ratio. With the aim of providing appropriate data for numerical research, a more generic parameter, namely the angle of attack, is investigated and derived from measurement. This is achieved by relating the line configuration with the corresponding kite position and shall answer the last research question.

The following diagram summarizes the succession of research questions.



Eventually, an exhaustive description of the systematic and random errors is detailed to estimate the accuracy of the measurement and results achieved. Errors stem from the intrinsic inaccuracies of sensors and uncertainties from averaging multiple maneuvers. In addition, simplifications and assumptions also play a role in the accuracy of the results.

4 Experimental Setup and Methodology

The following chapter outlines the key elements involved in the investigation. First, the kites and the environmental conditions are listed. Then, the test bench is described together with the accuracy of the different sensors. Eventually, the different testing procedures are detailed.

4.1 Kites

Three different kites are investigated during this work. The Hydra V5 from [Genetrix Kiteboarding](#) is a Supported Leading Edge (SLE) kite with a total area of 14 m². This wing profile serves as basis for up-scaled kite prototypes operating with the pumping Kitepower system. Secondly, the Mixt is a semi-rigid down-scaled version of the Hydra V5, with a total area of 9 m². Thirdly, the Vegas 2015 designed by [North Kiteboarding](#) is a C-shape kite with a total surface area of 10 m². The Hydra V5 and the Vegas 2015 are presented in Figure 4.1 and Figure 4.2 respectively¹. Steering lines are shown with red (left) and blue (right) colours while front lines are in black. The kite characteristics are summarized in Table 4.1. These kites have been operated with 24 m long lines with a power range of 500 mm.



Figure 4.1 Hydra V5. Modified from [64].



Figure 4.2 Vegas 2015. Modified from [65].

Table 4.1 Kite characteristics

Characteristics		Hydra V5	Mixt	Vegas 2015
Type		SLE kite	SLE kite	C-kite
Total surface area	m ²	14	9	10
Projected area	m ²	11.7	7.5	~ 5.5 ²
Kite mass	kg	4.29	x ¹	3.45
Bar + lines mass	kg	1.6	1.6	1.6
Number of struts		6	6	5
Number of lines		4	4	5
Wind range	kt	9 - 30	unknown	15 - 29
	m/s	4.6 - 15.4	unknown	7.7 - 14.9

¹ For confidential reasons, the Mixt cannot be presented

² Value estimated from previous version of North Vegas 2013 [79] and 2014 [80]

4.2 Testing Conditions

Tests to assess the aerodynamic kite performances were performed on the 23rd of November 2016 on the airfield of Pütznitz (DE). The track is a 1.5 km long road made of flat concrete. Measurements were achieved by a car pulling the kite back and forth multiple times. Although data were also recorded during turns, only data obtained during straight drives, as shown in Figure 4.3, are considered. The wind on this day was very light ranging from 0 m/s to occasional maximum of 2 m/s. Because of the airfield is surrounded by fields of grass, the Power Law exponent is estimated to be 0.15. The air density ρ_{air} is assumed to be 1.225 kg/m³.

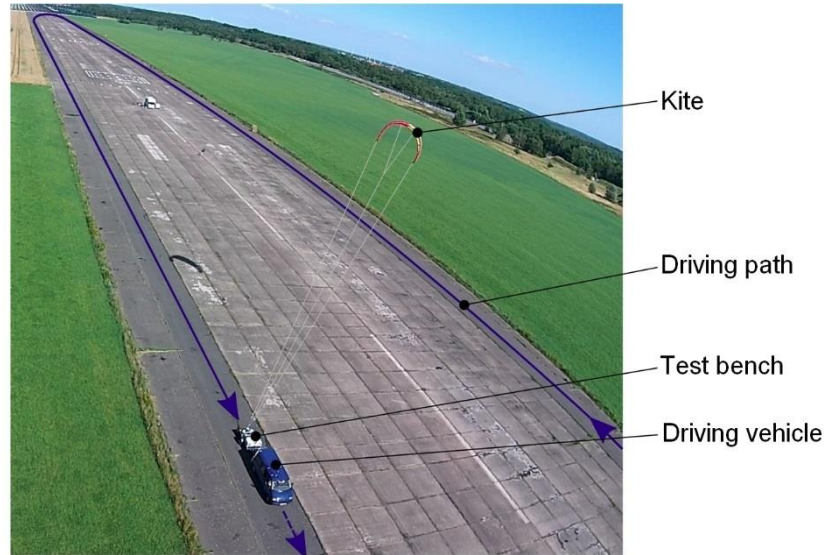


Figure 4.3 Pütznitz airfield, 1.5 km long track. Modified from [50].

4.3 Test Bench - TETA Setup

The test bench developed by Hummel [50] is used to measure the kite state. As briefly introduced in Chapter 2.4.2, the car-trailer system is equipped with multiple sensors to record relevant information. The logged data include forces in the different lines, namely force in the power line F_P , forces in the left F_{LS} and right F_{RS} steering line but also azimuthal Φ_g and elevation θ_w angles. In addition, both wind speed V_w and wind direction χ are provided by an anemometer mounted on the roof of the car at 3 m above ground level. An illustration of the system with the different forces and angles is presented in Figure 4.4. Moreover, the sampling rate is set to 50 Hz. Both azimuthal Φ_g and elevation θ_w angles are obtained by a complex combination of three angular measurements, namely the elevation θ_o , azimuthal Φ_{o1} and pivot Φ_{o2} angles. The first sensor measures the tether elevation angle whereas the two others indicate the angular position of the line into the horizontal plane. These angular sensors are illustrated in Figure 4.5. Nevertheless, the angular relationship to derive both azimuthal Φ_g and elevation θ_w angles is computed internally. Thus, Φ_g and θ_w are directly the channel outputs. The azimuthal angle Φ_w considering the wind direction is the composition of both azimuthal angle Φ_g and wind direction χ , as given in Equation (4.1). The complex angular relationship is explained in detail within Hummel's work [50]. It is important to note that the power line is mechanically controlled by motors whereas steering inputs are given by the pilot located inside the van. The pilot has thus no influence on the power setting of the kite. By systematically using the same bar and lines, the test bench has proved its ability to extract aerodynamic properties of wing from the kitesurf industry in a reliable and repeatable manner. Indeed, the 24 m long lines with the 500 mm of power range available allow to investigate most of the surf-kites present on the market.

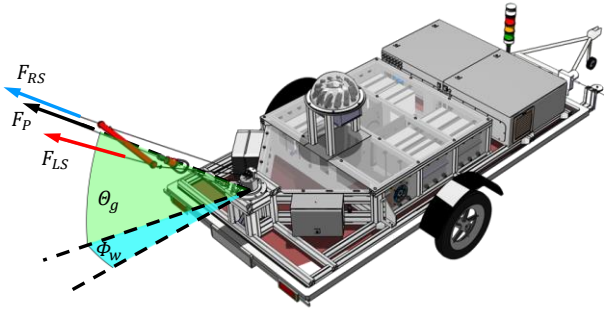


Figure 4.4 TETA towing test bench. Modified from [50].

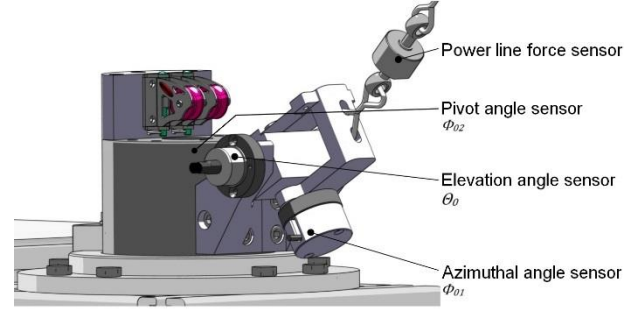


Figure 4.5 Close view of the angular sensors. Modified from [50].

When flying the kite downwind, the glide ratio can simply be computed from the tether elevation angle. However, as soon as the kite deviates from the downwind situation, this two-dimensional approach is no more valid. Indeed, the elevation angle varies throughout the wind window for the same glide ratio. Figure 4.6 illustrates this situation where a constant glide ratio is represented by the intersection of the red plane with the grey wind window. Nevertheless, a relationship can be established between elevation and azimuthal angles in order to extract the glide ratio even if the kite is not flying exactly downwind. From the right-hand side picture of Figure 4.6, the green angle ϑ_w between the downwind direction and the tether (defined here as the apparent elevation angle) remains constant for the same glide ratio, independently of the position of the kite. Therefore, Equation (4.2) can be deduced with angles shown in Figure 4.6. Eventually, the glide ratio can be computed with Equation (5.1) by substituting β with ϑ_w . For the special case of no azimuthal deviation, namely $\Phi_w = 0$, it can be noted that $\theta_w = \vartheta_w$ and also equals the tether elevation angle β .

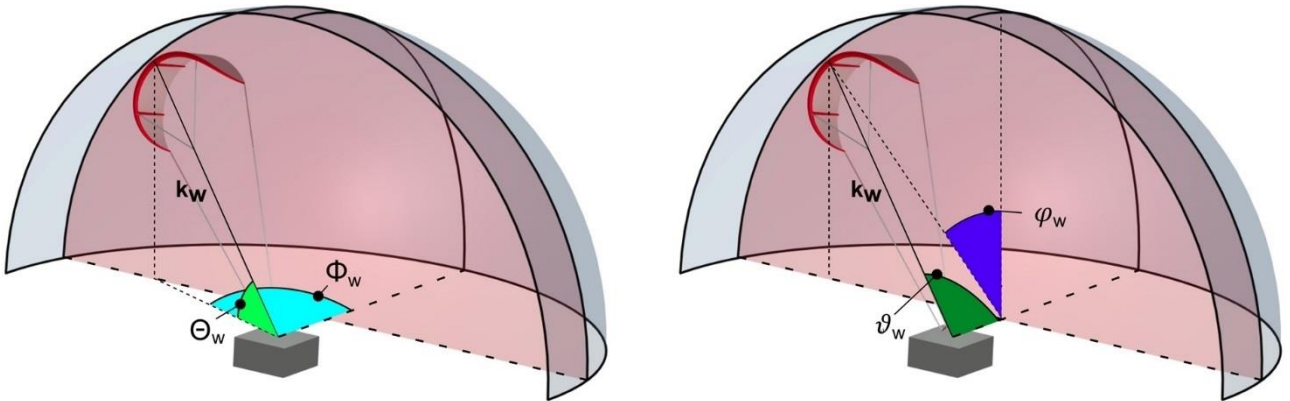


Figure 4.6 Wind window with constant glide ratio (red plane) [50].

$$\theta_w = \theta_g + \chi \quad (4.1)$$

$$\vartheta_w = \cos^{-1}(\cos \theta_w \cos \Phi_w) \quad (4.2)$$

4.3.1 Accuracy of Measurement

Each sensor has a given accuracy which is indicated by its absolute error Δ . For instance, the intrinsic accuracy regarding the force and angular sensors previously described as well as the anemometer are shown in Table 4.2. In order to estimate the accuracy of both azimuthal Φ_w and elevation θ_w angles, an error propagation is performed through the complex angular relationship. To be on the conservative side, only the maximum absolute error is considered for Φ_w and θ_w . Eventually, a second error propagation according to Equation (4.2) is carried out to estimate the accuracy of the apparent elevation angle ϑ_w which is then used to compute the glide ratio. The absolute error θ_w , Φ_w and ϑ_w are presented in Table 4.3.

Table 4.2 Sensor accuracy

Sensor		Absolute error
Power line force	ΔF_P	± 10 N for 5000 N
Right steering line force	ΔF_{RS}	± 0.2 N for 1000 N
Left steering line force	ΔF_{LS}	± 0.2 N for 1000 N
Elevation angle	$\Delta \theta_0$	$\pm 0.72^\circ$
Azimuthal angle	$\Delta \Phi_{01}$	$\pm 0.72^\circ$
Pivot angle	$\Delta \Phi_{02}$	$\pm 0.3^\circ$
Wind speed	ΔV_w	± 0.05 m/s
Wind direction angle	$\Delta \chi$	$\pm 1^\circ$

Table 4.3 Accuracy of computed values

Computed value		Absolute error
Elevation angle	$\Delta \theta_w$	$\pm 1.018^\circ$
Azimuthal angle	$\Delta \Phi_w$	$\pm 13.935^{\circ 3}$
Apparent elevation angle	$\Delta \vartheta_w$	$\pm 1.788^\circ$

These values are retrieved from Hummel's work. They correspond to the maximum possible absolute. More details about the error analysis and propagation can be found in the corresponding PhD thesis [50]. For the purpose of this study, only the absolute error of the forces, the wind speed and the apparent elevation angle are relevant.

4.4 Testing Procedure

4.4.1 Dynamic Maneuvers

The first testing approach corresponds to the procedure established by Hummel [50]. It consists of multiple dynamic maneuvers performed one after each other. As the towing test rig is driven at constant speed of 22 kt (11.3 m/s), the kite is repetitively powered from 0 to 100% within 4 seconds. Figure 4.7 shows 11 dynamic maneuvers achieved during one drive of 1.5 km long. It can be seen that the power ratio linearly increases from 0 to 100% in 4 seconds⁴. As soon as the full power situation is reached, the power setting returns to its initial state and begins a new dynamic maneuver. Portions before 570 and after 675 seconds indicate the start and the end of the road respectively. In total, the track has been covered 9 times while towing the Hydra V5 kite. Thus, roughly a hundred of dynamic maneuvers have been performed in 25 minutes of test.

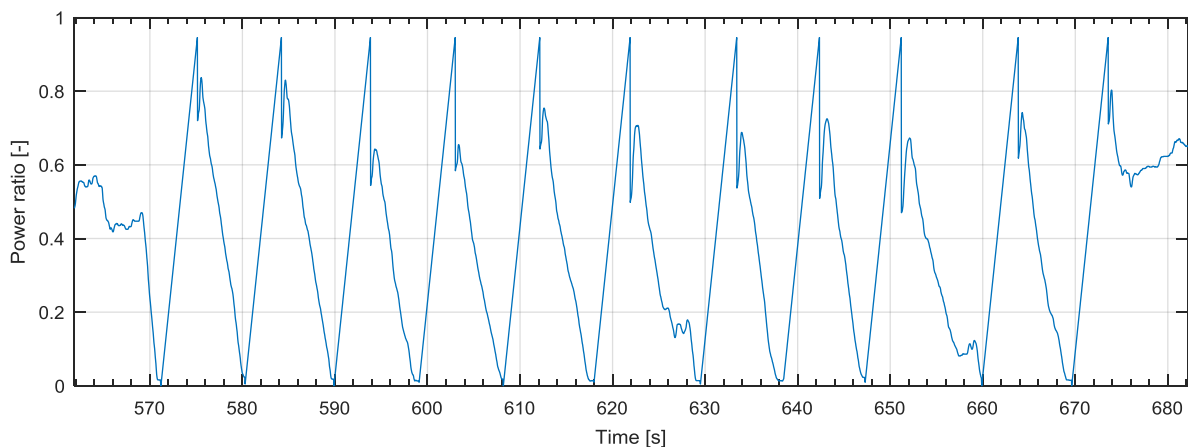


Figure 4.7 Dynamic maneuvers, 0 - 100% power within 4 seconds, for the Hydra V5 at 22 kt.

³ J. Hummel declared that this absolute error is too significant for further calculation and an alternative angle φ_w has to be considered instead.

⁴ 100 % actually corresponds to 508 mm of power range. Thus, the power ratio does not exactly reach 100 % when fully powered with 500 mm.

4.4.2 Static Maneuvers

The new testing procedure consists of static maneuvers. As soon as the car-trailer system terminates its turn and starts to drive on the straight part of the road at 22 kt (11.3 m/s) or 29 kt (14.9 m/s), the kite is set with a fixed power setting for an entire drive. Figure 4.8 represents one testing campaign of 9 distinct power settings ranging from 10 to 90% with a 10% increment. It can be noticed that one fixed power setting is generally kept for about 2 minutes. In order to remove the potential influence of a light wind, two testing campaigns have been achieved by alternatively switching the power setting from one side of the track to another. In other words, power ratio of 10, 30, 50, 70, 90% were set on one side of the track for the first campaign and on the other side for the second test campaign. However, due to time constraint, this has been only possible for the Hydra V5 at 22 kt and partially for the Mixt at 22 kt. It can be noted that for technical reasons regarding the test bench, the power ratio of 0% was not possible to investigate. On the other hand, the upper limit is defined by the kite itself and its stall point.

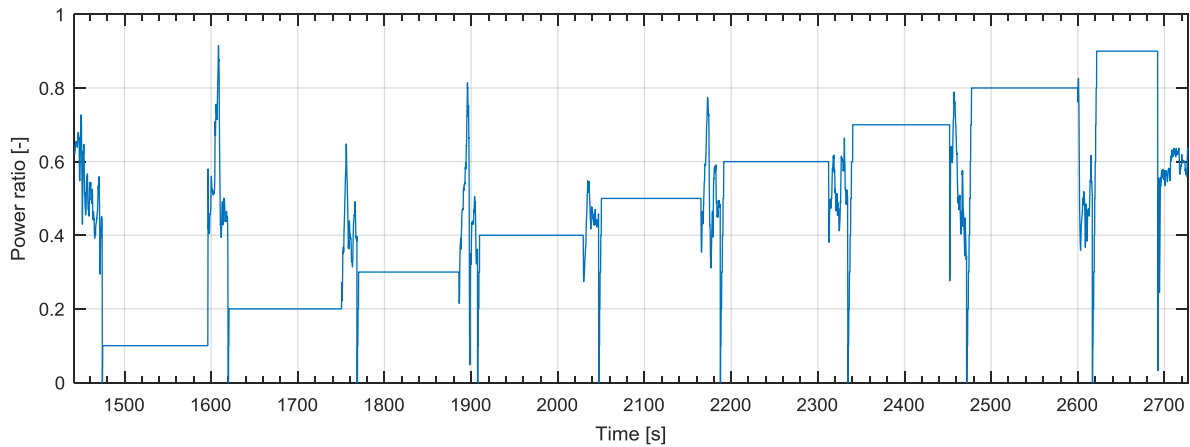


Figure 4.8 Static maneuvers with constant power setting, for the Hydra V5 at 22 kt.

4.4.3 Summary

The different tests achieved are listed in the following Table 4.4.

Table 4.4 Experiment summary

Kite	Speed	Maneuver	# Maneuvers	Duration (effective)
Vegas 2015	22 kt	Static	10	30 min (18 min)
Mixt	22 kt	Static	16	49 min (28 min)
Hydra V5	22 kt	Static	19	48 min (31 min)
Hydra V5	29 kt	Static	12	19 min (10 min)
Hydra V5	22 kt	Dynamic	95	25 min (6 min)

4.5 Power Ratio Angle

With the aims of relating the angle of attack to the power ratio $PR\%$, the power ratio angle ε , as shown in Figure 4.9, has to be determined experimentally. The relationship between the power ratio $PR\%$ and the power ratio angle ε depends not only on the kite's geometry but also on the bridle and line setup. Figure 4.9 illustrates two extreme cases, namely fully depowered kite (green) and the fully powered kite (red). The kite bridles are represented with thick lines ending with a dot whereas the thinner lines symbolize the 24 m long lines. When the kite is depowered, the handle bar is pushed towards the kite, which in turn moves the trailing edge of the kite further away. On the contrary, when the handle bar is pulled towards the pilot, the back lines are shortened and this brings the trailing edge closer to the pilot. It is important to recall that in this case (full power), the length of both front and back lines are equal. However, the length of front and back bridles are not necessary the same.

In order to establish the link between the power ratio and its corresponding angle ε , the kite and its lines are investigated according to Figure 4.9. The kite is set straight on its trailing edge (as shown in Figure 4.10) while the power line is tensioned and maintained horizontally throughout the measurement session. Thus, the virtual line normal to the power line is vertical and serves as benchmark for measuring the angle (dashed black line). An angular sensor (illustrated by a rectangle) is mounted on a carbon rod which is attached from the trailing edge to the lower part of the leading edge (colourful dashed lines). Thus, the power ratio angle can be obtained directly from the sensor. The measurements are performed indoors. The power range is systematically covered by increment of 3 cm. It should be mentioned that the lines with 500 mm of power range were not available for this measurement. Thus, the experiment is achieved with a similar set of 24 m long lines but with a power range of 360 mm. For each power setting, both front and back lines are equally tensioned by manually pushing the kite backwards. Simultaneously, the angle from the sensor is logged for 20 seconds. The MAD of the measurement gives an accuracy of +/- 0.33°.

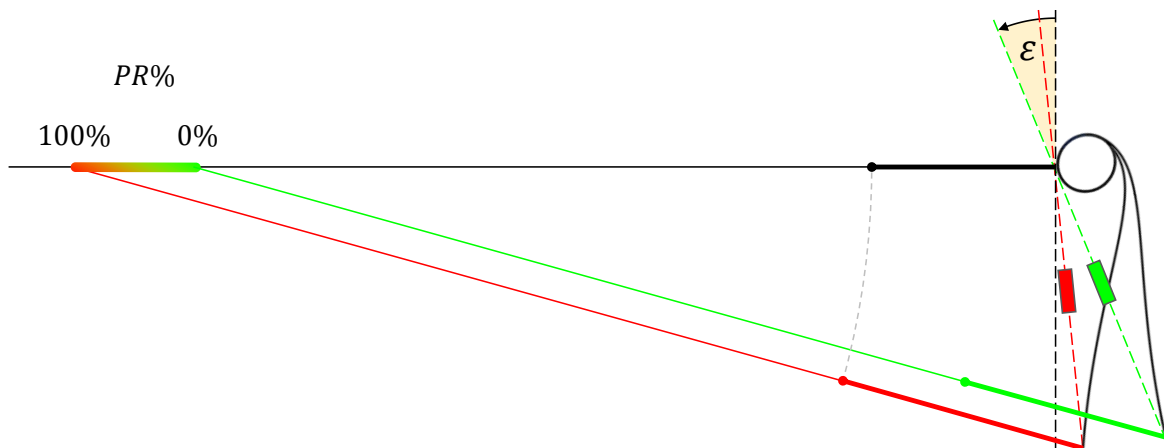


Figure 4.9 Schematic setup to assess the power ratio angle ε .



Figure 4.10 Angular sensor mounted on carbon rod.

5 Theoretical Models

The present chapter describes and justifies the relevant analytical theory used to assess the aerodynamic properties. In order to calculate C_L , C_D and L/D from measurement data, first a point mass kite and a straight tether are assumed. In a second step, a more realistic viewpoint is assumed by refining the point mass model with tether aerodynamic forces and weight influences. Eventually, the sag of the tether is also introduced and detailed. Finally, the approach to assess the angle of attack is described.

5.1 General Aspects

The glide ratio can be established either for the kite itself or for the kite-tether-system. Only the intrinsic glide ratio of the kite is considered for the present paper. For this, a quasi-steady approach is chosen neglecting the inertia of the kite. Precisely, this means that the kite moves without accelerations along a trajectory of discretised path points while an equilibrium of forces is assumed in every path point.

In addition, it is important to note that the following analytical models are two-dimensional representations of the situation. However, although the pilot during test tries to keep the kite in downwind position, the kite might occasionally deflect to the right or left of the wind window and therefore deviates from the 2D representation. Nevertheless, the glide ratio can still be assessed. This is being accounted for through a suitable choice of coordinate system developed previously in Chapter 4.3.

The key advantage of the here employed testing setup is that the testing is performed at a no wind condition. Thus, the apparent wind speed V_a at the kite is in principle known. In reality, a low ground wind speed may be present. Since the experiments were achieved along a wide flat area with very calm wind, the apparent wind is considered to be parallel to the ground. Moreover, it is assumed that the kite is always facing into the wind. Although the natural wind is very weak (< 2 m/s) at the height of the anemometer, its magnitude at the altitude of the kite might be slightly greater. However, the natural wind profile is neglected for this work. Thus, the apparent wind speed experienced by the kite corresponds to the wind speed recorded at the anemometer, namely $V_a = V_w$. Nevertheless, the Power Law (Equation (2.17)) is adopted to evaluate the error following this assumption.

5.2 Two-Dimensional Point Model

A simple 2D point model of a weightless kite is firstly implemented to compute the aerodynamic properties. This point model not only serves as the simplest analytical model but also corresponds to the model adopted by Hummel. Since results from his investigation shall be compared to the ones achieved in this thesis, the same model has to be considered for consistency. From geometrical consideration as shown on the left-hand side of Figure 5.1, Equation (5.1), which relates aerodynamic forces to the tether elevation angle β , can be established for the massless case. At this point, the tether force F_t balances the aerodynamic force F_a as shown in Equation (5.2).

$$\frac{L}{D} = \tan(\beta) \quad (5.1)$$

$$\sum \mathbf{F}_i = \mathbf{F}_t + \mathbf{F}_a = 0 \quad (5.2)$$

If the mass is taken into account, geometric considerations lead to Equation (5.3) deduced from the right-hand side of Figure 5.1. This constitutes the 2D point mass model which is considered to gauge the kite mass effect. Indeed, neglecting the kite mass in the first place simplifies the calculation but leads to a underestimation of the glide ratio, especially for high elevation angles β . The force equilibrium is given in Equation (5.4) where $m = m_k$ when kite mass is included. Eventually, by knowing the tether elevation angle β together with the tether force F_t and the weight of the kite, both lift L and drag D forces as well as the kite glide ratio can be calculated with the help of Equation (5.5) and Equation (5.6). Note that by assuming the apparent wind speed to be parallel to the ground, the weight $m\mathbf{g}$ is collinear to the lift L .

$$\frac{L - m_k g}{D} = \tan(\beta) \quad (5.3)$$

$$\sum \mathbf{F}_i = \mathbf{F}_t + \mathbf{L} + \mathbf{D} + m\mathbf{g} = 0 \quad (5.4)$$

$$C_L = \frac{C_R}{\sqrt{1 + \left(\frac{L}{D}\right)^{-2}}} \quad (5.5)$$

$$C_D = \frac{C_L}{\frac{L}{D}} \quad (5.6)$$

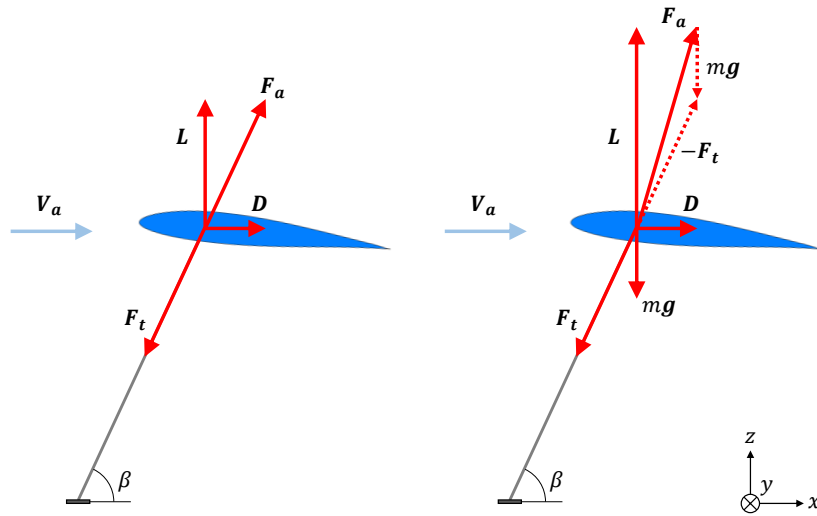


Figure 5.1 Point model without mass (left) and with mass (right).

5.3 Tether Mass Contribution

To capture the effect of tether mass, the tether weight has also to be taken into account when assessing the kite aerodynamic performance. Indeed, since the tether mass can contribute for a large share of the total mass (up to 40 %), its weight might have an even stronger effect than the kite mass. In order to consider the tether mass within the point mass model, the reasoning of van der Vlugt [54] and Noom [58], shown on Figure 2.38, is applied to lump the tether mass to the kite. Thus, the effective tether weight lumped to the kite and given in Equation (2.31) for spherical coordinates (r, θ, φ) is translated into Equation (5.7) for Cartesian coordinates (x, y, z) defined in Figure 5.1. The derivation is detailed in Annexe 10.3. Note that the tether elevation angle β and the azimuthal angle θ are complementary. The total tether mass m_t is given in Equation (5.8).

$$\mathbf{F}_{g,t} = -m_t g \begin{pmatrix} \frac{1}{2} \cos \beta \sin \beta \\ 0 \\ \frac{1}{2} \cos^2 \beta + \sin^2 \beta \end{pmatrix} \quad (5.7)$$

$$m_t = \frac{1}{4} \rho_t \pi d_t^2 l_t \quad (5.8)$$

By comparing the apparent tether weight $F_{g,t}$ separately along x -axis and z -axis, it can be noticed that the major contribution of Equation (5.7) stems from the vertical axis as intuitively expected. Figure 5.2 illustrates both components along x - and z -axis as well as the magnitude of the apparent weight for a given tether weight of 10 [N]. One can notice that the lumped tether weight $F_{g,t}$ varies from 50% to 100% of the total tether weight from $\beta = 0^\circ$ to $\beta = 90^\circ$ respectively.

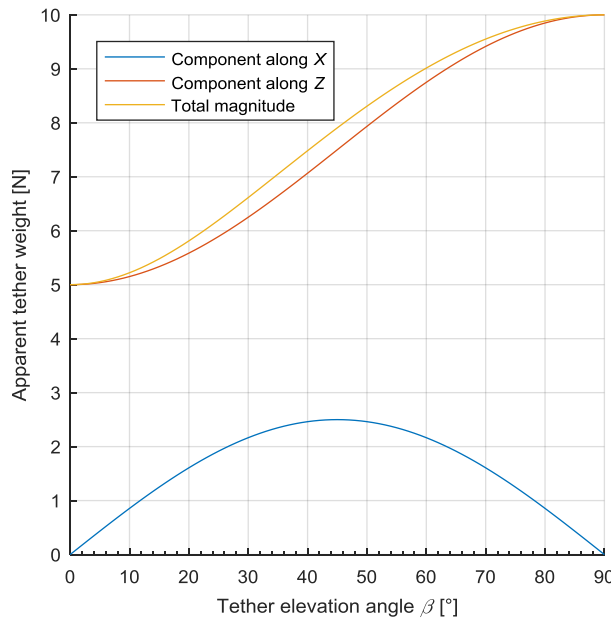


Figure 5.2 Components of the apparent tether weight $F_{g,t}$ for a magnitude of 10 [N].

Although the contribution along x -axis is relatively small in comparison to the vertical component, its effect is still considered for the calculation. Therefore, corrected aerodynamic coefficients are established by applying the force equilibrium of Equation (5.4) on both x and z -axis as given in Equation (5.9) and Equation (5.10) respectively. C_R and L/D are then computed thanks to Equation (2.27) and Equation (2.28) respectively.

$$ox: \quad \frac{1}{2} \rho_{air} A_{ref} C_D V_a^2 - F_t \cos \beta - m_t g \left(\frac{1}{2} \cos \beta \sin \beta \right) = 0 \quad (5.9)$$

$$oz: \quad \frac{1}{2} \rho_{air} A_{ref} C_L V_a^2 - F_t \sin \beta - m_t g \left(\frac{1}{2} \cos^2 \beta + \sin^2 \beta \right) = 0 \quad (5.10)$$

The reason for not choosing the constant effective mass established by Fagiano [53] comes from the fact that the effective tether weight should practically vary with the elevation angle.

5.4 Tether Aerodynamics

Equation (2.29) for considering the effective tether drag assumes zero velocity at the lower tether part. However, the entire system is in motion when tested with the TETA setup. Consequently, the lower tether section also experiences incoming wind speed and thus drag, which influences the aerodynamic performance of the kite. Since tests were performed in a very weak wind, the natural wind speed is assumed to be negligible in comparison to the velocity of the car. In that way, the wind speed recorded at the anemometer is equivalent to the air speed experienced by both kite and tether, namely $V_a = V_w$. With this in mind, the contribution of the tether drag acting on the kite is derived the same way as achieved by Houska [38], but corrected by assuming a uniform incoming wind speed instead of a linear profile. The according formulas are presented in the following Equation (5.11) to Equation (5.14). The momentum $M_{D,t}$ generated by the infinitesimal drag forces has to be equal to the one created by the equivalent drag force acting on the kite. If a longer tether (> 50 m) was considered, the apparent wind speed would have to be adapted accordingly, with the Power Law for instance. It should be mentioned that the following derivation holds for one single tether. Therefore, the equivalent force can simply be multiplied by the number of lines.

$$dM_{D,t} = r \sin \beta dD_t = r \sin \beta \frac{1}{2} C_{D,t} \rho_{air} d_t V_a^2 dr \quad (5.11)$$

$$M_{D,t} = \frac{1}{4} C_{D,t} \rho_{air} d_t l_t^2 \sin \beta V_a^2 \quad (5.12)$$

$$M_{D,t} = D_{t,e} l_t \sin \beta \quad (5.13)$$

$$D_{t,e} = \frac{1}{4} C_{D,t} \rho_{air} d_t l_t V_a^2 \quad (5.14)$$

Besides drag, the tether also experiences aerodynamic lift [63], which can be interpreted as extra “weight” since it points downwards. Although small, its magnitude is not negligible and might alter the measurement. The same momentum approach is applied to establish the equivalent tether lift acting on the kite. The integrated angular momentum generated by the infinitesimal tether lift must be equal to the momentum inflicted by the equivalent tether lift applied on the kite. Equation (5.15) gives the equivalent tether lift. Grouping both lumped drag and lift together with the lumped tether weight of Chapter 5.3 constitutes the so-called lumped model.

$$L_{t,e} = \frac{1}{4} C_{L,t} \rho_{air} d_t l_t V_a^2 \quad (5.15)$$

Both aerodynamic coefficients of the tether are based on formulas provided by Hoerner [66]. As shown in Equation (5.16) and Equation (5.17), these expressions take into account the inclination of the tether.

$$C_{D,t} = 1.1 \sin^3 \beta + 0.2 \quad (5.16)$$

$$C_{L,t} = 1.1 \sin^2 \beta \cos \beta \quad (5.17)$$

5.5 Tether Sag Model

So far, the tether is assumed to be straight since the TETA test bench flies the kite by means of short lines. If longer lines were used, the sagging of the tether would increase and could not be neglected anymore. Here, the effect of the tether sag is introduced to estimate if the straight tether assumption is valid for the TETA setup. Practically, the sag of the line stems from distributed weight, lift and drag forces acting along the tether. In order to consider the extreme case, these three forces are taken into account, as illustrated in Figure 5.3. Their infinitesimal expressions are given in Equation (5.18), Equation (5.19) and Equation (5.20) respectively. Again, the aerodynamic coefficients are computed with formulas of Hoerner given in Equation (5.16) and Equation (5.17). Since the worst case is to be considered for the

assumption validation, the natural wind profile is taken into account in addition to the speed of the car V_{car} . The Power Law in Equation (2.17) is adopted hereafter. The corresponding differential formulas are given in Equation (5.21), Equation (5.22) and Equation (5.23). Their derivations are detailed in Annexe 10.4. In addition, the apparent wind speed, including car velocity V_{car} and natural wind profile V_w , is expressed in Equation (5.24). The boundary conditions required to solve the differential equations system are given in Equation (5.25), Equation (5.26) and Equation (5.27).

$$dW = g dm_t = g \pi \frac{1}{4} d_t^2 \rho_t dr = g \rho_t' dr \quad (5.18)$$

$$dL_t = \frac{1}{2} C_{L,t} \rho_{air} d_t V_a^2 dr \quad (5.19)$$

$$dD_t = \frac{1}{2} C_{D,t} \rho_{air} d_t V_a^2 dr \quad (5.20)$$

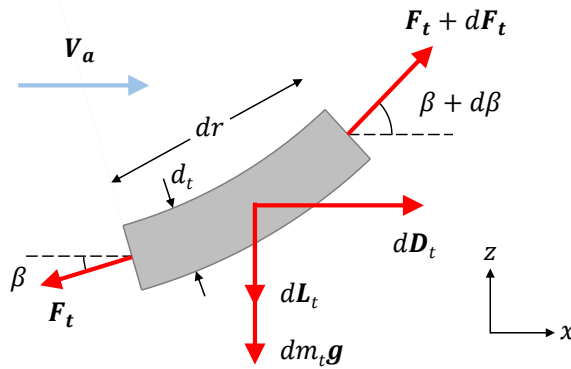


Figure 5.3 Force acting on an elemental length of a kite tether.

$$\frac{d\beta}{dz} = \frac{g \rho_t'}{\tan \beta F_t} + \frac{\rho_{air} d_t V_a^2}{2 F_t} \left(\frac{C_{L,t}}{\tan \beta} + C_{D,t} \right) \quad (5.21)$$

$$\frac{dF_t}{dz} = g \rho_t' + \frac{1}{2} \rho_{air} d_t V_a^2 \left(C_{L,t} - \frac{C_{D,t}}{\tan \beta} \right) \quad (5.22)$$

$$\frac{dx}{dz} = \frac{1}{\tan \beta} \quad (5.23)$$

$$V_a(z) = V_{car} + V_w(z_{ref}) \left(\frac{z}{z_{ref}} \right)^\alpha \quad (5.24)$$

$$\beta(z = 0) = \beta_{ground} \quad (5.25)$$

$$F_t(z = 0) = F_{t,ground} \quad (5.26)$$

$$x(z = 0) = 0 \quad (5.27)$$

At this point, the tether weight as well as both lift and drag force of the tether are included in the differential equation system. Eventually, the tether force at the kite connection point is greater than the tether force logged on the test bench, namely $F_{t,k} > F_t$. Therefore, the force equilibrium at the kite (Equation (5.4)) is adjusted by considering the computed $F_{t,k}$ instead of F_t . This is referred as the tether sag model.

5.6 Angle of Attack Assessment

In numerical simulations, it is common for researchers to work with the angle of attack. Thus, the aerodynamic curves, which have so far been derived with respect to the so-called power ratio, should be adapted accordingly. The method endorsed by Costa [47] is adjusted by assuming an horizontal incoming wind speed V_a . In this case, the angle of attack α is equivalent to the pitch angle ψ (Equation (2.12)). Thus, from now on, both terms can be used equally to mention the same quantity.

As illustrated in Figure 5.4 for a fixed elevation angle, the pitch angle ψ varies with the power ratio $PR\%$. For low power ratio, the back lines are longer and reduce the pitch angle. The close view of the full-power kite, shown in Figure 5.5, allows to establish the pitch angle from the tether elevation angle β and the power ratio angle ε . This relationship is given in Equation (5.28) where η is the offset angle between the central chord and the normal to the tether. This offset is formulated in Equation (5.29) where δ is the angle between the central chord and the line from the trailing edge to the bottom of the leading edge.

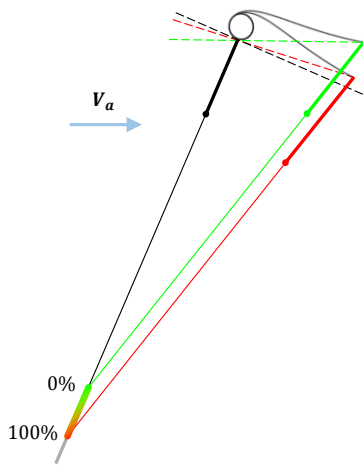


Figure 5.4 Pitch angle variation with respect to the power ratio.

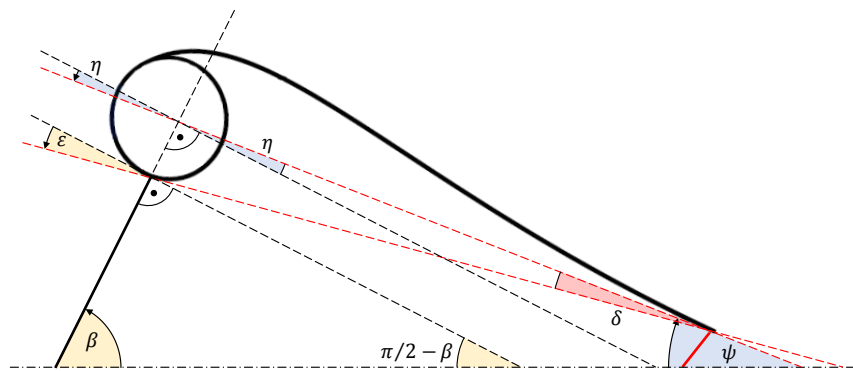


Figure 5.5 Close view of the full power situation. Blue: unknown angles. Yellow: measured angles. Red: geometry angle.

$$\alpha = \psi = \left(\frac{\pi}{2} - \beta\right) - \eta \quad (5.28)$$

$$\eta = \varepsilon - \delta \quad (5.29)$$

It should be mentioned that both power ratio angle ε and elevation angle β are interconnected by the power setting. Indeed, as the kite is powered up, the front lines are extended, which increases the pitch angle for a short time. However, by having a greater pitch angle, the pressure difference between both sides of the kite increases which in turn generates a larger lift force. Consequently, the kite gains in altitude and the elevation angle increases. As a result, the pitch angle diminishes as the kite moves forward. To summarize, as the power ratio increases, the power ε ratio angle reduces whereas the elevation angle β gets larger.

It must be specified that the angle β on Figure 5.5 actually corresponds to the front line elevation angle. Costa [47] approximated this angle by the elevation angle measured at the trailer. However, the sag of the tether, leading to a greater elevation angle at the kite β_k , might be considered depending on its effect on 24 m long line. In addition, the main line below the handle bar (grey line on Figure 5.4) is not perfectly aligned with the power line. Indeed, it would rather point towards the centre of pressure on the kite if the lines were straight. Thus, a small angle ζ appears at the junction of handle bar and can be taken into account by adding its value to β . All these considerations are examined independently.

6 Results

The following section firstly describes the processing applied to the raw data obtained from the different measurements. Secondly, the aerodynamic curves are extracted for both methodologies and then compared against each other. The aerodynamic performance coefficients are then corrected by including the aerodynamic effects of the tether as well as its weight. In addition, the sag of the tether and its ensuing effects are investigated. Eventually, the results are tried to be related to the angle of attack of the kite. The subsequent results have been achieved with the help of MATLAB software [67].

6.1 Data Processing

This chapter describes the way that the relevant data has been extracted and processed. Since both dynamic and static methodologies are practically different, their corresponding data processing are achieved independently. Nevertheless, both approaches deal with the same channel outputs which are enumerated in Table 6.1.

Table 6.1 Channel outputs

Channel output	Symbol	Unit	MATLAB name
Time	t	second	Time
Power ratio	$PR\%$	-	Power
Power line force	F_{PL}	N	ForcePL
Right steering line force	F_{RS}	N	ForceRS
Left steering line force	F_{LS}	N	ForceLS
Azimuthal angle	Φ_g	rad	Phi_g
Elevation angle	θ_w	rad	Theta_gw
Wind speed	V_w	m/s	WindSp
Wind direction angle	χ	rad	WindDi

Since multiple measurements are achieved for one supposedly same condition, the general aspect of this given condition must clearly appear without being altered by non-representative samples. For this reason, the median is preferred over the arithmetic mean. Indeed, the median is less sensible to outliers whereas the mean is inevitably affected by any single value that is too high or too low. In addition, although the mean works greatly for symmetric distribution, the median is not only adapted for symmetric distribution but does also suit well for skewed distribution [68]. Therefore, the median is thought to be more suitable to derive the central tendency. Accordingly, the median absolute deviation of the median (MAD) is considered over the standard deviation (STD) for gauging the statistical dispersion. Indeed, for the STD, the distance to the mean is squared which gives to outliers a strong influence. On the contrary, the MAD is more resilient to outliers [69]. The median absolute deviation of the median is given in Equation (6.1). Note that from now on, the term “average” refers to the median. It is worth mentioning that if a normal distribution is assumed, 50% of the individual measurements are enclosed by the value of +/- MAD.

$$MAD = \text{median}(|X_i - \text{median}(X)|) \quad (6.1)$$

6.1.1 Dynamic Maneuvers Processing

The first step of data processing is to find the portions of measurement which contain the relevant information. This is achieved with the MATLAB *Pol.m*⁵ function which searches for the indexes corresponding to 0 and 100% of power ratio. By knowing these indexes, the relevant sequences of data can be extracted. The raw data are then smoothed by applying a moving average filter of 0.24 second corresponding to 12 samples. This value has been selected after examination of the raw data. Figure 6.1 shows the typical progression of the elevation angle θ_w for one given dynamic maneuver. One can notice that fluctuations occur during the second half of the maneuver where 9 oscillations can be counted over roughly 2.2 seconds. This gives a period of 0.2444 second. Oscillations with similar period are also observed within other channels. At first, it was assumed that these oscillations were due to small swinging of the tether. However, Hummel [48] indicates that the trailer presents a frequency of roughly 4 Hz. Consequently, the duration for the moving average filter is rounded to 0.24 second. In this way, the filtered curve (orange) still shows the general trend of the raw signal (blue) without the oscillations. Once the filter has been applied to the angular signals of Table 6.1, Equation (4.1) and Equation (4.2) are successively computed to obtain the instantaneous apparent elevation angle ϑ_w for each dynamic maneuver. Figure 6.2 shows this angle for the 95 dynamic maneuvers achieved. The corresponding median and its median absolute deviation are illustrated with red colour. Since similar oscillations have been observed through force channels, the same filter is applied to each individual force signals. Then, the total steering force F_s is evaluated with Equation (6.2). Next, Equation (6.3) allows to compute the total tether force F_t that is transmitted to the trailer. Figure 6.3 shows the tether force for individual dynamic maneuvers and their corresponding median. Although the wind speed recorded at the anemometer is relatively stable, the same moving average filter is applied as well.

$$F_s = F_{RS} + F_{LS} \quad (6.2)$$

$$F_t = F_{PL} + F_s \quad (6.3)$$

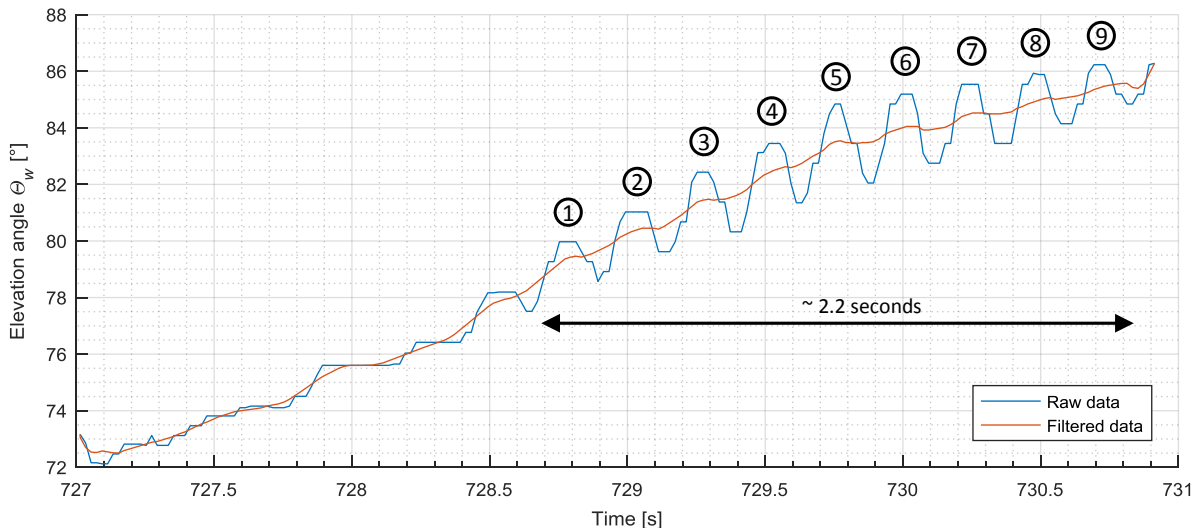
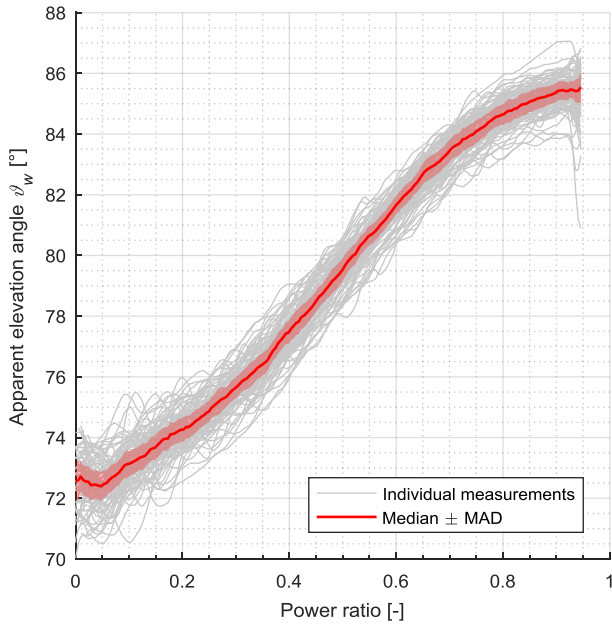
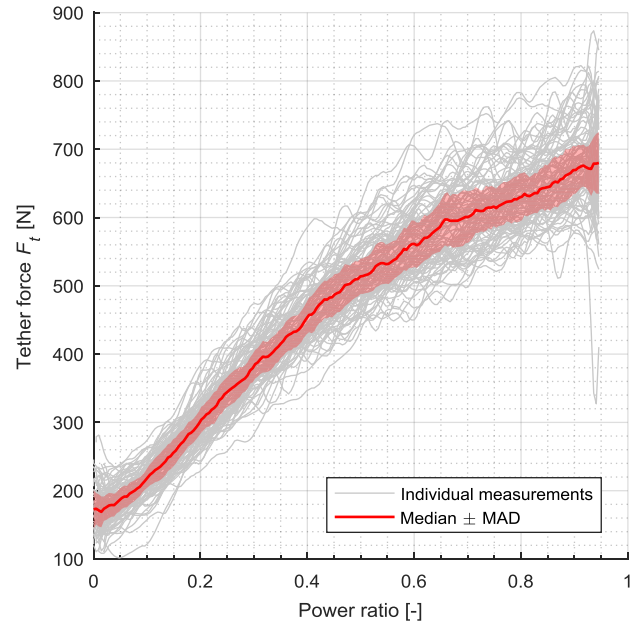


Figure 6.1 Raw and filtered data of the elevation angle θ_w for one dynamic maneuver.

⁵ Acronym for "Point of Interest"

Figure 6.2 Apparent elevation angle ϑ_w .Figure 6.3 Tether force F_t .

6.1.2 Static Maneuvers Processing

The *Pol.m* function is used again to extract the relevant portions of measurements. Both first and last indexes for each constant power ratio are found. Thus, when looking at Figure 4.8, only horizontal steps are considered. Although the power setting is set at the beginning of the straight run, the kite does not react immediately to the input. The same happens at the end of the track, when the fixed power setting is switched off. Therefore, the first and last five seconds of the measurement are cropped in order to make sure that the kite has reached its equilibrium position for the given power ratio. Then, since both signals supplied by the anemometer were occasionally lost, they are corrected by means of the *CorrectData.m* function which brings the lost value back to the mean of the value before and after the glitch. Eventually, the different signals are filtered by a moving average of one second.

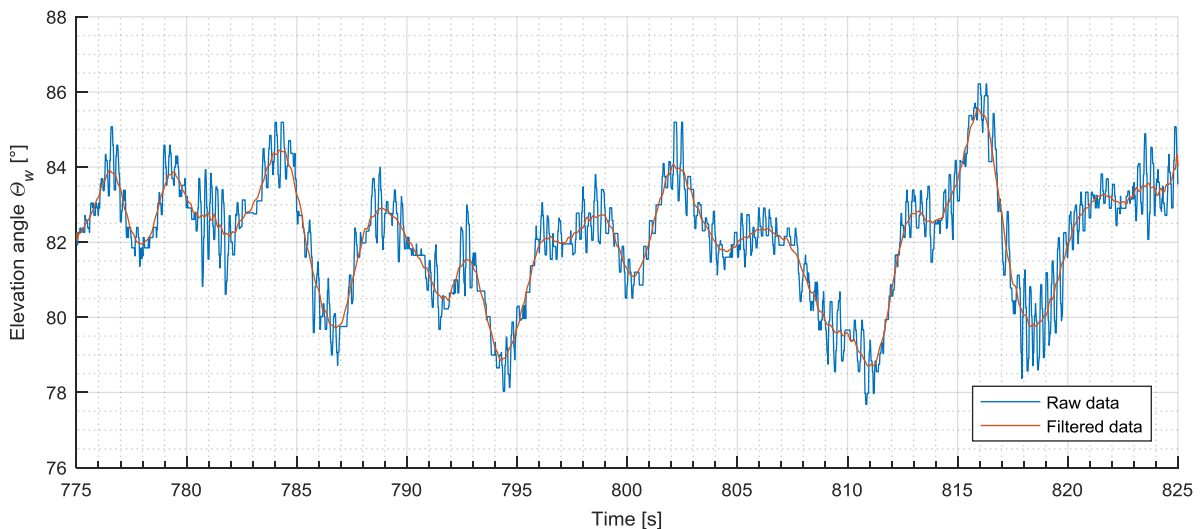
Figure 6.4 Raw and filtered data of the elevation angle ϑ_w for short sequence of static maneuver.

Figure 6.4 shows that the filtered signal follows the general trend of the raw data with a great reduction of the 4 Hz trailer oscillation. Moreover, the size of the moving window of the filter corresponds to less than 1% of a static maneuver size. For these reasons, the one-second moving average filter is justified. This filter is thus applied to all raw signals before to successively compute Equation (4.1) and Equation (4.2) in order to obtain the instantaneous appar-

ent elevation angle ϑ_w for each power ratio step. Then, Equation (6.2) and Equation (6.3) are computed to evaluate the tether force F_t . At this stage, it can already be noticed that although the power ratio is fixed, the kite oscillates within roughly 7° for this case. This is expected to stem from light natural wind at the elevation of the kite, which is unknown. Eventually, filtered samples for one given power ratio step are averaged for each power setting. Figure 6.5 presents the situation for the apparent elevation angle ϑ_w whereas the instantaneous tether force F_t is shown in Figure 6.6 for the Hydra V5 flying at 22 kt.

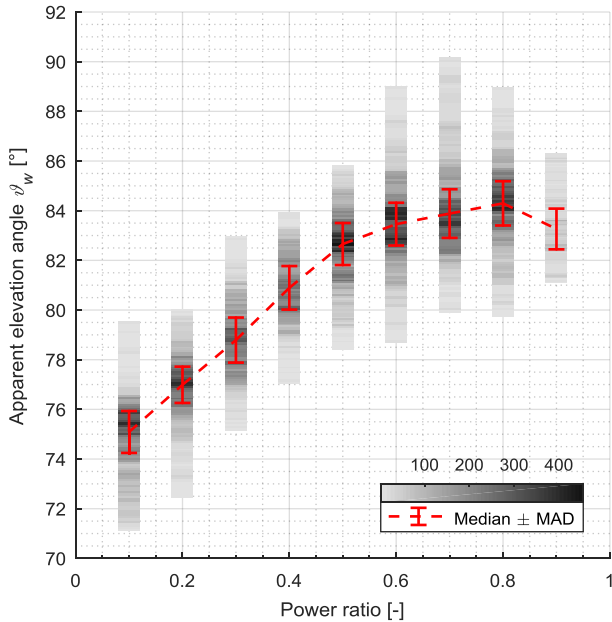


Figure 6.5 Apparent elevation angle ϑ_w of individual samples (grey) and their corresponding median (red) for each power ratio step. The number above the grey scale indicates the number of samples observed.

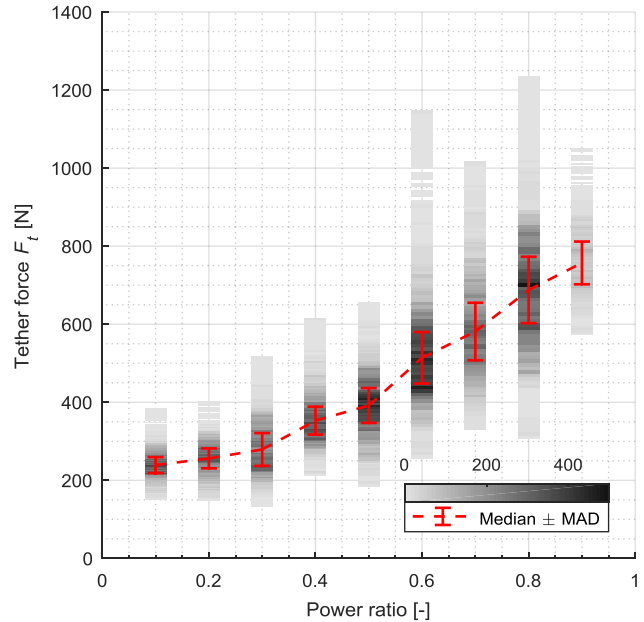


Figure 6.6 Tether force F_t of individual samples (grey) and their corresponding median (red) for each power ratio step. The number above the grey scale indicates the number of samples observed.

6.1.3 Summary

It is important to recall the process flow since the uncertainty propagation evolves accordingly. Once the tether elevation angle ϑ_w and the tether force F_t have been established, both glide ratio and resultant aerodynamic coefficient C_R are computed. Then, they are used to evaluate the lift coefficient C_L which eventually allows to compute the drag coefficient C_D . Therefore, the latter relies on all the foregoing values and their corresponding accuracies whereas the glide ratio for instance is derived from only one single parameter, namely ϑ_w . The Figure 6.7 below summarizes the process flow.

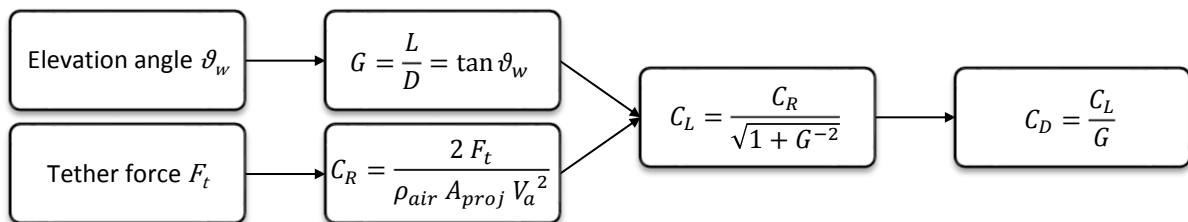


Figure 6.7 Process flow

6.1.4 Uncertainty Propagation

Since some of the measured signals are combined together to compute the aerodynamic coefficients, their corresponding uncertainty has to be estimated as well. Given the new parameter y to be a function of measured variables a, b, c , such as $y = f(a,b,c)$, the following linearized approximation, shown in Equation (6.4) [70], is used to calculate the maximum absolute propagated error Δy originating from all variable absolute uncertainty $\Delta a, \Delta b, \Delta c$. Thus, the propagated error is computed for the glide ratio G in Equation (6.5), for the resultant aerodynamic coefficient C_R in Equation (6.6), for the lift coefficient C_L in Equation (6.7) and for the drag coefficient C_D in Equation (6.8). The derivation is detailed in Annexe 10.5.

As shown in Chapter 4.3.1, each sensor comes with its own accuracy. However, a second uncertainty arises from performing multiple measurements at the same condition. This is given by the median absolute deviation of the median (MAD) as explained in Chapter 6.1. This uncertainty is generally greater than the intrinsic accuracy of the signals. Thus, to be conservative [71], the MAD is chosen as the error Δ for uncertainty propagation.

$$\Delta y = \left| \frac{\partial f}{\partial a} \right| \Delta a + \left| \frac{\partial f}{\partial b} \right| \Delta b + \left| \frac{\partial f}{\partial c} \right| \Delta c \quad (6.4)$$

$$\Delta G = \frac{\Delta \vartheta_w}{\cos^2 \vartheta_w} \quad (6.5)$$

$$\Delta C_R = \frac{2 \Delta F_t}{\rho_{air} A_{ref} V_a^2} + \frac{4 F_t \Delta V_a}{\rho_{air} A_{ref} V_a^3} \quad (6.6)$$

$$\Delta C_L = \frac{\Delta C_R}{\sqrt{1 + G^{-2}}} + \frac{C_R \Delta G}{(1 + G^{-2})^{\frac{3}{2}} G^3} \quad (6.7)$$

$$\Delta C_D = \frac{\Delta C_L}{G} + \frac{C_L \Delta G}{G^2} \quad (6.8)$$

6.2 Dynamic Maneuvers

Once the median and its MAD deviation is computed for the different signals, namely the apparent elevation angle ϑ_w , the tether force F_t and the wind speed V_w , the aerodynamic properties can be determined by applying successively Equation (5.1), Equation (5.2), Equation (2.24), Equation (5.5) and Equation (5.6). This leads to the following Figure 6.8 for the Hydra V5 flying at 22 kt. It can be noticed that these aerodynamic properties are depicted in general by relatively smooth curves. This feature means that the primary signals listed in Table 6.1 provided reliable and unbiased data.

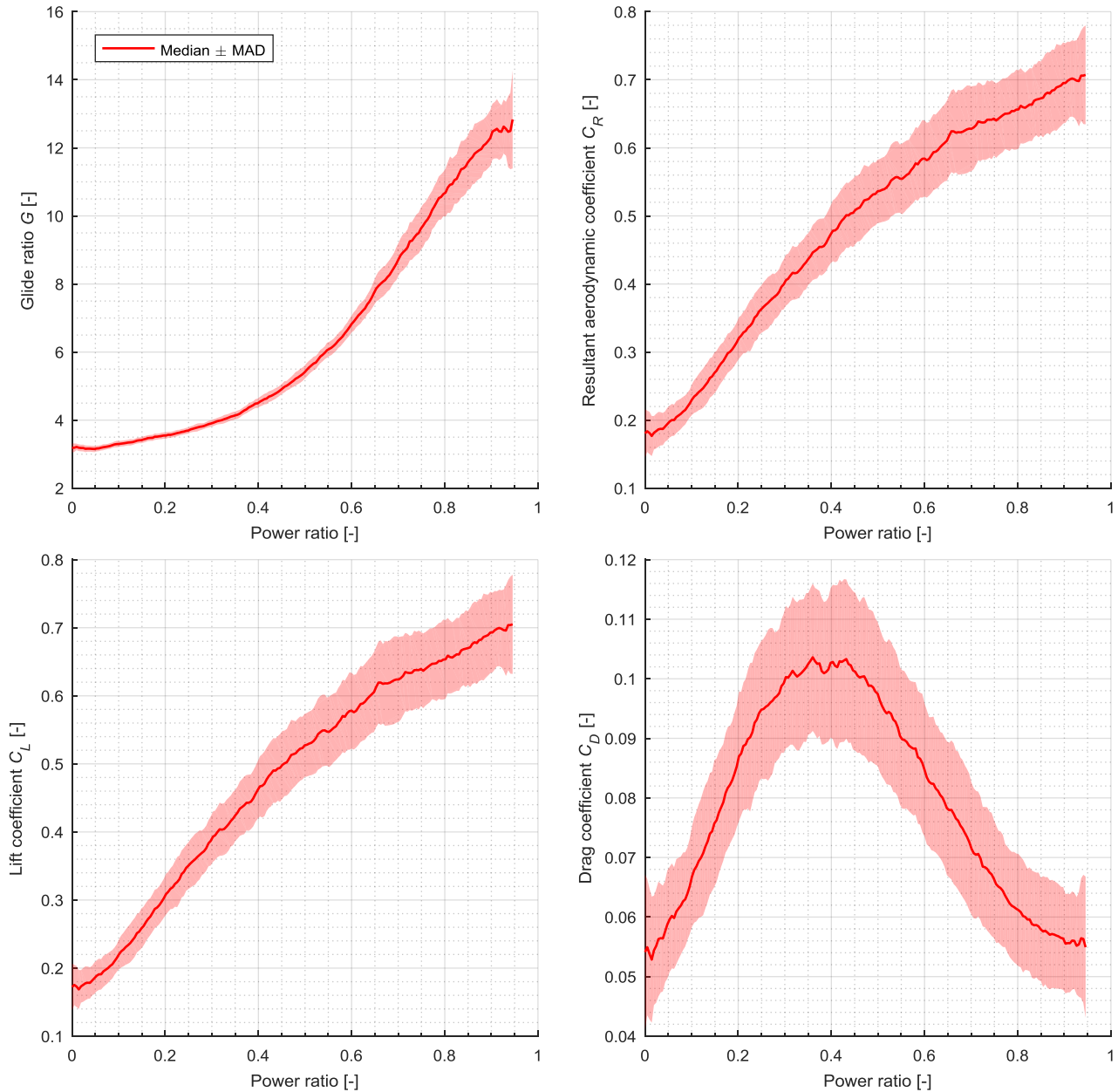


Figure 6.8 Median +/- MAD of the aerodynamic properties computed from dynamic maneuvers for the Hydra V5 flying at 22 kt.

As the power ratio increases, the kite gains height and thus the elevation angle becomes larger. This consequently leads to an increase in the glide ratio (Equation (5.1)). Moreover, since the tether force F_t grows with the $PR\%$, the resultant aerodynamic coefficient C_R also increases, which in turn boosts the lift coefficient C_L as well. It can be seen that MAD progressively develops by successively computing the kite aerodynamic properties according to Figure 6.7. Indeed, the relative error for the drag coefficient is significantly larger than the one from glide ratio as it can be no-

ticed in Figure 6.9. This is explained by the fact that the MAD of the drag coefficient is derived from a sequence of several propagated MAD from previous values whereas the glide ratio, for instance, only depends on one single parameter (c.f. Figure 6.7).

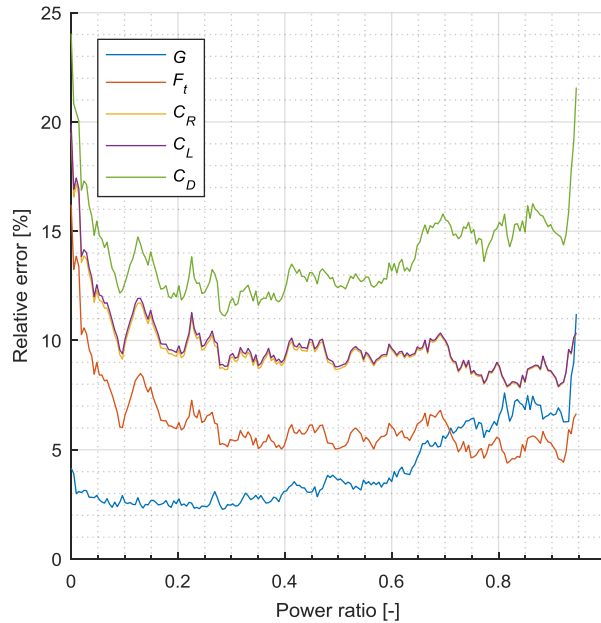


Figure 6.9 Relative error $MAD/median*100$.

6.3 Static Maneuvers

In the same manner as for dynamic maneuvers, the aerodynamic performance is computed hereafter for the Vegas 2015 at 22 kt, for the Mixt at 22 kt and for the Hydra V5 at 22 kt and 29 kt for static maneuvers. Their glide ratio G , aerodynamic coefficient C_R , lift coefficient C_L and drag coefficient C_D are shown in Figure 6.10.

Similarly to dynamic maneuvers, relatively smooth curves can be observed through the aerodynamic properties for the Hydra V5 at both speeds meaning unbiased data. This is however not the case for the Vegas 2015 which presents a sawtooth profile for most of its aerodynamic properties. The Mixt also features this aspect especially for 80% of power ratio. By investigating the primary signals, this characteristic is found to stem from the force measured in the power line F_{PL} as shown in Figure 6.11. This signal has then strong repercussions on the results since it is used to successively compute C_R , C_L and C_D (Figure 6.7). Reasons for such oscillations in F_{PL} may originate from a possible light wind at kite height. Indeed, when driving on one side of the track and facing the light wind, the kite experiences greater air speed and consequently develops stronger tether force compared to the other side of the track with wind in the back. Nevertheless, the speed variation at kite height is unknown since only the velocity at the anemometer is recorded and does not present noticeable fluctuation. In addition, it is worth mentioning for the Mixt that strange flying behaviours were observed by the pilot at a power ratio of 80%. The Mixt had the tendency for back stall. However, for 70% and 90%, the kite was perfectly stable. This is assumed to stem from the bridle configuration which should be improved. Indeed, this kite is still in the prototype phase.

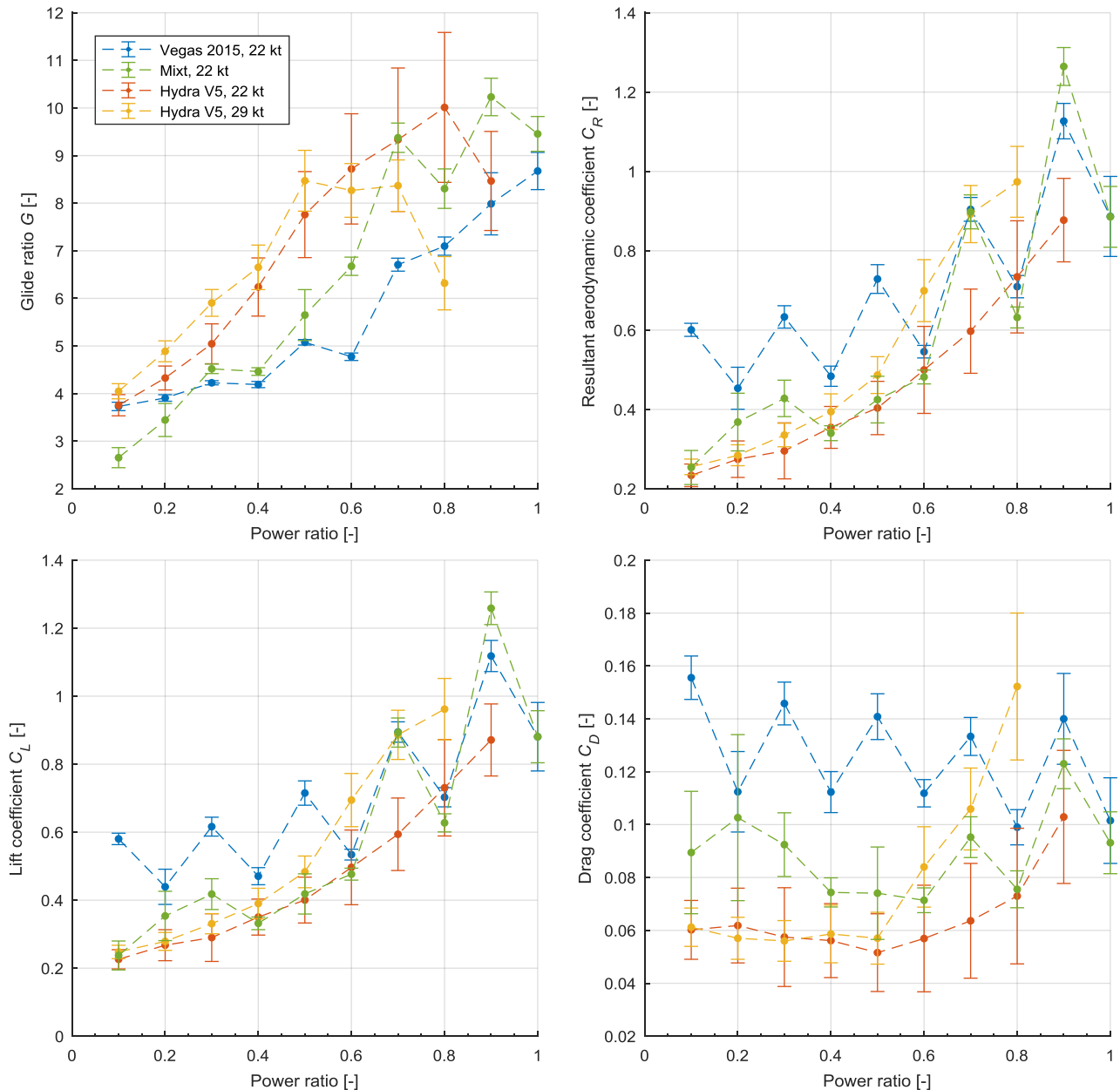


Figure 6.10 Median and MAD of the aerodynamic properties computed from static maneuvers for the Vegas 2015 at 22 kt (blue), for the Mixt at 22 kt (green), for the Hydra V5 at 22 kt (orange) and at 29 kt (yellow).

When comparing the Hydra V5 for both velocities, it can be seen that although coefficients C_R , C_L and C_D should be theoretically independent of the velocity, they generally present greater values for higher speeds. This might be a consequence of the assumption for which the tether force balances the resultant aerodynamic force ($F_t = F_a$). When looking at the glide ratio, its value is greater at 29 kt for the first 50% of power ratio whereas it is inverted for the second 50% of $PR\%$. Thus, the Hydra V5 experiences a higher maximum glide ratio at 22 kt than at 29 kt. Moreover, their respective maximum glide ratios do not occur at the same power ratio. Indeed, the maximum G for the lower wind speed is slightly postponed with respect to power ratio. In addition, the drag coefficient at 22 kt significantly increases passed the 50% of power ratio. A reason for this might come from the fact that several forces acting on the kite are neglected so far, which then biases the final result. For instance, the aerodynamic effects are greater for faster speed and could be a trigger for such effects.

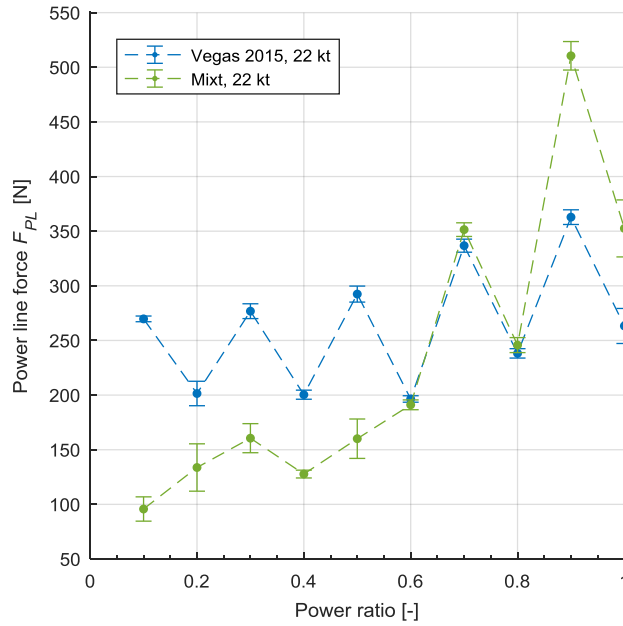


Figure 6.11 Sawtooth profile of the force in the power line.

6.4 Dynamic vs Static Maneuvers

In order to compare both testing procedures, the Hydra V5 flying at 22 kt is considered hereafter. Both apparent elevation angle ϑ_w and aerodynamic efficiency G are presented in Figure 6.12. In addition to the results achieved by the data processing detailed in Chapter 6.1.1, post-processed results from Hummel [48] for the same data set are also illustrated for comparison.

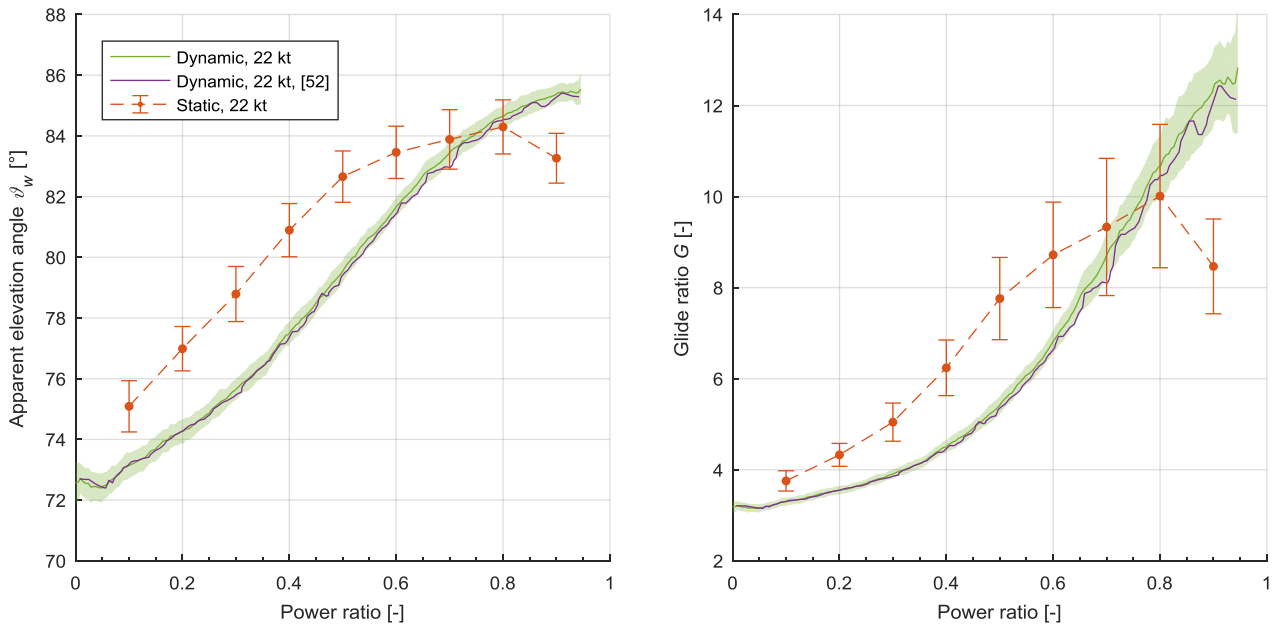


Figure 6.12 ϑ_w and G for the Hydra V5 at 22 kt. Green: median +/- MAD of dynamic maneuvers. Purple: result of dynamic maneuvers obtained by Hummel [48]. Orange: median +/- MAD of static maneuvers.

In this context, it can be said that the close match between current results (green) and result obtained from Hummel (purple) reproduces well the post-processing methodology developed for dynamic maneuvers in Chapter 6.1.1.

By observing the elevation angle ϑ_w of Figure 6.12, one can deduce that the kite generally reaches higher altitudes when flown with static maneuvers compared to dynamic ones. However, passed a certain power ratio, this tendency is inverted and the elevation angle becomes larger for dynamic maneuvers. One possible reason for this could be that at the beginning of the dynamic maneuvers, the kite does not respond immediately to the power input. Indeed, after one second, the power ratio is already at 25% of its maximum value, which might be a too large variation rate for the kite to be taken in. This is even more emphasised by the fact that the $PR\%$ is still decreasing just before the start of the dynamic maneuver. Indeed, there is no pause between the depower and power phases as shown in Figure 4.7. Therefore, the kite might still be losing height as the dynamic maneuver starts, as suggested on the left-hand side of Figure 6.12 for $PR\% < 10\%$. Consequently, it cannot be asserted that the kite is at its equilibrium position at the beginning of the maneuver, neither during it. Nevertheless, as soon as the kite responds to the power input, it gains speed and, due to its inertia, tends to overshoot its equilibrium position. This translates into a continuous increase of the glide ratio for dynamic maneuvers as it can be seen on the right-hand side of Figure 6.12. On the contrary, the glide ratio for static maneuvers reaches its maximum and then slightly drops for a power ratio of 90%.

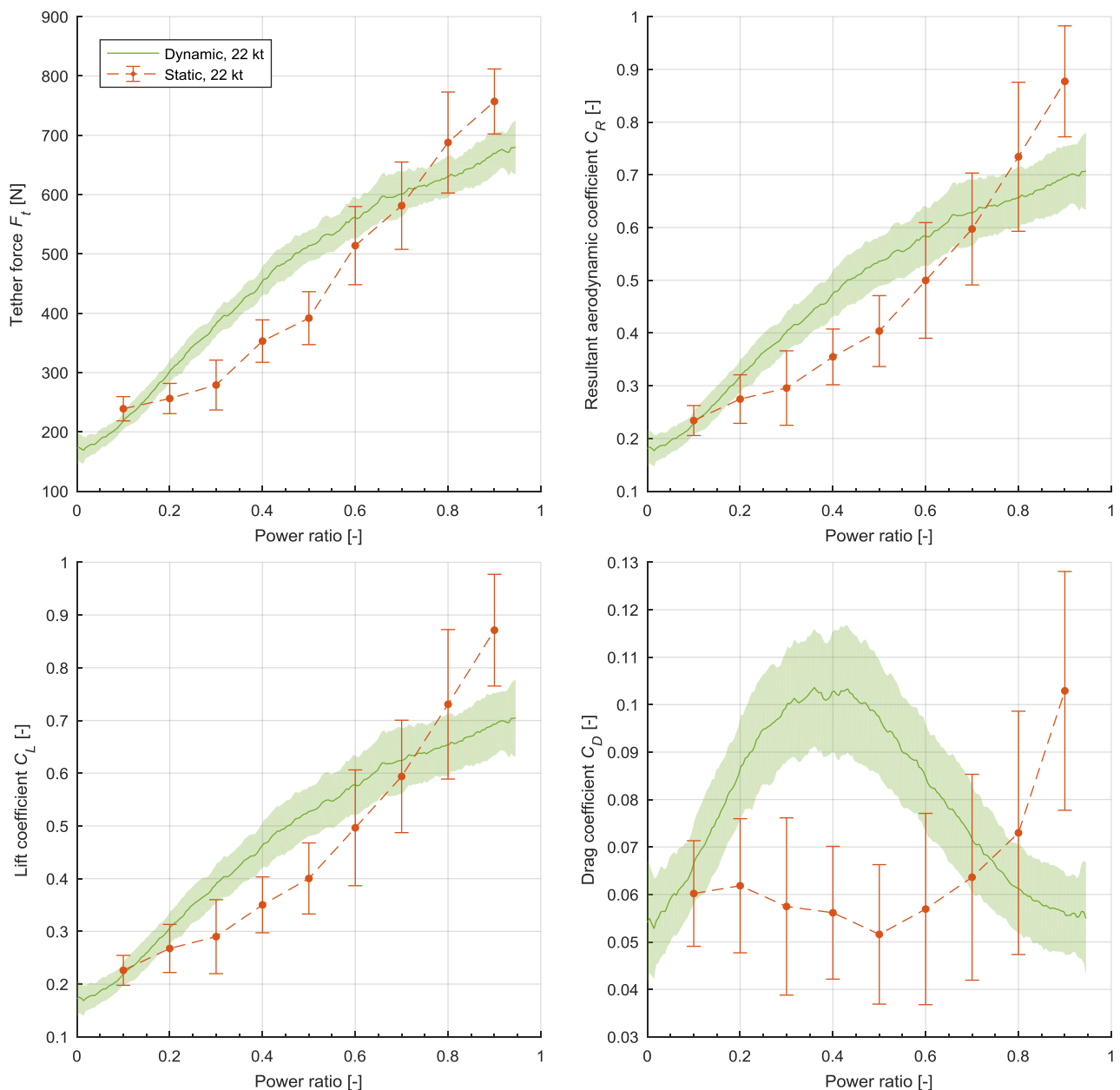


Figure 6.13 Median and MAD of the aerodynamic properties computed for the Hydra V5 at 22 kt. Green: dynamic maneuvers. Orange: static maneuvers.

Figure 6.13 shows the tether force and the aerodynamic coefficients for both testing procedures. It can be noticed that both methodologies lead to significant distinct behaviours for all parameters. Indeed, a concave shape can be distinguished from dynamic maneuvers whereas static maneuvers exhibit convex evolution of the aerodynamic properties. It is worth mentioning that both dynamic and static curves always cross for the same power ratios, namely 10% and 75%. C_R , C_L and C_D directly follow the trend given by the tether force F_t since they are successively derived from it.

The concave feature of the tether force for dynamic maneuver could be explained by the same previous reasons: fast change between depower and power phases and slow kite response. Figure 6.14 presents the power ratio and the apparent elevation angle for one given dynamic maneuver. Yellow shading illustrates the powering phase. As the $PR\%$ returns to its initial value of 0%, the elevation angle decreases meaning that the kite loses altitude. However, at the start of the dynamic powering maneuver, the kite continues to drop due to its inertia and then stays around $74-75^\circ$ for roughly one second. Within this period, the tether force rapidly develops since the $PR\%$ increases of 25% while the kite does not noticeably move. As soon as the kite responds to the power input and gains altitude, the tether force increases slower.

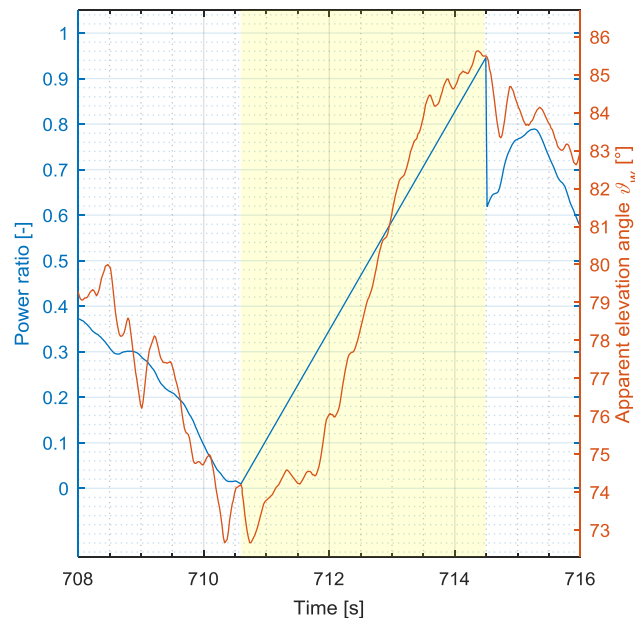


Figure 6.14 Power ratio and apparent elevation angle. Yellow shading: dynamic powering maneuver.

Since static maneuvers assume that the kite reaches its equilibrium position for each power step, one can suggest by comparing both methodologies that the kite strongly features a dynamic behaviour when dynamic maneuvers are performed. Since the kite does not react immediately to the power input, its apparent elevation angle is underestimated whereas its aerodynamic coefficients are overestimated during the first 75% of power ratio. Passed this point, these characteristics are inverted for the last 25% of power ratio, which means that the kite overshoots its equilibrium position.

For these reasons, static maneuvers are thought to provide more realistic and reliable results than dynamic maneuvers. However, several aspects, such as weight and tether aerodynamic, are still neglected at this point. Therefore, the following Chapter 6.5 includes these corrections into the results obtained for static maneuvers.

6.5 Mass and Tether Effects on Aerodynamic Performances

Both kite and tether mass as well as drag and lift of the tether play a role in the force equilibrium of the kite and have therefore to be considered when establishing its performance coefficients. First, the masses are taken into account by combining Equation (5.9) and Equation (5.10) for the tether weight with Equation (5.4) of the kite weight. Then, the aerodynamic effects of the tether are included in the force equilibrium through Equation (5.14) and Equation (5.15). The influence of these contributions is presented in Figure 6.16 for the Hydra V5 flown by static maneuvers at 22 kt. Note that solid lines refer to the left axis which denotes values of the given properties whereas discontinuous lines are associated to the right axis which designates the individual contribution of each effect, namely kite mass (ΔM_k , blue), tether mass (ΔM_t , blue), tether drag (ΔD_t , yellow) and tether lift (ΔL_t , yellow). The uncorrected features obtained from the 2D point model are shown as a reference basis with their median (dot) \pm MAD (error bar) and their corresponding 3rd order polynomial fit in orange. The global mass effect is illustrated by the solid blue line while the solid yellow line indicates the global aerodynamic effect of the tether. The final global correction is illustrated with green colour.

In order to have a better interpretation of the graphs, the following Figure 6.15 helps in indicating the corresponding line styles and colours as well as reference axis. On the one hand, the solid blue line is composed by the uncorrected value and the two mass effects. On the other hand, the solid yellow line is constituted by the uncorrected data and the two aerodynamic effects. They merge together to obtain the global correction shown with green colour.

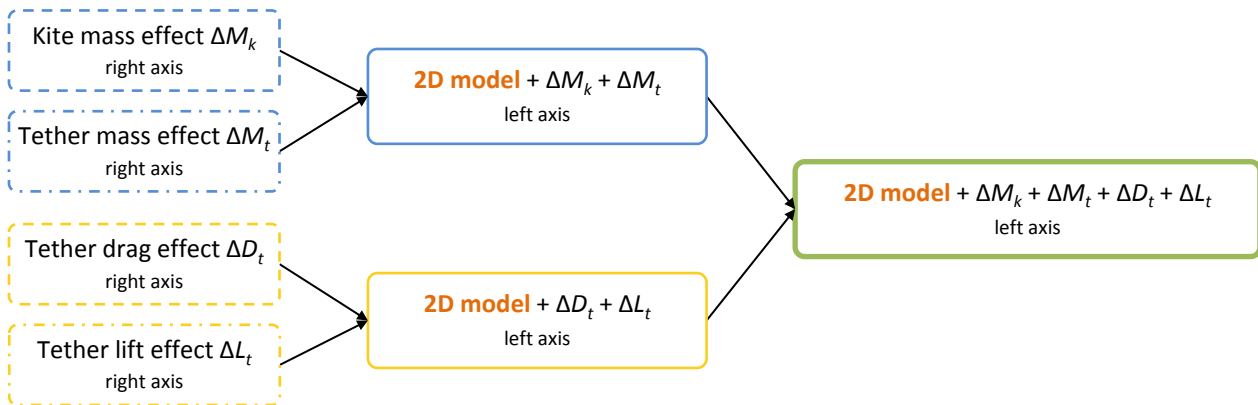


Figure 6.15 Structure and interpretation of Figure 6.16.

Equations of both corrected C_L and C_D for the different effects are shown in Annexe 10.6. Once both lift and drag coefficients are computed, C_R and G are established through Equation (2.27) and Equation (2.28) respectively. Details of individual correction of mass effect and tether aerodynamic effect are presented for completeness in Annexe 10.7 and Annexe 10.8 respectively.

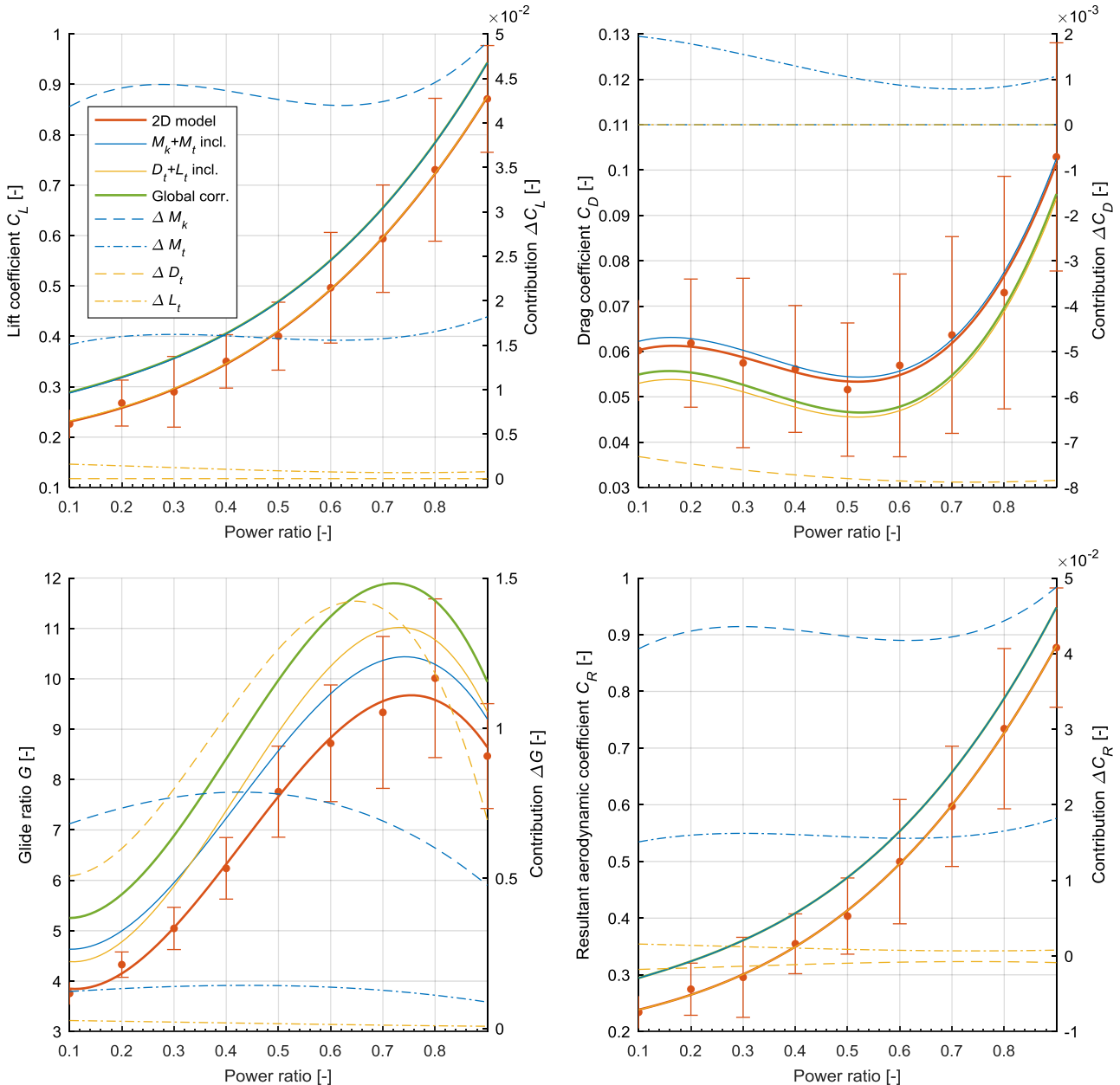


Figure 6.16 Kite and tether weight, drag and lift tether effects on aerodynamic performances for the Hydra V5 at 22 kt.

Left axis: effective value. Solid orange: no correction. Solid blue: mass incl.. Solid yellow: tether aerodynamic incl.. Solid green: global correction. Right axis: contribution of kite mass (dashed blue), tether mass (dash-dotted blue), tether drag (dashed yellow), tether lift (dash-dotted yellow).

By looking at Figure 6.16, several aspects can be identified. For instance, the top left figure indicates that the main contributions (right axis) in altering the kite lift coefficient C_L come primarily from the kite mass (+0.044) and secondly from the tether mass (+0.016). On the contrary, the tether lift does not play a noticeable role on C_L whereas the tether drag does not have any effect on it. Therefore, the solid yellow line (tether aerodynamic) stays superimposed to the uncorrected solid orange line while the solid blue line (combined mass effects) is overlapping the solid green line (global correction). Eventually, the global correction adjusts the kite lift coefficient C_L by an overall increase of 0.061 point.

By inspecting the kite drag coefficient C_D on the top right of Figure 6.16, it can firstly be noticed that both kite mass and tether lift do not have any influence on it. Then, although opposite, the major changes in C_D stem from the tether mass (+0.0012) and the tether drag (-0.0077). Therefore, the combined influence of all these effects leads to a global decrease of 0.0065 point of C_D compared to the uncorrected one. One should notice that solid blue, yellow and green

correction lines fall within the \pm MAD range of the uncorrected data. Corrected aerodynamic properties have therefore to be considered with caution.

Eventually, by looking at the resultant aerodynamic coefficient C_R on the bottom right graph of Figure 6.16, it can be noticed that the main changes are due to the mass effects of both kite (+0.043) and tether (+0.016). On the contrary, the aerodynamic effects of the tether do not have significant influence on C_R . The yellow line illustrating their combined aerodynamic effects does not move away from the uncorrected one. Thus, the global correction line is essentially composed by both kite and tether mass effects, as it is shown by the superimposition of the blue (combined mass effects) and green (global correction) lines.

Finally, both lift and drag coefficients combine together to derive the glide ratio (Equation (2.28)) shown on the bottom left graph of Figure 6.16. When examining the individual contribution (right axis), it can be seen that each effect plays a very different role. On the one hand, the tether lift and tether mass have relatively small influences on the glide ratio (+0.02 and +0.12 respectively). On the other hand, the kite mass and tether drag significantly affect the aerodynamic efficiency G by on average +0.70 and +0.99 respectively. As a result, this leads to a global increase of G by +29%. Moreover, it is worth mentioning that while the individual contributions of the kite mass, tether mass and tether lift are relatively constant with the power ratio, the tether drag effect significantly varies with $PR\%$. Indeed, it affects the kite glide ratio with an increase varying from +0.52 to more than +1.4. Eventually, the maximum glide ratio is not only slightly shifted to the left of the graph, but it is also improved by +2.2 when taking all these effects into account. This increase is especially noticeable since the final corrected line is no more enclosed by the \pm MAD range.

It is however important to note that the contribution due to the tether drag is relatively sensible to its parameters of Equation (5.14), especially to the tether diameter d_t . Figure 6.17 shows the variation in the glide ratio ΔG due to the tether drag effect ΔD_t for different line diameters from 1 to 3 mm. In the current setup, the line diameter is 1.5 mm. But a discrepancy of 0.5 mm on such a diameter could already lead to a change of ± 0.5 in the lift-over-drag ratio. In contrast, modifying the kite mass from the current 4.29 kg to an imaginary 1 kg would not even alter the variation in glide ratio by -0.5.

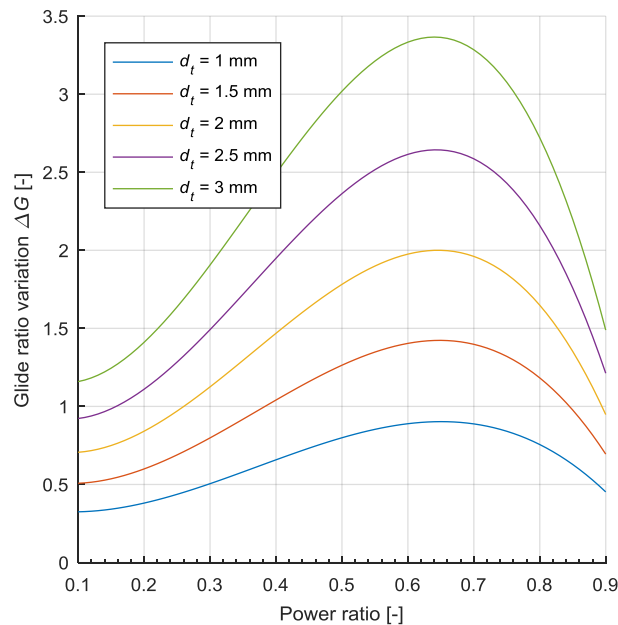


Figure 6.17 Sensitivity analysis of the tether diameter d_t on the glide ratio variation ΔG due to tether drag effect ΔD_t .

6.6 Tether Sag Effect

Solving the differential equation system given by Equation (5.21) to Equation (5.23) allows to evaluate the sag of the tether. In this context, the worst-case scenario is examined. This means that the profile of the 24 m long lines is investigated by considering the Hydra V5 flying at 22 kt via static maneuvers through a hypothetical natural front wind of 2 m/s recorded at 3 m above ground. Indeed, an underestimation of the wind speed can lead to a misestimation of the tether sag affecting the derivation of the aerodynamic coefficients. Figure 6.18 depicts the sag of the tether for two extreme power ratios, namely 10% (blue) and 90% (orange). The dashed line represents the straight tether. It can be noticed that a larger deviation occurs for a lower power ratio. This is reinforced by looking at Table 6.2. Indeed, the deviation becomes more significant as the power ratio decreases. In addition, it appears that the tether force at the ground $F_{t,g}$ is smaller than the tether tension at the kite $F_{t,k}$. Indeed, roughly 15 N are dissipated by the weight and the aerodynamic effects of the tether. The elevation angle at the kite becomes on average 1° smaller when the extra natural wind is removed.

Table 6.2 Tether sag effect

Power Ratio	β_g	β_k	$\Delta\beta$	$F_{t,g}$	$F_{t,k}$	ΔF_t
%	[°]	[°]	[°]	[N]	[N]	[N]
10	75.09	81.06	5.97	238.95	253.49	14.54
20	76.99	82.16	5.18	256.22	270.98	14.76
30	78.79	83.55	4.76	278.99	293.90	14.91
40	80.89	84.78	3.89	353.01	368.07	15.06
50	82.66	86.06	3.40	391.69	406.90	15.21
60	83.46	86.17	2.72	513.97	529.20	15.23
70	83.88	86.18	2.30	581.33	596.59	15.26
80	84.30	86.18	1.89	687.83	703.11	15.29
90	83.26	84.89	1.63	757.03	772.25	15.22

The variation in tether force must be considered when computing the aerodynamic coefficients of the kite. Indeed, this change affects the force equilibrium at the kite. The aerodynamic coefficients computed from the tether sag model are compared, in Figure 6.19, against the ones previously obtained in Chapter 6.5. The results computed from the simple 2D model and from the model which lumps all the tether forces to the kite are shown with solid orange and solid green lines respectively. The aerodynamic properties stemming from the tether sag model are exposed with solid blue lines for an extra natural wind of 2 m/s and with dashed green lines for neglected natural wind. The reason for using the green colour twice but with different line styles comes from the fact that, if the lumped model was ideal, it should therefore match the tether sag model.

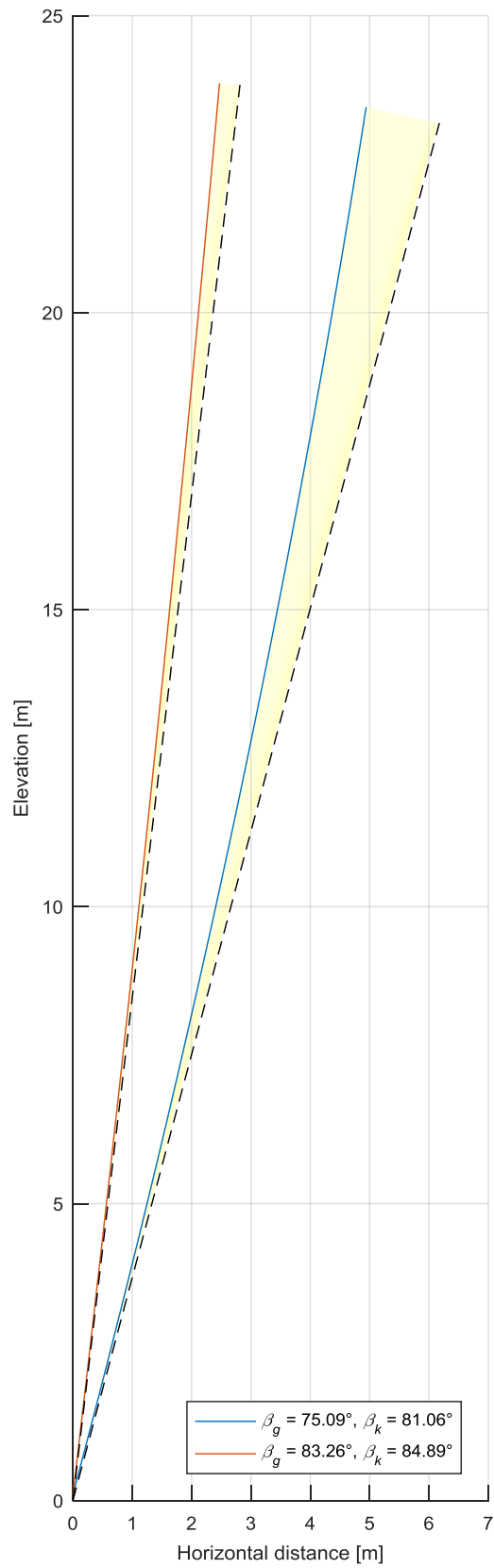


Figure 6.18 Tether sag for power ratio of 10% (blue) and 90% (orange), in comparison to straight tether (dashed black).

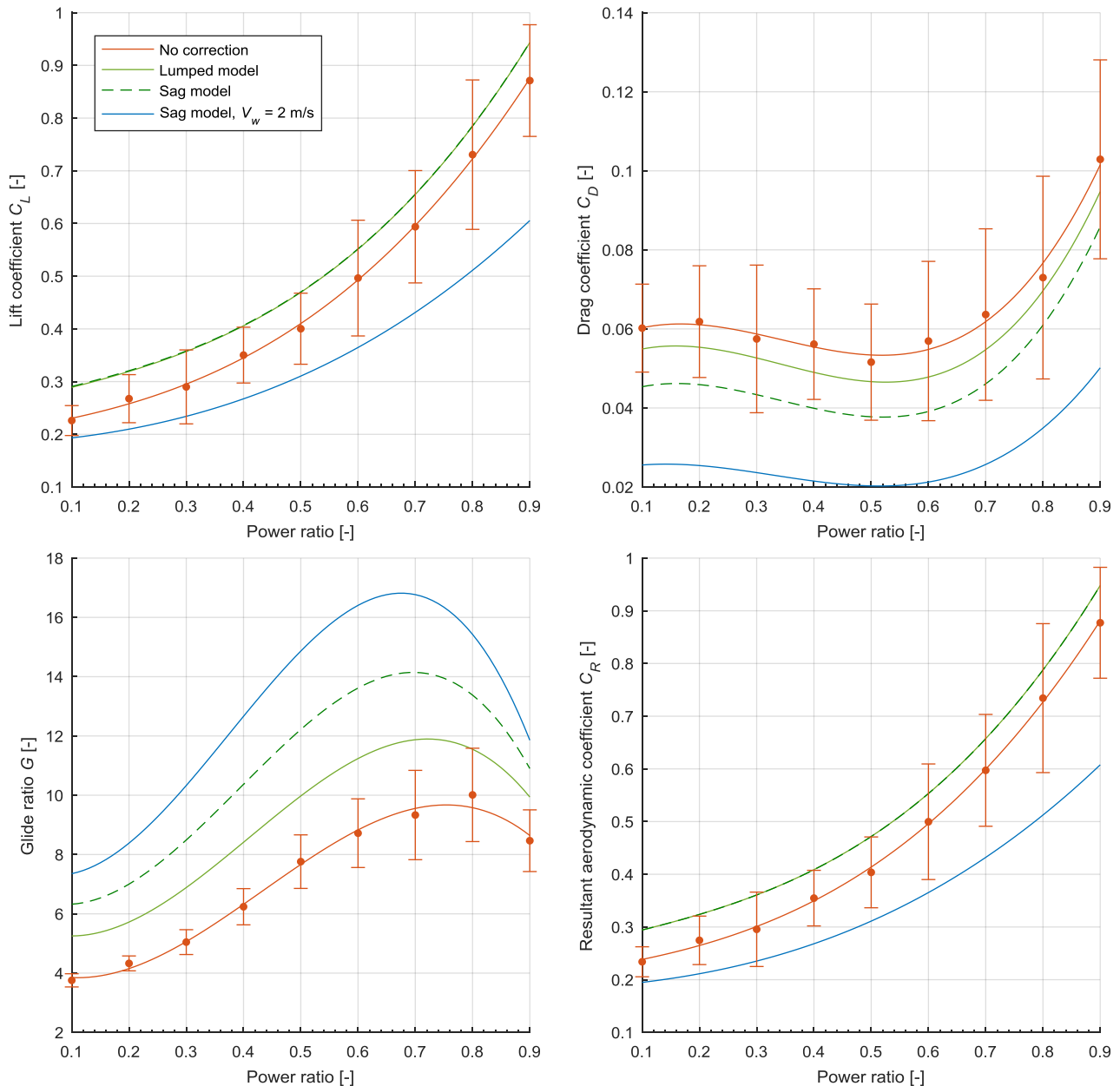


Figure 6.19 Aerodynamic performances for the Hydra V5 at 22 kt obtained from different refinement models. Solid orange: no correction, median \pm MAD, $V_w = 0$ m/s. Solid green: global correction from lumped forces (Chap 6.5), $V_w = 0$ m/s. Dashed green: correction from sag model, $V_w = 0$ m/s. Solid blue: correction from sag model, $V_w = 2$ m/s.

By examining the top left graph of Figure 6.19, it can be noticed that both lumped model and tether sag model lead to similar lift coefficients: their curves coincide perfectly. This means that the complex tether sag model does not necessarily provide better value for C_L compared to the simpler lumped model. Nevertheless, when an extra 2 m/s of natural wind is added to simulate the worst-case scenario, the lift coefficient is significantly affected and notably drops.

This same feature is found in the top right graph for the drag coefficient as well. Indeed, there is an average reduction of -0.037 in C_D due to the extra natural wind of 2 m/s. For the case where the natural wind is neglected, the drag curve derived from the lumped model (solid green) does not match the one from the tether sag model (dashed green) as it was previously for the lift coefficient. The latter is on average improved by -0.016 compared to uncorrected drag coefficient.

This discrepancy between both tether sag and lumped models is propagated through the glide ratio as presented on the bottom left graph of Figure 6.19. Indeed, since the drag coefficient obtained from the tether sag model is actually

lower, its corresponding glide ratio consequently becomes greater than the one from the lumped model. Thus, L/D is improved by +3.64 on average compared to the uncorrected one and reaches a maximum of 14 for a power ratio of 70%. This significant increase is supported by the fact that the tether elevation angle at the kite β_k is greater than the tether elevation measured at the ground β_g . Although this change seems to be relatively small, its effect on the glide ratio can be significant, especially for high elevation angles, because of the tangent relationship. Figure 6.20 illustrates the tangent function for an angle ranging from 75 to 88°. It is shown that an increase of 3.4° in the elevation angle β (which corresponds to the case of 50% power ratio in Table 6.2) leads to a gain of 6.76 in the glide ratio. When the natural wind of 2 m/s is considered, the glide ratio is boosted even more, up to almost 17. Although the lift coefficient is diminished, this increase is explained by the fact that the drag coefficient is significantly reduced.

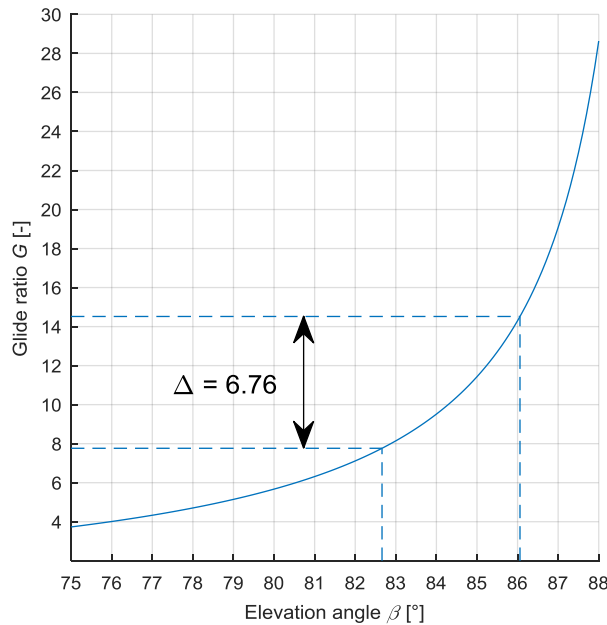


Figure 6.20 Tangent relationship between elevation angle β and glide ratio G . Dashed lines shows the difference in G for $\beta = 82.66^\circ$ and $\beta = 86.06^\circ$ which correspond to the angles for 50% power ratio (Table 6.2).

Finally, the resultant aerodynamic coefficient C_R is presented on the bottom right graph of Figure 6.19. Since the drag coefficient is roughly one order of magnitude lower than the lift coefficient, the resultant aerodynamic coefficient C_R is mainly governed by C_L . Therefore, the curve for C_R greatly follows the same trend as the one for the lift coefficient. When the natural wind is neglected, the curve obtained by the tether sag model matches the one from the lumped model. If the natural wind is considered, the resultant aerodynamic significantly drops by an average of -0.126. The major reduction occurs for high power ratio with devaluation down to -0.273.

6.7 Angle of Attack - Power Ratio Relationship

In order to relate the aerodynamic curves to the angle of attack instead of the power ratio, the corresponding conversion needs to be established. As a first step, the power ratio angle ε is investigated with respect to the power ratio $PR\%$. Figure 6.21 shows the power ratio angle ε obtained for multiple power positions throughout the 36 cm of power range (blue). A second order polynomial curve (orange) is fitted through these measurement points in order to extrapolate the relationship for the power range of 50 cm. Thus, the 0 cm of power position corresponds to 100% of power ratio whereas the 50 cm coincides to 0% for the line used with the TETA setup. Although not linear, it appears that the power ratio angle ε gradually increases as the power ratio decreases (power position increases). Moving the handle bar from 0 to 100% of power ratio leads to an angular variation of roughly 12°. The non-linearity comes from the deformation of the kite and the change in bridle configuration for different power settings.

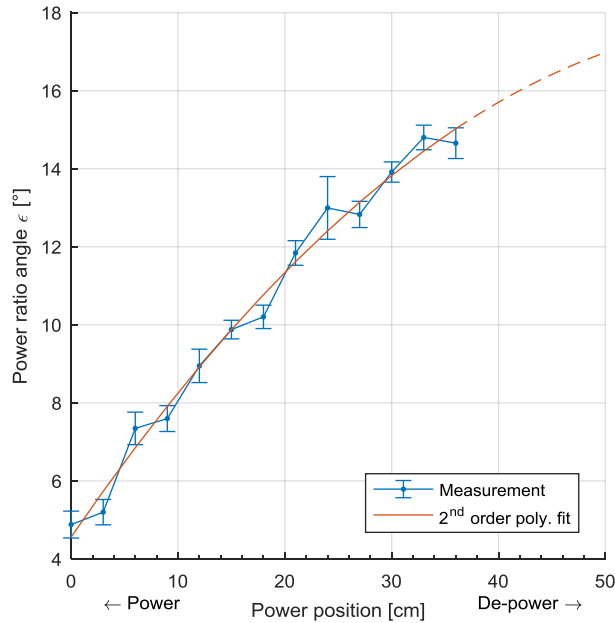


Figure 6.21 Power ratio angle ϵ with respect to the power position (alternatively power ratio). Blue: measurement with 36 cm power range lines. Orange: extrapolation for 50 cm power range lines.

By knowing the power ratio angle ϵ , Equation (5.28) and Equation (5.29) are computed to establish the pitch angle for each power ratio, as shown in yellow in Figure 6.22. For these equations, the elevation angle at the ground β_g is firstly adopted to have a comparison with Costa [47]. It is represented by dashed lines. Then, to take into account of the sag of the tether, the elevation angle at the kite β_k is considered. Its corresponding pitch angle is illustrated with solid lines. Eventually, both β_g and β_k are corrected by including the small angle ζ at the handle bar junction (green). Thus, the latter relationship is expected to be the most representative of the reality and is considered by default unless otherwise specified. Finally, in order to assess the effect of the power ratio angle ϵ on the pitch angle ψ , the blue lines are established by neglecting ϵ in the calculation.

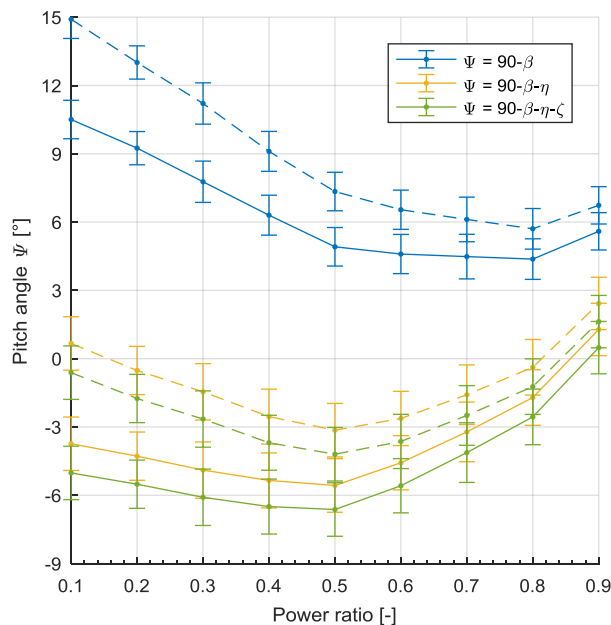


Figure 6.22 Pitch angle ψ versus the power ratio, evaluated with β_g (dashed line) and β_k (solid line).

The first thing to notice when examining yellow and green lines on Figure 6.22 is the fact that the same pitch angle ψ can be obtained for two distinct power ratios. This convex behaviour stems firstly from the fact that both elevation

angle β and power ratio angle ε evolve in an opposite way with roughly the same amplitude and secondly because the elevation angle presents a concave shape with respect to the power ratio (Figure 6.5).

Considering the elevation angle at the kite β_k instead of the one at the ground β_g shifts the pitch angle ψ to a lower value. Since the sag of the tether is more important for low power ratios, the decrease in pitch angle due to sagging is more notable for these low power ratios. In addition, it can be noticed that the angle ζ at the junction of the handle bar does not have a significant effect on the pitch angle. Indeed, the latter is slightly decreased. However, on the other side, the effect of the power ratio angle ε is not negligible. Indeed, it significantly lowers the pitch angle ψ , namely the angle of attack in this case, down to negative values.

Expressing the aerodynamic properties obtained in Chapter 6.6 with respect to the pitch angles derived in Figure 6.22 leads the following Figure 6.23. The same colour code is adopted. The different derivations of the pitch angle do not influence on the magnitude of the aerodynamic properties but rather shift the curves on the left or on the right.

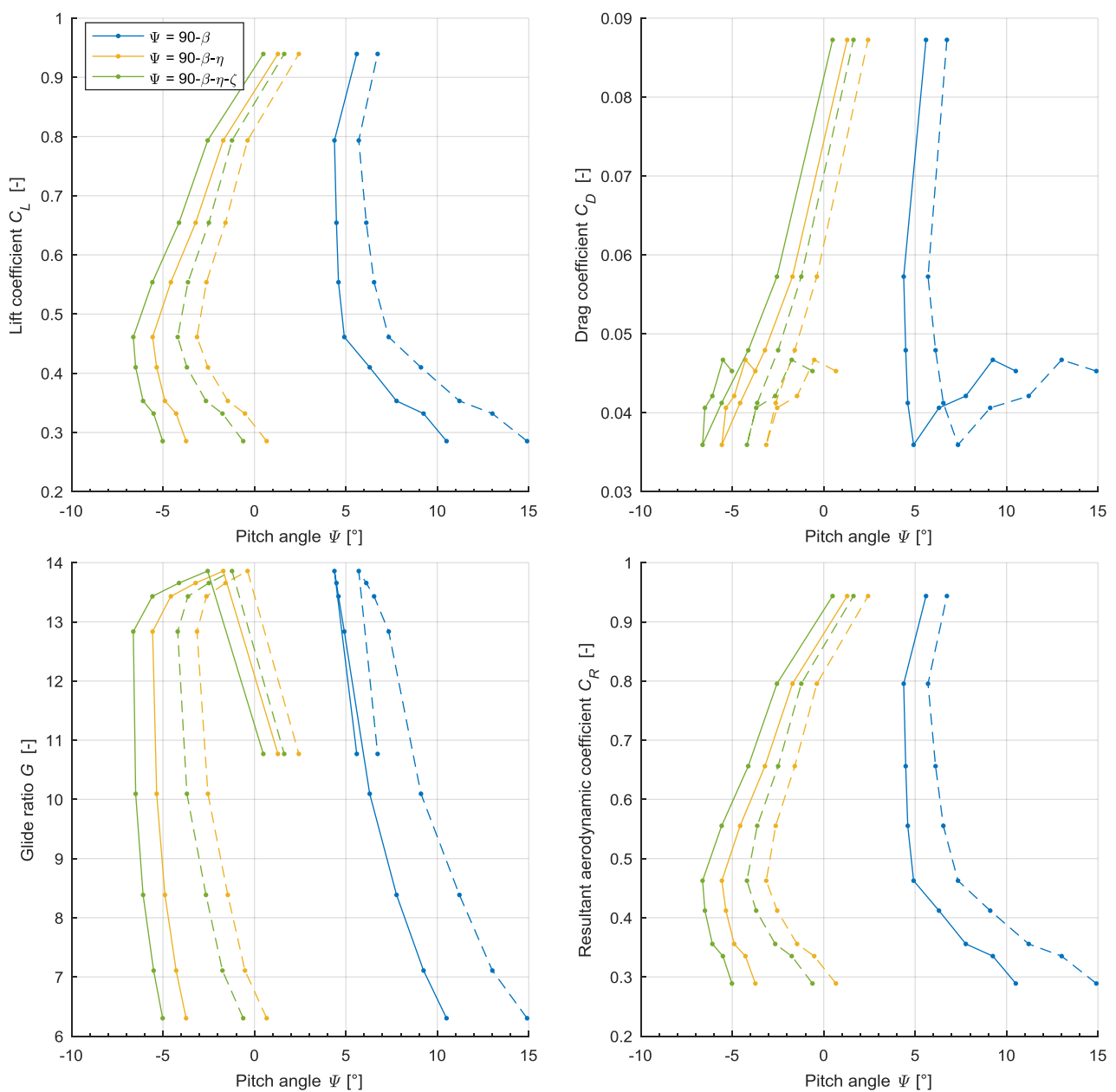


Figure 6.23 Aerodynamic properties for the Hydra V5 at 22 kt obtained from the tether sag model (Chapter 6.6) and expressed with respect to the different pitch angle derivations.

Dashed lines considered the elevation angle at the ground β_g whereas solid lines the elevation angle at the kite β_k .

Because of the convex relationship between the pitch angle ψ and the power ratio, the aerodynamic properties presented in Figure 6.23 show strange trends. For instance, for each aerodynamic property, two distinct quantities can be obtained at the same pitch angle. It is known from conventional wings [37] that the lift coefficient should evolve linearly between 0 to 10°. This feature does not appear when examining the top left graph of Figure 6.23. For those reasons, the $PR\%$ - AoA relationship and therefore the aerodynamic properties presented in Figure 6.23 are advised to be taken with care.

One can imagine the hypothetical situation for which the power ratio angle ε would exhibit a more vertical profile (c.f. Figure 6.22), meaning a larger ε range for the same power range. This would lead the pitch angle to change its trend and to have constant increase with the power ratio. Although the pitch angle would have unrealistic negative values, such a feature would have an influence on the shape of the aerodynamic properties curves of Figure 6.23 and would make them more realistic. As a hypothetical illustration, Figure 10.6 in Annexe 10.9 presents C_L , C_D , L/D and C_R with respect to the pitch angle obtained by considering the power ratio angle ε to be twice its actual value. From this, it can be suggested that the main reason for such convex relationship between pitch angle and power ratio originates from an improper relationship between the power ratio and its corresponding angle ε .

As an alternative corroboration, the calculation process can be reversed to establish the pitch angle with respect to power ratio by assuming typical polar curves. In this context, the aerodynamic coefficients used by Fechner [72] for his kite dynamic model are adopted and shown in Figure 6.24. From these, the theoretical pitch angle is established and exposed in blue in Figure 6.25 as well as the pitch angle assessed experimentally (green). It can be seen from this comparison that both curves do not match at all. The theoretical pitch angle continuously increases with $PR\%$ through positive values whereas the pitch angle established experimentally presents a convex profile with negative values. From this discrepancy, the incorrectness of the $PR\%$ - ψ conversion is reinforced and would require more investigation.

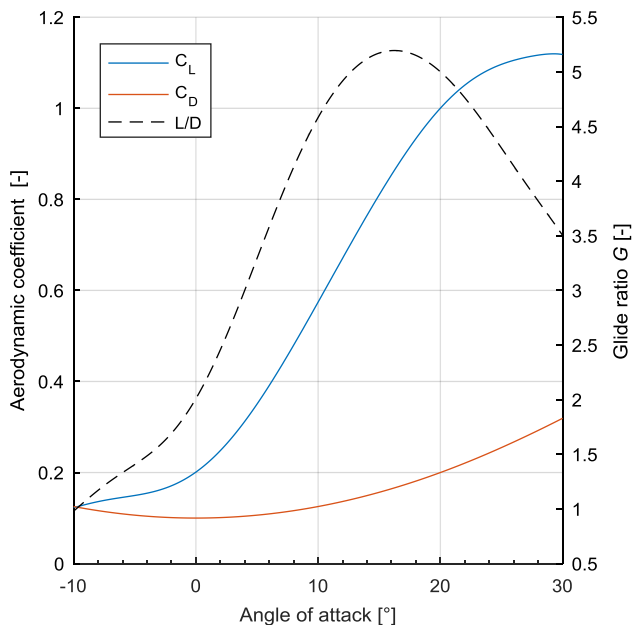


Figure 6.24 Aerodynamic properties assumed by Fechner [72] and adopted for the reverse calculation process.

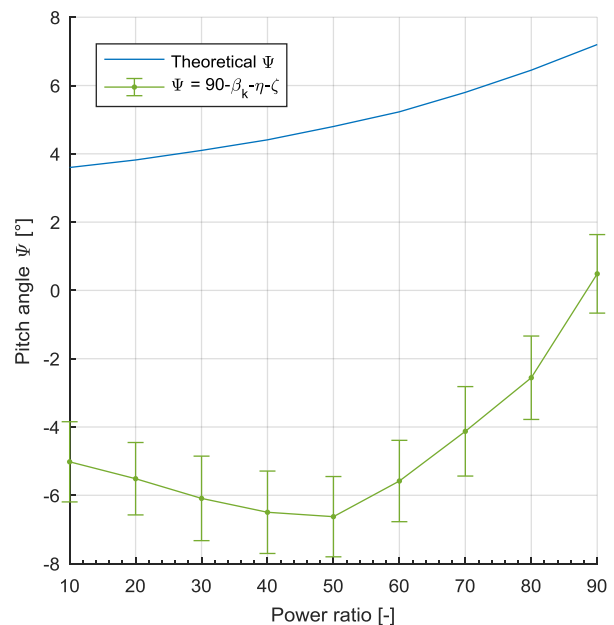


Figure 6.25 Theoretical (blue) and experimental (green) pitch angle with respect to power ratio.

Although it is common for cambered wing (such as the Hydra V5) to generate lift when operating at low negative angle of attack (typically -3° , [37]), the computed AoA presents larger negative values, down to -6.6° for power ratio of 50% (green line on Figure 6.25). It was initially expected that the angle of attack should be comparable to the one derived by Costa [47] since the definition of the angle of attack, the kite shape and the testing procedure of both experiments were rather similar. For his investigation, Costa recorded an angle of attack varying from -2° to 10° . However,

er, it is important to note that this has been achieved by investigating only one single power setting. In order words, his AoA varies within 12° even though the power ratio, consequently the power ratio angle ε , are constant.

Being aware of this oscillation despite a fixed power ratio, the present examination is brought one step backward and investigates the instantaneous flight state (instead of the average one) to see if similar fluctuations are observed along the experiment. Figure 6.26 presents the pitch angle ψ , derived by including the handle bar angle ζ , with respect to the elevation angle at the kite β_k for each power ratio. The black dots indicate the median of the instantaneous measurements, which correspond to the green line of Figure 6.25. Figure 6.27 illustrates the instantaneous lift coefficient for 10% of power ratio with respect to the pitch angle ψ .

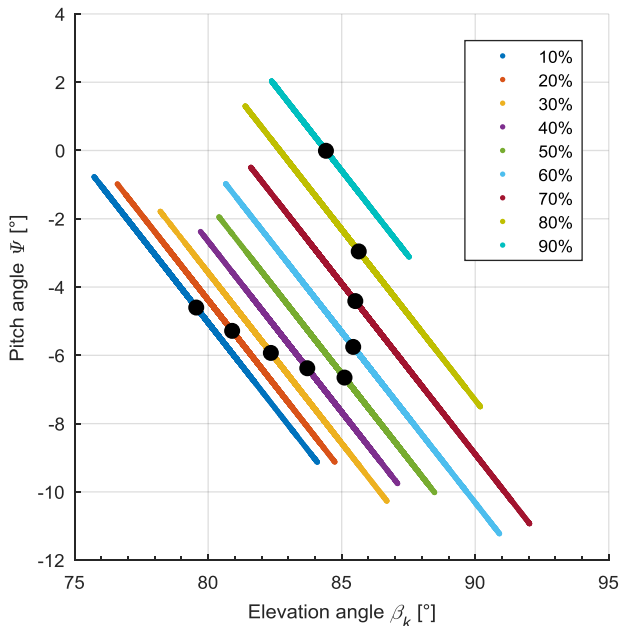


Figure 6.26 Instantaneous pitch angle ψ versus the elevation angle β_k for each power ratio. Black dots: median.

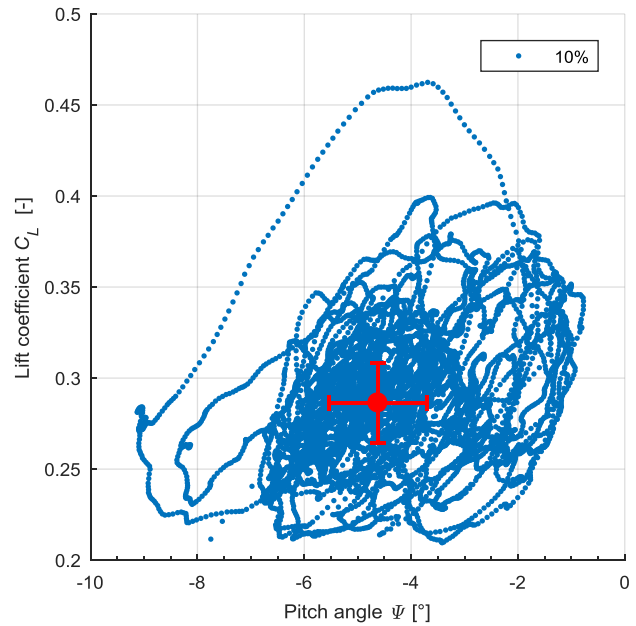


Figure 6.27 Instantaneous lift coefficient versus the pitch angle for 10% of power ratio with median \pm MAD (red).

From Figure 6.26, it can be seen that for a fixed power ratio, the elevation angle varies on average within 8° . The pitch angle fluctuates with the same amplitude since both power ratio angle ε and handle bar angle ζ are assumed to be constant for a given power ratio (Equation (5.28)). The oscillation in elevation angle despite a constant power ratio was already observed in Figure 6.2. Since measurements are performed outdoors, it is relatively difficult to keep the kite at a precise location within the wind window throughout an entire testing session. As a consequence, the instantaneous lift coefficient also exhibits variable values, as shown in Figure 6.27, while the power setting is kept constant. This point cloud stems from the fluctuation in tether force, in wind speed as well as in elevation angle. The instantaneous aerodynamic properties for all the different power ratios are illustrated for completeness in Figure 10.7 of Annex 10.10.

To summarize, the conversion from power ratio to pitch angle exhibits a strange convex profile with important negative values. This leads to unrealistic polar curves with respect to the pitch angle not only for averaged measurements but also for instantaneous one. The explanation for such result is assumed to stem from two sources. Firstly, the relationship between the power ratio and its corresponding angle ε might be different for the line system employed on the TETA setup since its power range is larger than the one experimentally investigated. As illustrated in Figure 6.25, the relationship established experimentally is significantly distant than the one computed from hypothetical polar curves. A second potential explanation comes from natural side wind and/or wind gust at the height of the kite which leads the kite to deviate from its top position. Therefore, steering inputs are required to compensate the deviation. In addition, fluctuations in tether force and car speed are also noticed. As a consequence, the kite deforms and its aerodynamic state is modified even though the power ratio is kept constant. The power ratio angle ε is assumed to be

constant for a given power ratio whereas this might actually not be the case in real flying condition because of the continuous deformation of the kite. Furthermore, the handle bar angle ζ also oscillates throughout the experiment. For those reasons, the present angle of attack – power ratio relationship is advised to be taken with care and would need more investigation.

7 Discussion and Recommendations

7.1 TETA Setup

The TETA setup from TU Berlin has shown great ability to extract relevant information regarding the aerodynamic performance of the kite in a short amount of time ($< 1\text{h}$). The main advantages are the control of the apparent wind speed, the automated and repeatable maneuvers and the possibility to test a wide range of wings. The main limitation of this test bench comes from the requirement of no wind condition which restricts the number of available testing days. Indeed, a light wind would inevitably affect the measurement. A second limiting point is the size of the kite that could be tested. Hummel declares that kites up to 21 m^2 can be investigated with the TETA setup. To allow larger kites to be tested, the trailer should be ballasted and several sensors might be upgraded accordingly.

7.1.1 Methodologies

Both dynamic and static maneuvers have been compared against each other. The first thing to note is that the dynamic approach provides data more quickly than the static methodology. Indeed, it requires roughly 50% less time. In addition, the proportion of time during which relevant data are actually recorded over the total testing time is significantly lower for the dynamic approach: 24% against 64% for the static one. For these reasons, the dynamic approach is more time efficient. However, this might change since it has been suggested to introduce a small pause between two consecutive dynamic maneuvers. Indeed, it was sometimes found that the kite was still losing altitude after the recovery phase while the next dynamic maneuver had already started. Such time break is expected to ensure the kite to be at its equilibrium position at the beginning of the dynamic maneuver and should limit biased measurements.

In addition, it was shown that the short 4 seconds of dynamic powering induce the kite not to reach its quasi-steady equilibrium for any time of the dynamic maneuver. Hence, the quasi-steady model might not be appropriate to derive the aerodynamic properties from dynamic maneuvers. Therefore, two possible adjustments are proposed. The first suggestion consists of keeping the 4 seconds of dynamic maneuvers but adapting the analytical model to take into account the dynamic behaviour of the kite. In this case, the duration of a testing session would remain the same but the mass of the kite as well as its acceleration and the apparent wind speed would have to be determined throughout the entire maneuver. On the one hand, this would lead to a more complex analytical model, but on the other hand, the aerodynamic properties derived from it would be then expected to be more exact and closer to reality. The second alternative adaptation is to extend the powering time in such a way that the kite actually reaches its quasi-steady equilibrium. In that way, the testing session would last longer while the quasi-steady model would earn confidence and become more valid for extracting aerodynamic properties. At some point, increasing this duration asymptotically would eventually be similar to perform static maneuvers.

If such static maneuvers are adopted, some improvements should be considered. Among them, it should be primordial to investigate the same power ratio at least once on both sides of the road. Indeed, it was found for some cases which have not been tested in such a way, that their corresponding measurements presented strange sawtooth profile leading to unrealistic profile for aerodynamic coefficients. Thus, by achieving multiple measurements, the sawtooth profile is expected to be smoothen similarly as for the Hydra V5 at 22 kt. The more repetitions, the better the measurements. In addition, it might be rational to reduce the 10% increment to 5% or even 2% for the purpose of

refining the evaluation of the aerodynamic properties. Although this would significantly increase the testing duration, the obtained measurement data would then provide more accurate and reliable values. A possibility to prevent from long testing periods would be to investigate whether two or more power ratios could be performed during one same run without compromising much the accuracy of the results. Thus, the testing duration would be reduced.

Another aspect of the static maneuver approach is the fact that, although the power ratio is kept constant, the different quantities such as elevation angle, forces and speed are constantly varying. This results in highly fluctuating properties, as shown for instance in Figure 6.27 for the lift coefficient. Thus, one can question whether averaging such fluctuating instantaneous quantities for a fixed power ratio is actually a justified and a valid course of action. An argument for supporting such method comes from the fact that most of the instantaneous values are concentrated around the median as illustrated on Figure 6.27 with the MAD range. Indeed, the point cloud varies horizontally and vertically within 8.35° and 0.253 respectively whereas the MAD range is significantly smaller with 1.84° horizontally and 0.044 vertically. A second justification for taking the average of the instantaneous quantities is that, although different, the curves from both dynamic and static maneuvers present rather the same global trend. As shown on the left hand-side of Figure 6.12, both elevation angles for instance, first present a uniform increase with the power ratio before reaching a certain plateau.

7.1.2 Kite Comparison

It is worth mentioning that kites from different brands are not necessarily designed in the same way. Figure 7.1 shows the evolution of a typical lift curve with the incidence angle for an average wing. The curve first exhibits a steady increase up to a certain angle for which the wing experiences the maximum lift. Past this point, the curve decreases and reaches the stall point. The power range of a kite corresponds to a portion of this curve. Thus, depending on the kite brand's strategy, a manufacturer can decide which power range he wants to assign to his kites.

According to Genetrix Kiteboarding manufacturer [73], two main approaches are generally adopted. One can choose to set the power range upper limit between the maximum load point and stall point (Brand 2 on Figure 7.1). This allows the kite to fly within a wider wind speed range but with the risk of possible back stall. On the contrary, this risk is avoided if the upper limit is set before the maximum load point (Brand 1 on Figure 7.1). However, this also limits the wind speed range for the kite. Although a trade-off has to be made, the upper limit of the power range always corresponds to the full power situation, namely when the bar is completely pulled towards the pilot.

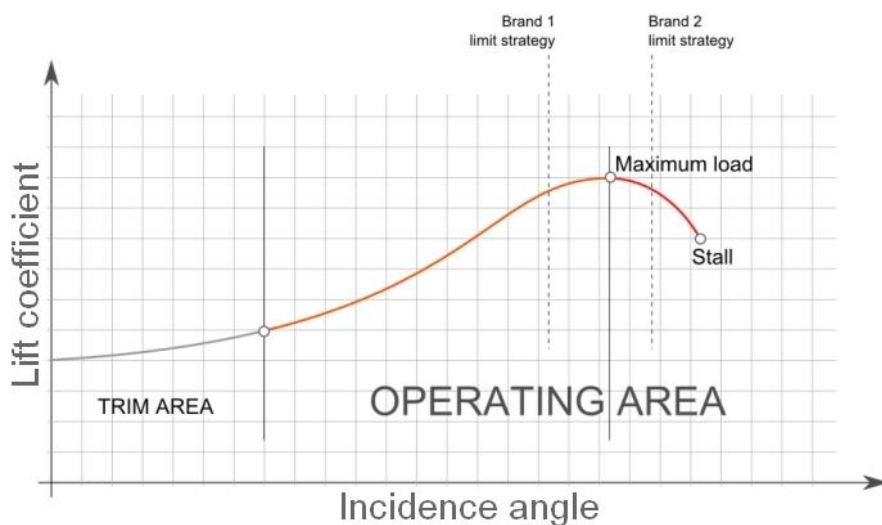


Figure 7.1 Typical lift polar curve. Modified from [73].

These two distinct design strategies can be noticed in Figure 2.32 obtained by Hummel from his TETA setup. For instance, the North Vegas kite (NV), for which neither the stall phase, nor the maximum lift is observed, rather follows

the strategy #1 of Figure 7.1. On the other hand, the Genetrix Hydra V5 kite (GH) not only experiences the maximum load but also evolves within the stall phase. This kite corresponds thus to strategy #2 of Figure 7.1. Therefore, both kites not only do not follow the same design strategy, but also might not necessarily have the same power range.

Given this, a question might arise when one wants to compare kites with distinct power range but both compatible with the 500 mm power range of the TETA test rig. Assuming Kite A works with 400 mm while Kite B has a power range of 300 mm, how can they be compared adequately against each other? This concern is actually not a real problem but rather a limitation of the comparison range. Indeed, the 100% of power ratio for Kite A and Kite B corresponds to the 100% power ratio for the line system as illustrated on Figure 7.2. Then, the rest of the two kite power ranges is simply deployed over the 500 mm power range of the lines. Therefore, both kites have distinct line power ratios when their designed depower setting is reached. Kite A has a line power ratio of 20% when fully depowered whereas Kite B is entirely depowered for a line power ratio of 40%. Beyond this point, loosening the back lines even more does not have significant effect on the kite. Indeed, as shown in Figure 2.32, the glide ratio rather stays constant for small values of power ratio.

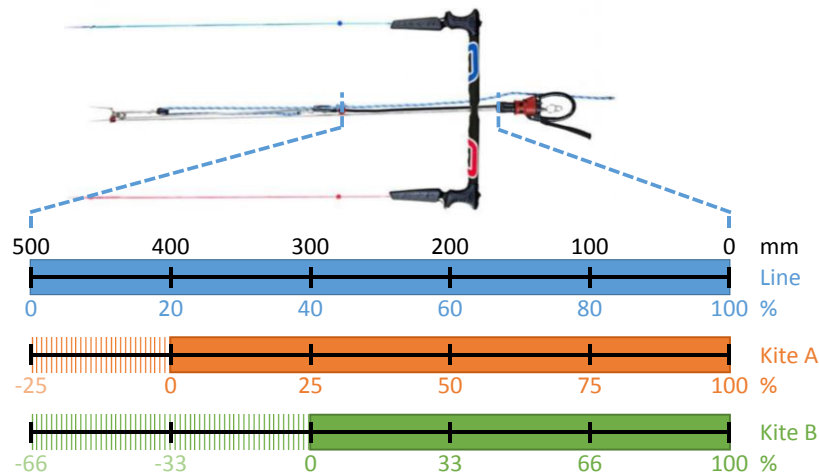


Figure 7.2 Example of the power range of the line system (blue) and the power range of two distinct kites, namely Kite A of 400 mm (orange) and Kite B of 300 mm (green) power range.

As it is now, the TETA test bench allows to cover the designed power range of the kite as well as the trim area shown on Figure 7.1. However, since the 100% power range of the kite is aligned to the 100% power range of the TETA line, the region passed the designed upper limit of the kite is not investigated with the current setup. By looking at Figure 2.32, it can be assumed that, since its curve has not reached its maximum point yet, the North Vegas kite could be investigated even more if the handle bar could be pulled further.

To solve this point, the kite power range should not be aligned with the 100% of power range of the line but rather shifted slightly away from it. By looking at Figure 7.2, this would mean that the orange and green power range would have to be set roughly in the middle of the blue one. In that way, both extremities of the kite power range could be further investigated with the TETA test bench. Shifting the kite power range along the line power range can be done by shortening the initial back line of the kite.

The process of defining the upper limit of the kite power range is commonly achieved manually. The pilot/designer himself gauges for which power settings the kite provides most power. This method is undoubtedly dependent on the perception of the pilot. In addition, the polar curve (Figure 7.1) is given for one specific wind condition and might be shifted for others. In that way, the upper limit of the power range might also vary from one wind speed to another. Thus, in addition to comparison purposes, the TETA setup is advised to be used to define the most appropriate power range for new kites out of the entire polar curve by systematically investigating distinct wind speeds. In this sense, the characterization of the power range is no more qualitative but becomes quantitatively justified.

7.2 Source of Error

Measurement errors are commonly divided into two categories [74]. A random error is a fluctuation in the measured value. It can be reduced by repeating multiple measurements and averaging them. By contrast, a systematic error is a repeatable inaccuracy that remains the same no matter the number of repetitions. If known, the resulting bias can be compensated by applying a correction factor. Both errors can be quantified or unquantified.

7.2.1 Random Quantified Error

Each sensor is built with its own accuracy as detailed in Chapter 4.3.1. Thus, the measured value is given within the sensor resolution range. Since multiple repetitions have been performed for both dynamic and static maneuvers, the median absolute deviation of the median provides an idea of the preciseness of the measurements. Table 7.1 lists the measurement accuracies. It can be noticed that dynamic maneuvers lead to better accuracy than static maneuvers. This feature comes from the fact that 95 maneuvers have been performed with the dynamic approach whereas static methodology only counts 19 maneuvers. Indeed, the more measurements, the better the accuracy becomes.

Table 7.1 Accuracy of computed values

Measurement		Sensor resolution	MAD dynamic	MAD static
Apparent elevation angle	$\Delta\vartheta_w$	$\pm 1.78^\circ$	$\pm 0.73^\circ$	$\pm 1.74^\circ$
Tether force	ΔF_t	± 2.2 N for 1000 N	± 28.86 N	± 49.76 N
Wind speed	ΔV_w	± 0.05 m/s	± 0.20 m/s	± 0.35 m/s

7.2.2 Random Unquantified Error

The road, on which the investigation is achieved, is assumed to be perfectly flat. However, due to small gaps between two successive concrete plates as well as deteriorations of the road, the test bench has encountered some bumps along the driveway. These small shocks might be transmitted up to the angular sensor and might affect the measurement. This minor discrepancy is assumed to be absorbed by averaging multiple measurements.

In order to have clean prescribed velocity, the test day is selected to have as little wind as possible. However, wind gusts cannot be predicted nor detected with the current setup. In addition, a light natural wind might occur at the height of the kite impacting on the kite behaviour. Due to their low magnitude and variable direction, both wind gusts and light natural wind at kite height are expected to be imbibed by the averaging process.

7.2.3 Systematic Unquantified Error

The major unknown of the experiment remains the air speed that the kite actually experiences. Indeed, during the entire investigation, it is assumed that the kite apparent wind speed is equivalent to the velocity measured by the anemometer. Nevertheless, a natural wind, relatively low and variable at the anemometer, can also be more significant and unidirectional at kite height leading to a systematic error of the measurement. In addition, for dynamic maneuvers, the kite picks up speed as its angular position varies by 13.2° within 4 seconds. By assuming a uniform circular motion, this angular variation translates into an average velocity increase of 1.4 m/s with instantaneous peaks up to +10 m/s. So far, this velocity increase is neglected. However, as the square of the apparent velocity is used to compute the aerodynamic coefficients, a small discrepancy in V_a can lead to large error in C_L and C_D . Therefore, assessing the kite apparent velocity is one of the most crucial point to improve for limiting this systematic error.

Besides, although the pilot tries his best to keep the kite on top of the wind window, the wing inevitably deviates from this position because of light side wind. However, thanks to the complex combination of three angular sensors, the glide ratio can be assessed even if the kite is completely off track. Nevertheless, the aerodynamic forces, the tether force as well as the forces acting along the tether are assumed to be contained within a vertical plane aligned with the car-trailer-track set. Thus, the 2D deviation of the kite is not taken into account when computing the aerodynamic coefficients. This can lead to systematic error if the kite is constantly shifted on one side of the track but this can also

become a random error if the wing is oscillating around its prescribed position. To limit this error, either the measurements should be performed only when the wind is totally absent or either the analytical model should be extended to include such 2D deviation.

An underlying issue derived from the two previous comments is the validation of the quasi-steady model as a good representation of the reality. Indeed, it can be discussed whether this simplification is legitimate while some quantities significantly vary in time for both dynamic and static maneuvers. In addition to pick up in flying speed during dynamic maneuvers, the acceleration may not be negligible either. The average tangential acceleration of the kite is roughly 0.46 m/s^2 but peaks up to 5 m/s^2 are also noticed. Moreover, it has been shown that the elevation angle for the static maneuver (Figure 6.2) was greatly varying within a short period of time. For these reasons, the quasi-steady kite state might slightly differ from reality, leading to systematic errors in the results.

In addition, the deformation of the kite was not considered so far. However, it is undeniable that the kite experiences some deformation due to its flexible nature. Thus, each power setting prescribes a distinct given shape to the kite, leading to a systematic discrepancy with respect to the assumed unmodified shape. Besides this main deformation, the kite shape is also affected by steering inputs as well as strong and fluctuating load even for a fixed power ratio, which can be seen as a random error since this effect can be discarded by averaging multiple measurements.

Another source of error was mentioned to stem from the difference in power range of both line systems. Indeed, the line of the TETA setup presents a power range of 50 cm whereas the one used to established the power ratio angle features 36 cm of power range. Although the missing 14 cm are extrapolated, a systematic error might arise from this distinction. In addition, due to aging, the lines might not exactly measure 24 m but can be longer or shorter, slightly affecting the results.

Still regarding the tether, it is assumed that its mass is uniformly distributed. However, a large part of it is actually concentrated at the bottom of the tether because of the handle bar as well as the security system. This uneven distribution might systematically affect the sag of the tether which, in turn impedes on elevation angle as well as the tether force at the kite. Furthermore, both drag and lift of the tether are established using the formulas of Hoerner [66] for circular bodies as well as an equivalent diameter supposed to represent the effect of multiple lines. Nevertheless, both section and diameter vary along the tether leading to a systematic error in comparison to the situation assumed.

7.2.4 Summary

As a short summary, the main sources of error are recalled in Table 7.2.

Table 7.2 Source of error

Error	Systematic	Random
Unquantified	Unknown V_a at kite height Constant unidirectional natural wind Pick-up speed during dynamic maneuvers Kite 2D deviation Quasi-steady model validation Kite deformation Power range and line system dissimilarity Tether mass and geometry	Imperfect road profile Light natural wind and wind gusts Kite 2D deviation Kite deformation
Quantified	Intrinsic sensor accuracy Repetition of individual measurements (MAD)	

7.3 Parameter Sensibility

As indicated in Chapter 7.2.3, the main uncertainty is the apparent wind speed at the kite height. Because of potential natural wind, it can reasonably be assumed that the magnitude of the air velocity experienced by the kite is greater than the one recorded at the anemometer. Thus, this speed discrepancy leads to an overestimation of the aerodynamic coefficients C_L , C_D (Equation (2.25) and Equation (2.26) respectively). Then, although the glide ratio should be independent of the velocity, its derivation is altered since it is computed from the elevation angle and the tether force at the kite, which both vary with V_a . To illustrate the sensibility of V_a , the glide ratio and the aerodynamic coefficients, shown in Figure 7.3, are derived for apparent wind speeds 25% and 50% greater than the one measured at the anemometer, namely $V_a = 14.47$ m/s (orange) and $V_a = 17.36$ m/s (yellow) respectively.

As mentioned through Figure 6.17, the diameter of the tether plays a sensible role in its drag and lift effects on the kite aerodynamic properties. Therefore, it also affects the computed glide ratio of the kite. As an illustration in Figure 7.3, a thinner and a larger diameter, namely $d_t = 1$ mm (purple) and $d_t = 2$ mm (green), are assumed to assess the resulting effect on the glide ratio and on the aerodynamic coefficients.

To allow comparison, the reference curves (thick blue), shown in Figure 7.3, are obtained from the tether sag model (Chapter 6.6) and correspond to the dashed green lines of Figure 6.19. The default parameters are: $V_a = 11.57$ m/s, $d_t = 1.5$ mm.

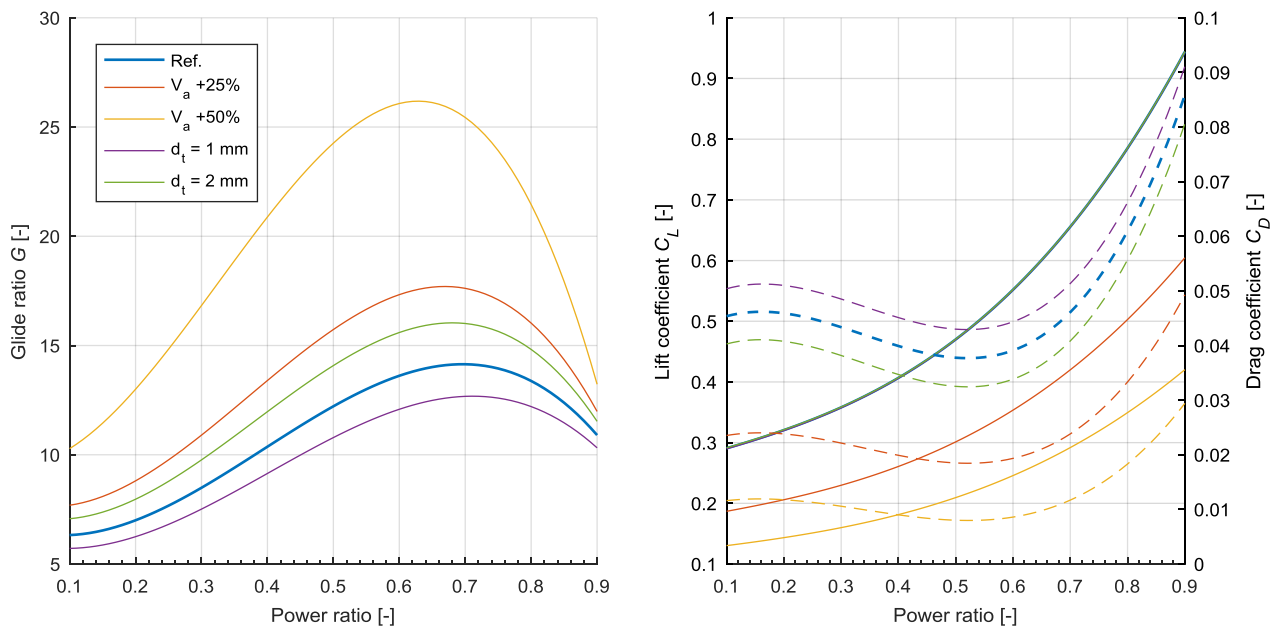


Figure 7.3 Glide ratio, lift coefficient (solid line) and drag coefficient (dashed line) for an increase in V_a of +25% (orange), of +50% (yellow), for a d_t of 1 mm (purple), of 2 mm (green) and for default value (dark blue).

As suggested, the apparent velocity appears to be a critical parameter. Indeed, L/D , C_L and C_D are strongly influenced by the variation in V_a . An increase of 50% almost doubles the initial glide ratio. Thus, knowing the real apparent velocity is of great importance for accurately assessing the aerodynamic properties of a wing. For this reason, the development of a systematic measurement of the apparent wind speed at the kite is one of the most important improvement to achieve.

On the other side, the tether diameter only affects the drag coefficient, which then alters the glide ratio. Although the sensibility of d_t is smaller than the one from V_a , its effect on the glide ratio is still consequent and leads to an average variation of $\pm 10\%$. Moreover, although not investigated, it can reasonably be assumed that the tether drag coefficient adopted from Hoerner [66] slightly differs from the actual one. Therefore, the tether should correctly be modelled as a whole in order to compute accurate aerodynamic properties.

7.4 Main Recommendations

Since the apparent wind velocity V_a is the most critical unknown, a wind speed measurement device is recommended to be mounted directly on the kite. This is expected to significantly reduce the uncertainty associated with the actual wind model. Thus, the analytical kite model will benefit from an accurate value of V_a leading to a more precise and reliable assessment of the aerodynamic properties. Furthermore, the wind velocity profile will also be rectified and will in turn improve the tether sag model.

A second sensitive parameter affecting the aerodynamic properties is the tether diameter and therefore its corresponding drag effect. Moreover, the tether drag coefficient assumed for the present study might slightly diverge from the real one. Therefore, as a suggestion, the appraisal of the tether drag effect is advised to be investigated by performing an experimental drag study of the line itself, in a wind tunnel for example.

Regarding the dynamic approach, it is suggested to insert a short pause between two consecutive dynamic maneuvers to make sure the kite is at its equilibrium position when the maneuver starts. Furthermore, it might be favourable to adjust the quasi-steady model to take the acceleration of the kite and its dynamic behaviour into consideration. Alternatively, it might be meaningful to extend the powering time to let say 10 seconds to see how the results are affected.

On the side of the static testing method, it is recommended to achieve runs for the same power ratio, at least once, on both sides of the track. This is expected to limit the sawtooth profile occasionally observed for some measurements. As a second suggestion, it might be relevant to decrease the increment between power ratios with the aim of having a more refined characterization of the aerodynamic properties.

As general notice, it is reminded to perform measurement when the natural wind is as low as possible. This should provide clean and stable measurements. Eventually, the analytical model for both methodologies should be extended to include and assess the deviation of the kite motion from the 2D plane.

As for the relationship between power ratio and angle of attack, the same investigation of the power ratio angle should be carried out with the actual set of line used on the TETA test bench. This is expected to improve the correspondence from $PR\%$ to AoA. As a supportive validation, an inertia measurement unit is suggested to be mounted on the kite to provide directly the pitch angle with respect to its corresponding power setting.

8 Conclusion

In the context of Airborne Wind Energy, the wing efficiency for pumping kite power systems, as well as its aerodynamic properties play a key role at the development stage for power production and cost estimation. Furthermore, the performance coefficients serve as a basis during kite design development and are used for kite comparison. Moreover, numerical simulations for wing performance require experimental data for the validation of their model. Therefore and generally speaking, a high definition of the aerodynamic coefficients is of great interest.

8.1 Achieved Results

The goal of this M.Sc. Thesis was to improve the assessment methodology as well as the exactitude of the aerodynamic properties regarding the Kitepower wing through experimental investigation. To complete this general assignment, four sub-research questions were studied successively.

As an opening, a new static assessment methodology was suggested and investigated experimentally against the current dynamic approach from Hummel [48]. The comparison of both methodologies has led to relatively different results suggesting a dynamic behaviour of the kite when dynamic maneuvers were performed. Moreover, it was found that the kite did not instantaneously react to the power input leading to an overestimation of its aerodynamic coefficients for the first 75% of power ratio. Therefore, although less time efficient, the static maneuvers are expected to provide more realistic and reliable results when assessing the kite aerodynamic properties.

Up to this point, the kite mass as well as the mass, lift and drag of the tether were not included in the analytical model of the system. To assess their effects on the kite aerodynamic properties, their contributions were individually studied by lumping their equivalent forces to the kite. It was found that both kite mass and tether drag had a strong influence on the kite glide ratio. In addition, the lift coefficient was mainly altered by both kite and tether mass whereas the tether drag notably affected the drag coefficient. Considering all these effects together has led to a global variation in G , C_L and C_D of +29%, +16% and -10% respectively. Therefore, except for the tether lift, these effects played an important role and should not be neglected.

As a third point, the sag of the tether, hitherto neglected, was investigated by considering the distributed weight, lift and drag acting along the tether. The tether sag was identified to induce an average elevation angle difference of 3.5° and 2.5° when a 2 m/s natural wind was considered or neglected respectively. This variation was found to increase linearly as the power ratio decreased. In addition, the tether force at the kite was reduced by 15 N affecting the aerodynamic properties, especially the drag coefficient (-25%), consequently the glide ratio (+55%).

With the purpose of using the computed aerodynamic curves for computational simulations, the conversion from power ratio to angle of attack was eventually assessed. The relationship between the power ratio and its corresponding angle was experimentally determined. Nevertheless, this correspondence may not hold for real flying condition. Furthermore, the line investigated experimentally was different than the one used on the TETA setup. Therefore, the $PR\%$ - AoA correlation could not be established effectively.

Finally, it has been highlighted that both apparent wind velocity and tether diameter could sensibly affect the results. Therefore, their precise determination is of great importance when assessing the aerodynamic properties of a wing.

All together it can be concluded that the new static testing methodology provides an improvement of the aerodynamic properties assessment when mass and tether aerodynamic effects as well as tether sag are considered. This improvement could be even stronger with an accurate wind speed measurement mounted on the kite. Although not expressed as a function of AoA, the determined aerodynamic coefficients offer a better insight into the kite performance and can be adopted as reference value for computational simulation and kite design development.

8.2 Future Development

As future work, possible directions of research are suggested from the outcome of this M.Sc. Thesis.

The assessment of the apparent wind speed experienced by the kite is certainly the most important point to achieve. Generally speaking, this information is of great interest for experimental investigation. Fortunately, researches on this topic are currently underway.

The relationship between power ratio and angle of attack should be investigated in more detail. The use of an inertia measurement unit might be an essential improvement in directly relating the pitch angle to the power setting. Hopefully, this will provide a better insight into the pitch angle variation and ultimately into the angle of attack.

The deformation of the kite did not fall within the scope of this study. Nevertheless, it might be relevant to investigate the alteration of the kite shape for different inputs, such as wind speed, power setting or steering input.

Speaking of steering, a possible next step in pushing the research further might be to investigate the effect of such maneuvers on the kite behaviour, deformation and performances.

9 References

- [1] International Energy Agency (IEA), “Key world energy trends - excerpt from: world energy balances,” Paris, France, 2016.
- [2] United Nations, “World population prospects: the 2015 revision,” *United Nations, Department of Economic and Social Affairs, Population Division*. 2015.
- [3] Houghton JT *et al.*, “Climate change 2001: the scientific basis,” 2001.
- [4] United Nations, “Paris agreement (COP21),” Paris, France, 2015.
- [5] Swiss Federal Office of Energy (SFOE), “Current situation in respect of the search for sites,” 2015. [Online]. Available: <http://www.bfe.admin.ch/radioaktiveabfaelle/05182/index.html?lang=fr>. [Accessed: 26-Oct-2016].
- [6] Global Wind Energy Council (GWEC), “Global wind report 2015,” Brussels, Belgium, 2016.
- [7] REN21, “Renewables 2016 global status report,” Paris, France, 2016.
- [8] A. Cherubini, A. Papini, R. Vertechy, and M. Fontana, “Airborne wind energy systems: a review of the technologies,” *Renew. Sustain. Energy Rev.*, vol. 51, pp. 1461–1476, 2015.
- [9] U. Ahrens, M. Diehl, and R. Schmehl, *Airborne wind energy*. Berlin: Springer Berlin Heidelberg, 2013.
- [10] J. Breukels, “An engineering methodology for kite design,” Delft University of Technology, 2011.
- [11] M. B. Ruppert, “Development and validation of a real time pumping kite model,” Delft University of Technology, 2012.
- [12] B. M. R. Franca, “A tool for aerodynamic analysis of flexible kites,” Delft University of Technology, 2014.
- [13] A. Viré and R. Schmehl, “How to harness wind energy with traction kites,” *Rev. Environ. Sci. Biotechnol.*, pp. 1–4, 2014.
- [14] B. H. Thacker, S. W. Doebling, F. M. Hemez, M. C. Anderson, J. E. Pepin, and E. a. Rodriguez, “Concepts of model verification and validation,” 2004.
- [15] C. L. Archer, “An introduction to meteorology for airborne wind energy,” in *Airborne wind energy*, U. Ahrens, M. Diehl, and R. Schmehl, Eds. Berlin: Springer Berlin Heidelberg, 2013, pp. 81–94.
- [16] C. L. Archer and K. Caldeira, “Global assessment of high-altitude wind power,” *Energies*, vol. 2, no. 2, pp. 307–319, 2009.
- [17] REN21, “Renewables 2005 global status report,” Washington DC, USA, 2005.
- [18] ENERCON GmbH, “Enercon E-33,” Aurich, 2005.
- [19] European Wind Energy Association (EWEA), “Part I: technology,” in *Wind Energy - The Facts*, Brussels, Belgium, 2009.

- [20] J. S. Hill, "World's largest wind turbines begin generating power at burbo bank extension," *CleanTechnica*, 2016. [Online]. Available: <https://cleantechnica.com/2016/11/22/worlds-largest-wind-turbines-begin-generating-power-burbo-bank-extension>. [Accessed: 07-Dec-2016].
- [21] Thomas Gibson, "The view from the world's biggest wind turbine," *Bloomberg*, 2016. [Online]. Available: <http://www.bloomberg.com/news/videos/b/60fa3ff5-4ce8-4d45-a794-03358d96ed87>. [Accessed: 07-Dec-2016].
- [22] DONG energy, "Successful installation of world's largest offshore wind turbine at Burbo Bank Extension," *DONG energy*, 2016. [Online]. Available: <http://www.burbobankextension.co.uk/en/news/articles/successful-installation-of-world's-largest-offshore-wind-turbine-at-burbo-bank-extension>. [Accessed: 14-Dec-2016].
- [23] D. Rob, "Building the world's biggest wind turbine," *EniDay*, 2016. [Online]. Available: https://www.eniday.com/en/technology_en/making-the-worlds-biggest-wind-turbine. [Accessed: 07-Dec-2016].
- [24] International Energy Agency (IEA), "Technology roadmap wind energy," Paris, France, 2013.
- [25] Renewable Energy Website, "Betz limit," *Renewable Energy Website*. [Online]. Available: <http://www.reuk.co.uk/wordpress/wind/betz-limit/>. [Accessed: 16-Dec-2016].
- [26] R. Thresher, M. Robinson, and P. Veers, "To capture the wind," *IEEE Power Energy Mag.*, vol. 5, no. 6, pp. 34–46, Nov. 2007.
- [27] J. Quilter, "Picture gallery - world's largest blade begins journey to Scotland," *Windpower Monthly Magazine*, 2013. [Online]. Available: <http://www.windpowermonthly.com/article/1191655/picture-gallery-worlds-largest-blade-begins-journey-scotland>. [Accessed: 07-Dec-2016].
- [28] Keystone Tower Systems, "In field," *Keystone Tower Systems*, 2011. [Online]. Available: <http://keystonetowersystems.com/in-field-2>. [Accessed: 07-Dec-2016].
- [29] M. L. Loyd, "Crosswind kite power," *J. Energy*, vol. 4, no. 3, pp. 106–111, 1980.
- [30] U. Ahrens, M. Diehl, and R. Schmehl, "Front matter," in *Airborne wind energy*, U. Ahrens, M. Diehl, and R. Schmehl, Eds. Berlin: Springer Berlin Heidelberg, 2013, pp. i–xxiii.
- [31] R. Schmehl, "Introduction to airborne wind energy," *Airborne wind energy lecture*. University of Technology Delft, 2016.
- [32] M. Diehl, "Airborne wind energy: basic concepts and physical foundations," in *Airborne wind energy*, U. Ahrens, M. Diehl, and R. Schmehl, Eds. Berlin: Springer Berlin Heidelberg, 2013, pp. 3–22.
- [33] M. C. de O. De Lellis, "Airborne wind energy with tethered wings: modeling, analysis and control," Federal University of Santa Catarina, 2016.
- [34] J. Heilmann, "The technical and economic potential of airborne wind energy," Utrecht University, 2012.
- [35] I. Argatov, P. Rautakorpi, and R. Silvennoinen, "Estimation of the mechanical energy output of the kite wind generator," *Renew. Energy*, vol. 34, no. 6, pp. 1525–1532, 2009.
- [36] P. Williams, B. Lansdorp, and W. Ockels, "Optimal crosswind towing and power generation with tethered kites," *J. Guid. Control. Dyn.*, vol. 31, no. 1, pp. 81–93, 2008.
- [37] J. Anderson Jr, *Fundamentals of aerodynamics*, vol. Fifth Edit. Maryland, USA, 2010.
- [38] B. Houska and M. Diehl, "Optimal control of towing kites," in *Proceedings of the 45th IEEE Conference on Decision and Control*, 2006, no. 3, pp. 2693–2697.
- [39] R. Leloup, K. Roncin, G. Bles, J.-B. Leroux, C. Jochum, and Y. Parlier, "Estimation of the lift-to-drag ratio using the lifting line method: application to a leading edge inflatable kite," in *Airborne Wind Energy*, U. Ahrens, M.

- Diehl, and R. Schmehl, Eds. Berlin: Springer Berlin Heidelberg, 2013, pp. 339–355.
- [40] G. M. Dadd, D. A. Hudson, and R. A. Shenoj, “Comparison of two kite force models with experiment,” *J. Aircr.*, vol. 47, no. 1, pp. 212–224, 2010.
- [41] G. M. Dadd, D. A. Hudson, and R. A. Shenoj, “Determination of kite forces using three-dimensional flight trajectories for ship propulsion,” *Renew. Energy*, vol. 36, no. 10, pp. 2667–2678, 2011.
- [42] A. de Wachter, “Deformation and aerodynamic performance of a ram-air wing,” Delft University of Technology, 2008.
- [43] R. van der Vlugt, “Aero- and hydrodynamic performance analysis of a speed kiteboarder,” Delft University of Technology, 2009.
- [44] J.C. Stevenson, “Traction kite testing and aerodynamics,” University of Canterbury, 2003.
- [45] K. V Alexander and J. C. Stevenson, “A test rig for kite performance measurement,” *Proc. Inst. Mech. Eng. Part B J. Eng. Manuf.*, vol. 215, no. 4, pp. 595–598, 2001.
- [46] G. M. Dadd, “Kite dynamics for ship propulsion,” University of Southampton, 2013.
- [47] D. Costa, “Experimental investigation of aerodynamic and structural properties of a kite,” Swiss Federal Institute of Technology Zurich, 2011.
- [48] J. Hummel, “Automatisierte Vermessung und Charakterisierung der dynamischen Eigenschaften seilgebundener, vollflexibler Tragflächen,” Berlin University of Technology, 2017.
- [49] C. Elfert, “Specs Prüfstand,” Berlin University of Technology, Berlin, Germany, 2016.
- [50] J. Hummel, “TETA: Test and Evaluation of Tethered Airfoils,” 2016. [Online]. Available: http://www.mpm.tu-berlin.de/menue/forschung/projekte/teta_kitepruefstand/. [Accessed: 11-Jan-2017].
- [51] J. Stevenson, K. Alexander, and P. Lynn, “Kite performance testing by flying in a circle,” *Aeronaut. J.*, vol. 109, no. 1096, pp. 269–276, 2005.
- [52] J. C. Stevenson and K. V Alexander, “Circular flight kite tests: converting to standard results,” *Aeronaut. J.*, vol. 110, no. 1111, pp. 605–614, Sep. 2006.
- [53] L. Fagiano, “Control of tethered airfoils for high-altitude wind energy generation,” Politecnico di Torino, 2009.
- [54] R. van der Vlugt, “Quasi-steady model of a pumping kite power system,” *Renew. Energy*, p. 14, 2014.
- [55] J. F. Manwell, J. G. McGowan, and A. L. Rogers, *Wind energy explained: theory, design and application*, Second Edi. John Wiley & Sons, Ltd., 2009.
- [56] R. B. Stull, *Meteorology today for scientists and engineers*, 2nd Editio. University of British Columbia: West Pub., 1995.
- [57] SwitchKites, “Switch Kiteboarding - Method2,” 2016. [Online]. Available: <http://switchkites.com/method2.html>. [Accessed: 20-Jan-2017].
- [58] M. N. Noom, “Theoretical analysis of mechanical power generation by pumping cycle kite power systems,” Delft University of Technology, 2013.
- [59] M. M. Diehl, “Real-time optimization for large scale nonlinear processes,” Ruprecht-Karls-Universität Heidelberg, 2001.
- [60] B. Houska, “Robustness and stability optimization of open-loop controlled power generating ites,” Ruprecht-Karls-Universität Heidelberg, 2007.

- [61] I. Argatov, P. Rautakorpi, and R. Silvennoinen, "Apparent wind load effects on the tether of a kite power generator," *J. Wind Eng. Ind. Aerodyn.*, vol. 99, no. 10, pp. 1079–1088, 2011.
- [62] P. Rautakorpi, "Mathematical modeling of kite generators," Tampere University of Technology, 2013.
- [63] S. K. Varma and J. S. Goela, "Effect of wind loading on the design of a kite tether," *J. Energy*, vol. 6, no. 5, pp. 342–343, 1982.
- [64] Genetrix Kiteboarding, "Hydra V5," 2013. [Online]. Available: <http://genetrixkites.com.ua/products/hydra-v5/>. [Accessed: 27-Jan-2017].
- [65] North Kiteboarding, "Vegas 2015 Manual," 2015.
- [66] S. F. Hoerner, *Fluid-dynamic drag*. Bricktown, New Jersey, USA, 1965.
- [67] "MATLAB R2016b." The MathWorks Inc., Natick, Massachusetts, 2016.
- [68] N. Jasuja and P. Menon, "Mean vs Median," *Diffen LLC*, 2017. [Online]. Available: http://www.diffen.com/difference/Mean_vs_Median. [Accessed: 01-Feb-2017].
- [69] C. Leys, C. Ley, O. Klein, P. Bernard, and L. Licata, "Detecting outliers: do not use standard deviation around the mean, use absolute deviation around the median," *J. Exp. Soc. Psychol.*, vol. 49, no. 4, pp. 764–766, 2013.
- [70] TP de Physique Générale, "Introduction au calcul d'incertitude," Lausanne, Switzerland.
- [71] V. Lindberg, "Uncertainties and error propagation," p. 28, 2000.
- [72] U. Fechner, R. van der Vlugt, E. Schreuder, and R. Schmehl, "Dynamic model of a pumping kite power system," *Renew. Energy*, vol. 83, pp. 705–716, 2015.
- [73] S. Vlaminck, "The kite polar signature," Bidart, France, 2017.
- [74] D. Deardorff, "UNC physical lab manual uncertainty guide," Chapel Hill, 2000.
- [75] C. L. Archer and K. Caldeira, "Atlas of high altitude wind power," Stanford, 2008.
- [76] K. Marvel, B. Kravitz, and K. Caldeira, "Geophysical limits to global wind power," *Nat. Clim. Chang.*, vol. 2, no. 9, pp. 1–4, 2012.
- [77] M. Richard, "First Solar's Cells Break Efficiency Record," *MIT Technology Review*, 2016. [Online]. Available: <https://www.technologyreview.com/s/600922/first-solars-cells-break-efficiency-record/>. [Accessed: 04-Jan-2017].
- [78] M. Siemens AG, "First installation of Siemens' 6 megawatt wind turbine in Germany," www.siemens.com/press, 2014. [Online]. Available: http://www.siemens.com/press/pool/de/pressebilder/2014/windpower-renewables/300dpi/im2014120221wp_300dpi.jpg. [Accessed: 05-Jan-2017].
- [79] Side-Shore, "North Vegas 2013," 2012. [Online]. Available: <http://blog.side-shore.com/2012/10/17/test-de-la-north-vegas-2013/>. [Accessed: 27-Jan-2017].
- [80] GoKite, "North Vegas 2014," 2014. [Online]. Available: <http://www.gokite.com.br/loja/kites/north-vegas-2014/>. [Accessed: 27-Jan-2017].

10 Annexes

10.1 Global Wind Potential

In general, wind speed increases with altitude, so does the wind power density. Archer and Caldeira [16] assessed the global wind power by looking at detailed atlas maps of WPD for several altitudes. These maps not only provide relevant information regarding future wind energy harvester location, but they also display the evolution in wind power density with height. Figure 10.1 presents the wind power density available during 50, 68 and 95% of the time between 1979 and 2006. The left-hand side maps illustrate the available power at 80 m height, which conventional wind turbines can extract from [15]. Few land areas offer wind power densities greater than 0.3 kW/m^2 , even for 50% of the time. On the right-hand side, the situation is presented for an altitude of 500 m which can be representative of future Airborne Wind Energy harvester. The main difference lays in the fact that the maps of the 50 and 68% especially, show an evident increase in the WPD over the globe. According to the right-hand side of Figure 10.1, an AWE system could potentially experience a wind power density of 1 kW/m^2 during 50% of the time in some locations. These resource maps illustrate the high potential of wind energy in general. Although very high altitudes are not directly related to this work, it is worth mentioning that the WPD is five times greater at $10'000 \text{ m}$ than at $1'000 \text{ m}$, with values up to 10 kW/m^2 when tapping into jet streams. This is suggested when looking at jet streams located around the South Pole.

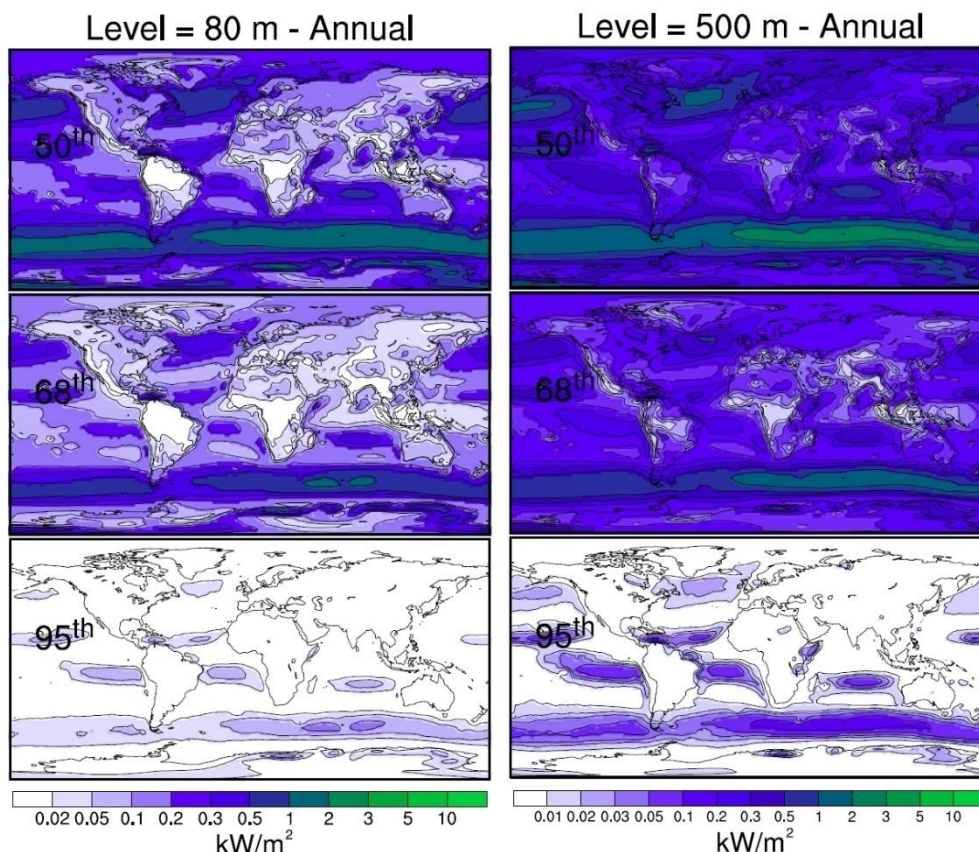


Figure 10.1 Wind power density for 80 m and 500 m, that was exceeded 50, 68, 95% of the time between 1979-2006 [75].

Recent assessments have suggested that earth's winds could provide enough power to supply the world electrical power demand [76]. Indeed, estimations predict a potential extraction of 400 TW by means of wind turbines whereas Airborne Wind Energy systems could convert more than 1800 TW from the wind kinetic energy. However, such energy extraction would lead to severe climatic changes. Nevertheless, the author claims that 18 TW, which corresponds to the global primary power demand, could be obtained from the wind in a sustainable way without engendering any significant negative effect. In conclusion, the wind could potentially act as a great actor of energy supplier.

10.2 Advantage of Airborne Wind Energy Systems

The AWE systems are able to harvest wind energy at high altitudes where wind are more constant and stronger. Recalling Equation (2.7) and assuming typical values of C_L and C_D to be respectively 1 and 0.07 and an incoming wind speed V_w of 13 m/s lead to a theoretical power output of 40 kW/m² of wing area [32]. Although this value is not realized yet by any research groups, it seems to be reachable in close future. This 40 kW/m² power density value can be used to compare AWE system against other power generation systems.

In February 2016, the efficiency record for a solar cell has been broken by converting 22.1% of sunlight energy into electricity [77]. The solar radiation reaching the earth's surface is known to be about 1.3 kW/m². Thus, such solar panels could potentially have a power density of 0.29 kW/m². This value is 140 times lower than the AWE power density of 40 kW/m². Looking at conventional wind energy, the power density of an ideal wind turbine working at Betz limit (59.3%) with the same incoming wind speed ($V_w = 13$ m/s) is almost 0.8 kW/m² (Equation (2.2)). Although this value is larger than the PV power density, it is still 50 times lower than the power density of AWE system. These two examples demonstrate the high power density of Airborne Wind Energy system.

Another aspect could be illustrated if the wing of an Airbus 380 was used as an apparatus for AWE harvester. The 845 m² wing could theoretically generate more than 30 MW of power. The whole system, composed by the 80 m wide wing and a 1 km long cable, would weight about 39 tons [32]. To provide the same amount of power with conventional wind turbines, four of the Enercon E-126 7.5 MW would be required in ideal conditions. One single blade of such wind turbine already weights 65 tons. Thus, the total blades weight for the four E-126 wind turbines reaches 780 tons, which is 20 times more than the corresponding AWE system. Moreover, if the weights of the rotors and towers are included (12400 tons), the 30 MW airborne system becomes 300 times lighter than these four conventional wind turbines [32].

This significant weight difference is due to the fact that the outer 30% of the wind turbine blades is responsible for more than 50% of the total power [32]. Consequently, one of the main functions of the tower and the inner blade part is simply to hold the tip in optimal position. This significantly increases the weight of the entire system. In AWE system, the blade and the tower are substituted by the wing and by the tether respectively which allows the kite to reach even higher altitudes. Moreover, since the AWE system does not suffer from large overturning moment like tall wind turbine does, it does not require a solid foundation [34]. In conclusion, the Airborne Wind Energy system is lighter and requires less material than conventional wind turbines, which also reduces the global cost of the system.

In addition to material and price, AWE systems benefit from an easy mobility [34]. Indeed, Kitepower's idea is to fit the entire AWE system into a freight container, which can be easily transported by standard truck as presented on Figure 10.2. Furthermore, unlike large wind turbine, AWE system does not require a huge crane for installation, maintenance and refurbishment as shown on Figure 10.3. Thus, AWE system could be installed in places where conventional wind turbine could not. Another important aspect of AWE system is the fact that the maintenance will be easier, cheaper and safer since it will occur on ground level [34]. Eventually, replacing the tower by a thin tether will obviously lower the visual impact of the entire system.



Figure 10.2 Kitepower system fitted into a freight container.
Modified from author's picture.



Figure 10.3 Siemens SWT-6.0-154, 120 m hub height,
75 m long blade, from [78].

10.3 Lumped Tether Mass Derivation

Equation (2.31) given in spherical coordinate (r, θ, φ) is converted into Cartesian coordinates (x, y, z) according to the following Equations (10.1) to Equation (10.5), where $\varphi = 0$ for the 2-dimension assumption.

$$\mathbf{F}_{g,t}^{sphe} = \frac{1}{4} \rho_t \pi d_t^2 l_t g \begin{pmatrix} -\cos \theta \\ \frac{1}{2} \sin \theta \\ 0 \end{pmatrix} \quad (10.1)$$

$$\mathbf{F}_{g,t}^{Cart} = m_t g \begin{pmatrix} \sin \theta \cos \varphi & \cos \theta \cos \varphi & -\sin \varphi \\ \sin \theta \sin \varphi & \cos \theta \sin \varphi & \cos \varphi \\ \cos \theta & -\sin \theta & 0 \end{pmatrix} \begin{pmatrix} -\cos \theta \\ \frac{1}{2} \sin \theta \\ 0 \end{pmatrix} \quad (10.2)$$

$$\mathbf{F}_{g,t}^{Cart} = m_t g \begin{pmatrix} \frac{1}{2} \sin \theta \cos \theta \cos \varphi - \sin \theta \cos \theta \cos \varphi \\ \frac{1}{2} \sin \theta \cos \theta \sin \varphi - \sin \theta \cos \theta \sin \varphi \\ -\frac{1}{2} \sin^2 \theta - \cos^2 \theta \end{pmatrix} \quad (10.3)$$

$$\mathbf{F}_{g,t}^{Cart} = m_t g \begin{pmatrix} -\frac{1}{2} \sin \theta \cos \theta \\ 0 \\ -\frac{1}{2} \sin^2 \theta - \cos^2 \theta \end{pmatrix} \quad (10.4)$$

$$\mathbf{F}_{g,t}^{Cart} = m_t g \begin{pmatrix} -\frac{1}{2} \cos \beta \sin \beta \\ 0 \\ -\sin^2 \beta - \frac{1}{2} \cos^2 \beta \end{pmatrix} \quad (10.5)$$

10.4 Sag Differential Equation Derivation

The following derivation leads to the differential equation system regarding the tether sag.

$$\text{ox :} \quad -F_t \cos(\beta) + (F_t + dF_t) \cos(\beta + d\beta) + \frac{1}{2} \rho_{air} C_{D,t} d_t V_a^2 dr = 0 \quad (10.6)$$

$$\text{oz :} \quad -F_t \sin(\beta) + (F_t + dF_t) \sin(\beta + d\beta) - \rho'_t g dr - \frac{1}{2} \rho_{air} C_{L,t} d_t V_a^2 = 0 \quad (10.7)$$

$$\text{ox :} \quad -F_t \cos(\beta) + (F_t + dF_t) (\cos(\beta) - \sin(\beta) d\beta) + \frac{1}{2} \rho_{air} C_{D,t} d_t V_a^2 dr = 0 \quad (10.8)$$

$$\text{oz :} \quad -F_t \sin(\beta) + (F_t + dF_t) (\sin(\beta) + \cos(\beta) d\beta) - \rho'_t g dr - \frac{1}{2} \rho_{air} C_{L,t} d_t V_a^2 = 0 \quad (10.9)$$

$$\text{ox :} \quad dF_t \cos(\beta) - F_t \sin(\beta) d\beta + \frac{1}{2} \rho_{air} C_{D,t} d_t V_a^2 dr = 0 \quad (10.10)$$

$$\text{oz :} \quad dF_t \sin(\beta) + F_t \cos(\beta) d\beta - \left(\rho'_t g + \frac{1}{2} \rho_{air} C_{L,t} d_t V_a^2 \right) dr = 0 \quad (10.11)$$

$$\text{ox :} \quad F_t d\beta = dF_t \frac{\cos(\beta)}{\sin(\beta)} + \frac{1}{2} \rho_{air} C_{D,t} d_t V_a^2 \frac{dr}{\sin(\beta)} \quad (10.12)$$

$$\begin{aligned} \text{oz :} \quad & dF_t \sin(\beta) + dF_t \frac{\cos^2(\beta)}{\sin(\beta)} + \frac{1}{2} \rho_{air} C_{D,t} d_t V_a^2 \frac{\cos(\beta)}{\sin(\beta)} dr \\ & - \left(\rho'_t g + \frac{1}{2} \rho_{air} C_{L,t} d_t V_a^2 \right) dr = 0 \end{aligned} \quad (10.13)$$

$$\text{oz :} \quad dF_t + \frac{1}{2} \rho_{air} C_{D,t} d_t V_a^2 \cos(\beta) \frac{dz}{\sin(\beta)} - \left(\rho'_t g + \frac{1}{2} \rho_{air} C_{L,t} d_t V_a^2 \right) dz = 0 \quad (10.14)$$

$$\text{oz :} \quad \frac{dF_t}{dz} = \rho'_t g + \frac{1}{2} \rho_{air} d_t V_a^2 \left(C_{L,t} - C_{D,t} \frac{\cos(\beta)}{\sin(\beta)} \right) \quad (10.15)$$

$$\begin{aligned} \text{ox :} \quad & \cos(\beta) \rho'_t g + \frac{1}{2} \rho_{air} d_t V_a^2 \left(C_{L,t} - C_{D,t} \frac{\cos(\beta)}{\sin(\beta)} \right) \cos(\beta) - F_t \sin(\beta) \frac{d\beta}{dz} \\ & + \frac{1}{2} \rho_{air} C_{D,t} d_t V_a^2 \frac{1}{\sin(\beta)} = 0 \end{aligned} \quad (10.16)$$

$$\text{ox :} \quad F_t \frac{d\beta}{dz} = \frac{\cos(\beta)}{\sin(\beta)} \rho'_t g + \frac{1}{2} \rho_{air} d_t V_a^2 \left(C_{L,t} \frac{\cos(\beta)}{\sin(\beta)} - C_{D,t} \frac{\cos^2(\beta)}{\sin^2(\beta)} + C_{D,t} \frac{1}{\sin^2(\beta)} \right) \quad (10.17)$$

$$\text{ox :} \quad F_t \frac{d\beta}{dz} = \frac{\cos(\beta)}{\sin(\beta)} \rho'_t g + \frac{1}{2} \rho_{air} d_t V_a^2 \left(C_{L,t} \frac{\cos(\beta)}{\sin(\beta)} + C_{D,t} \right) \quad (10.18)$$

10.5 Error Propagation Derivation

The absolute error for the glide ratio G in Equation (10.19) is derived from Equation (5.1).

$$\Delta G = \left| \frac{\partial \tan \vartheta_w}{\partial \vartheta_w} \right| \Delta \vartheta_w = \frac{\Delta \vartheta_w}{\cos^2 \vartheta_w} \quad (10.19)$$

The absolute error for the aerodynamic coefficient C_R is derived in Equation (10.20) and Equation (10.21) from Equation (2.24).

$$\Delta C_R = \left| \frac{\partial \frac{2 F_t}{\rho_{air} A_{ref} V_a^2}}{\partial F_t} \right| \Delta F_t + \left| \frac{\partial \frac{2 F_t}{\rho_{air} A_{ref} V_a^2}}{\partial V_a} \right| \Delta V_a \quad (10.20)$$

$$\Delta C_R = \frac{2 \Delta F_t}{\rho_{air} A_{ref} V_a^2} + \frac{4 F_t \Delta V_a}{\rho_{air} A_{ref} V_a^3} \quad (10.21)$$

The absolute error for lift coefficient C_L is derived from Equation (5.5) in Equation (10.22) to Equation (10.25).

$$\Delta C_L = \left| \frac{\partial \frac{C_R}{\sqrt{1+G^{-2}}}}{\partial C_R} \right| \Delta C_R + \left| \frac{\partial \frac{C_R}{\sqrt{1+G^{-2}}}}{\partial G} \right| \Delta G \quad (10.22)$$

$$\Delta C_L = \frac{\Delta C_R}{\sqrt{1+G^{-2}}} + C_R \Delta G \left(\frac{1}{2} (1+G^{-2})^{-\frac{3}{2}} \right) \left| \frac{\partial (1+G^{-2})^{-\frac{1}{2}}}{\partial G} \right| \quad (10.23)$$

$$\Delta C_L = \frac{\Delta C_R}{\sqrt{1+G^{-2}}} + C_R \Delta G \left(\frac{1}{2} (1+G^{-2})^{-\frac{3}{2}} \right) (2 G^{-3}) \quad (10.24)$$

$$\Delta C_L = \frac{\Delta C_R}{\sqrt{1+G^{-2}}} + \frac{C_R \Delta G}{(1+G^{-2})^{\frac{3}{2}} G^3} \quad (10.25)$$

The absolute error for drag coefficient C_D given in Equation (5.6) is derived in Equation (10.26) and Equation (10.27).

$$\Delta C_D = \left| \frac{\partial \frac{C_L}{G}}{\partial C_L} \right| \Delta C_L + \left| \frac{\partial \frac{C_L}{G}}{\partial G} \right| \Delta G \quad (10.26)$$

$$\Delta C_D = \frac{\Delta C_L}{G} + \frac{C_L \Delta G}{G^2} \quad (10.27)$$

10.6 Corrected Lift and Drag Coefficients

- Kite Mass Effect

$$C_L = \frac{F_t \sin \beta + m_k g}{q} \quad (10.28)$$

$$C_D = \frac{F_t \cos \beta}{q} \quad (10.29)$$

- Tether Mass Effect

$$C_L = \frac{F_t \sin \beta + \frac{1}{4} \rho_t \pi d_t^2 l_t \left(\frac{1}{2} \cos^2 \beta + \sin^2 \beta \right)}{q} \quad (10.30)$$

$$C_D = \frac{F_t \cos \beta + \frac{1}{4} \rho_t \pi d_t^2 l_t \left(\frac{1}{2} \cos \beta \sin \beta \right)}{q} \quad (10.31)$$

- Global Mass Effect

$$C_L = \frac{F_t \sin \beta + m_k g + \frac{1}{4} \rho_t \pi d_t^2 l_t \left(\frac{1}{2} \cos^2 \beta + \sin^2 \beta \right)}{q} \quad (10.32)$$

$$C_D = \frac{F_t \cos \beta + \frac{1}{4} \rho_t \pi d_t^2 l_t \left(\frac{1}{2} \cos \beta \sin \beta \right)}{q} \quad (10.33)$$

- Tether Lift Effect

$$C_L = \frac{F_t \sin \beta + \frac{1}{4} C_{L,t} \rho_{air} d_t l_t V_a^2}{q} \quad (10.34)$$

$$C_D = \frac{F_t \cos \beta}{q} \quad (10.35)$$

- Tether Drag Effect

$$C_L = \frac{F_t \sin \beta}{q} \quad (10.36)$$

$$C_D = \frac{F_t \cos \beta - \frac{1}{4} C_{D,t} \rho_{air} d_t l_t V_a^2}{q} \quad (10.37)$$

- Global Tether Aerodynamic Effect

$$C_L = \frac{F_t \sin \beta + \frac{1}{4} C_{L,t} \rho_{air} d_t l_t V_a^2}{q} \quad (10.38)$$

$$C_D = \frac{F_t \cos \beta - \frac{1}{4} C_{D,t} \rho_{air} d_t l_t V_a^2}{q} \quad (10.39)$$

- Global Effect

$$C_L = \frac{F_t \sin \beta + m_k g + \frac{1}{4} \rho_t \pi d_t^2 l_t \left(\frac{1}{2} \cos^2 \beta + \sin^2 \beta \right) + \frac{1}{4} C_{L,t} \rho_{air} d_t l_t V_a^2}{q} \quad (10.40)$$

$$C_D = \frac{F_t \cos \beta + \frac{1}{4} \rho_t \pi d_t^2 l_t \left(\frac{1}{2} \cos \beta \sin \beta \right) - \frac{1}{4} C_{D,t} \rho_{air} d_t l_t V_a^2}{q} \quad (10.41)$$

10.7 Kite and Tether Mass Effects

The effect of kite mass and tether mass on the aerodynamic properties are presented individually in the following Figure 10.4. The uncorrected data, namely massless case, is shown in orange colour. The dots and error bars illustrate the median and its corresponding \pm MAD respectively whereas the smooth orange line is the corresponding 3rd order polynomial fit. The effect of the kite mass is shown in blue while yellow colour represents the correction due to the tether mass. The global mass effect is illustrated in green.

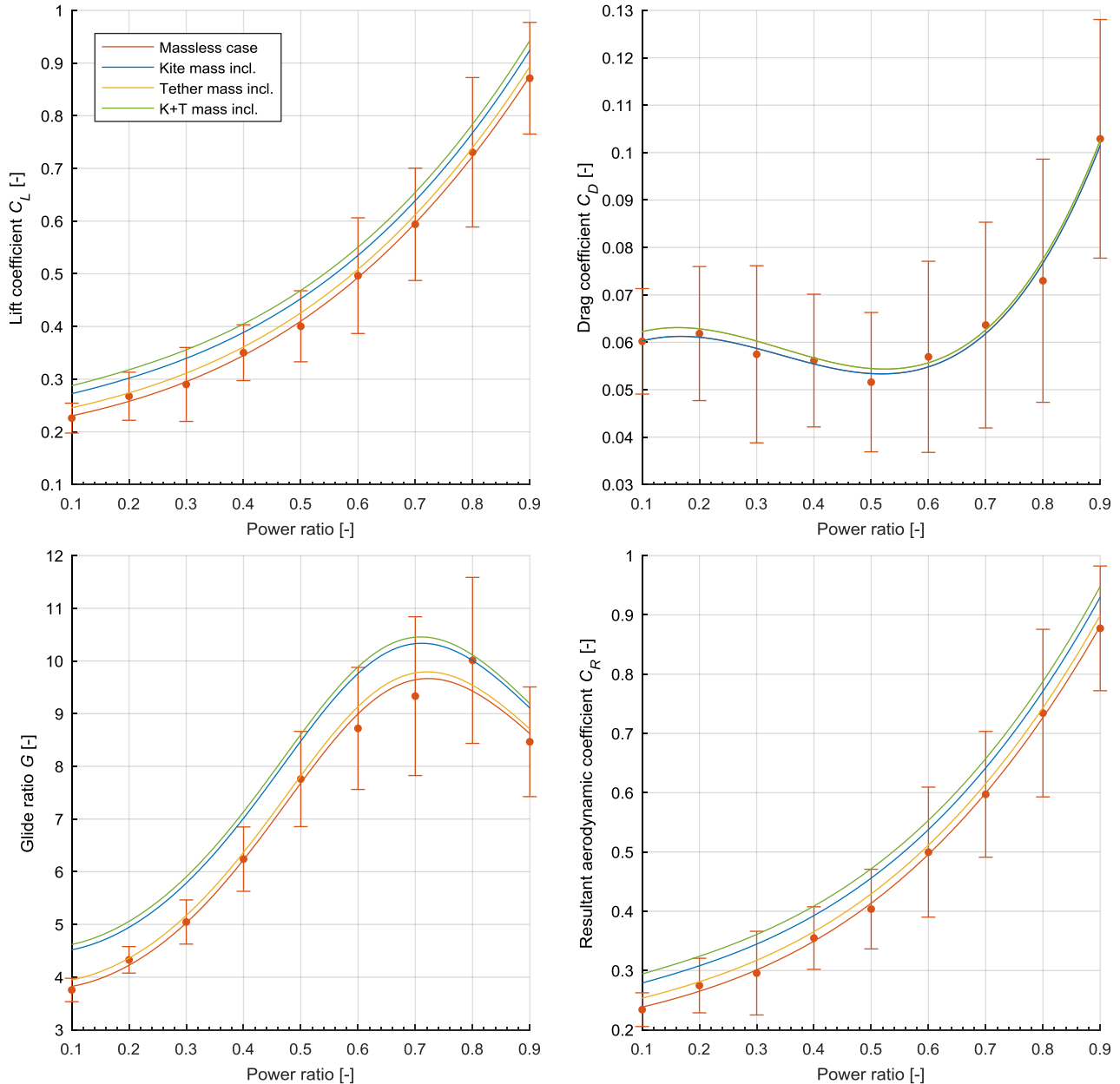


Figure 10.4 Mass effect on aerodynamic performances for the Hydra V5 at 22 kt. Orange: massless case with median \pm MAD and polyfit. Blue: kite mass included. Yellow: tether mass included. Green: both kite and tether mass included.

10.8 Tether Drag and Lift Effects

The effect of the aerodynamic forces acting on the tether on the kite properties are detailed in the following Figure 10.5. The uncorrected data, namely the case for which the tether is neglected, is shown in orange colour. The dots and error bars illustrate the median and its corresponding \pm MAD respectively whereas the smooth orange line is the corresponding 3rd order polynomial fit. The effect of the tether drag is shown in blue while yellow colour represents the correction due to the tether lift. The global tether aerodynamic effect is illustrated with green colour.

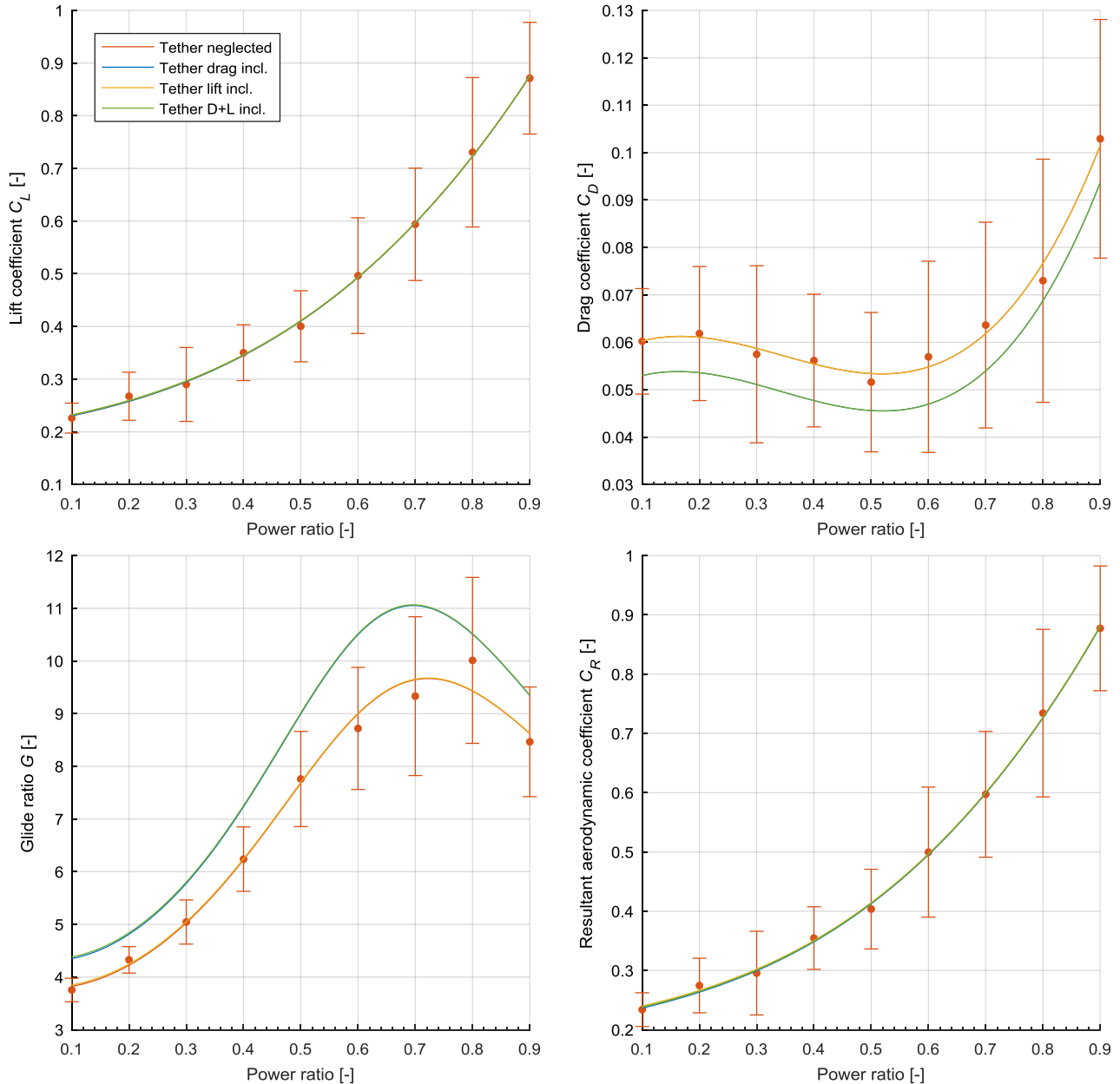


Figure 10.5 Drag and lift effect of the tether on aerodynamic performances for the Hydra V5 at 22 kt. Orange: tether neglected, median \pm MAD and polyfit. Blue: tether drag included. Yellow: tether lift included. Green: both drag and lift included.

10.9 Hypothetical Pitch Angle – Power Ratio Relationship

In Figure 10.6, the aerodynamic properties of the kite are presented with respect to the pitch angle obtained by considering the power ratio angle ε to be double the one actually established in Figure 6.21. Although the values of the pitch angle are unrealistic, the trends of C_L and C_D becomes more realistic.

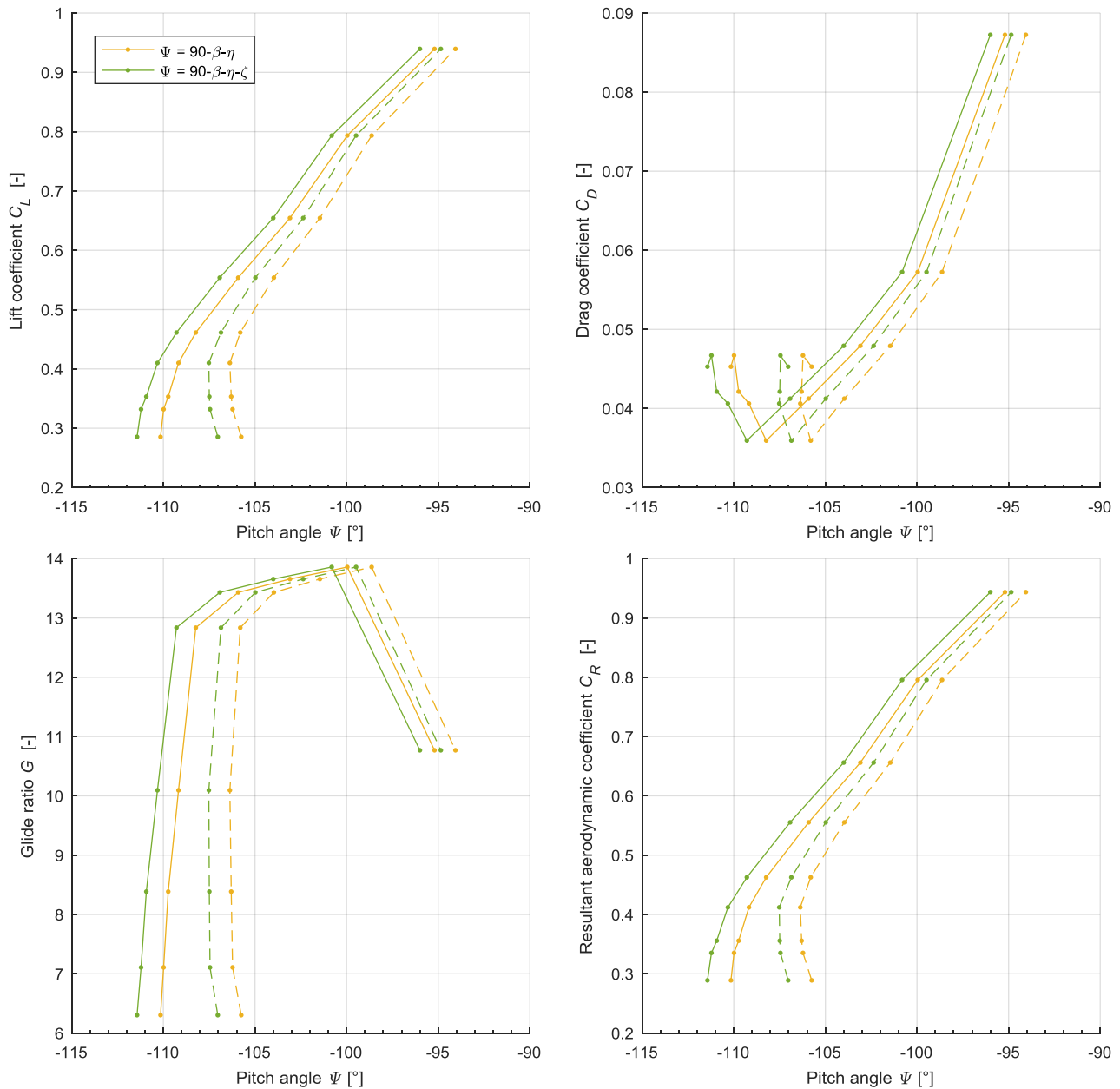


Figure 10.6 Aerodynamic properties expressed with respect to the hypothetical pitch angle obtained by doubling the value of the power ratio angle. Dashed lines considered the elevation angle at the ground whereas solid lines the elevation angle at the kite.

10.10 Instantaneous Aerodynamic Properties vs Pitch Angle

The instantaneous aerodynamic properties derived from the tether sag model are presented in Figure 10.7 for each power ratio. The pitch angle is obtained from Equation (5.28) by considering the elevation angle at the kite β_k and by including the angle at the handle bar junction ζ . The black dots indicate the median of the instantaneous measurements for each power ratio. They correspond to the solid green line in Figure 6.23.

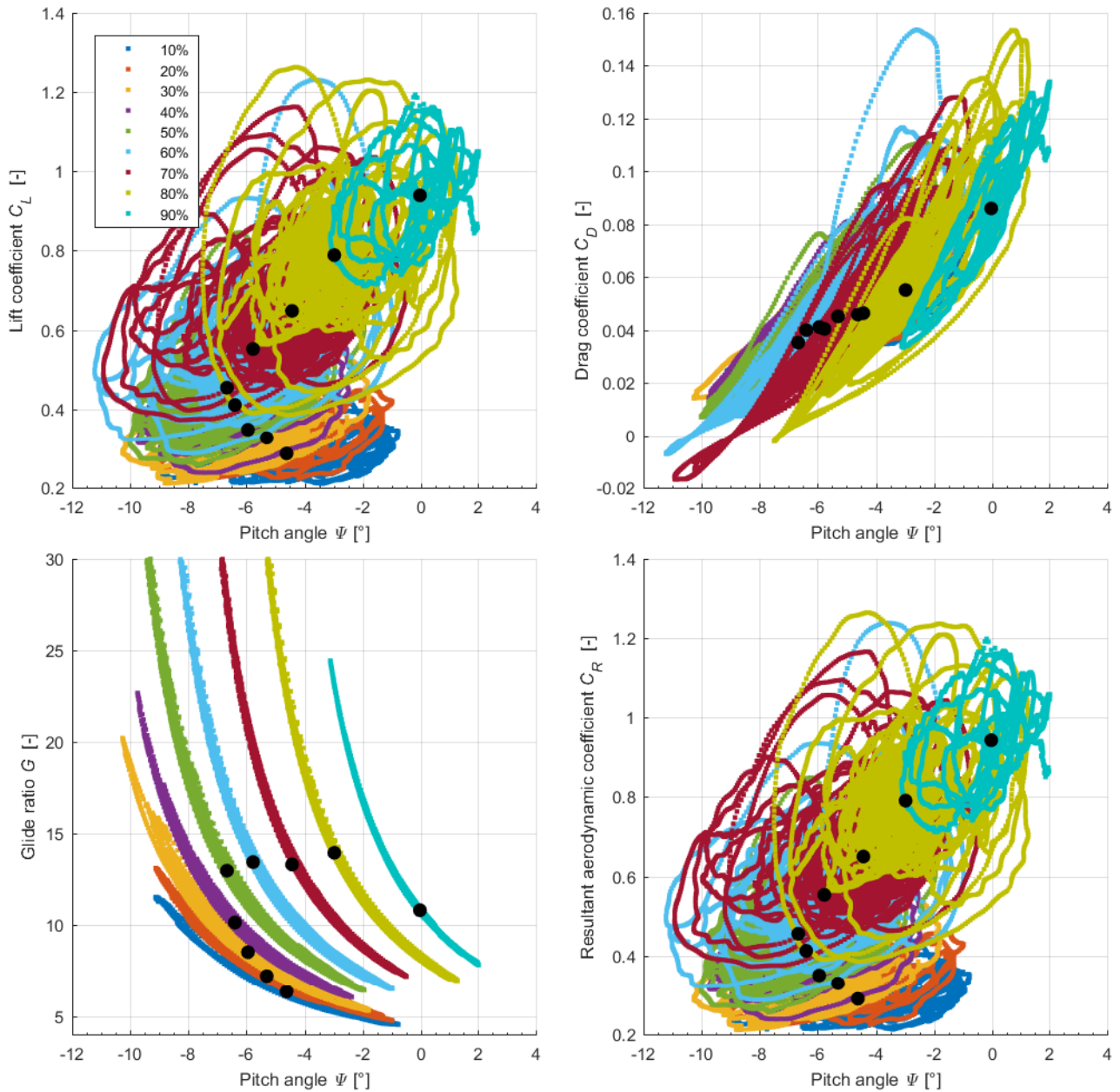


Figure 10.7 Instantaneous aerodynamic properties for the Hydra V5 at 22 kt obtained from the tether sag model (Chapter 6.6) and expressed with respect to the pitch angle.